Spring 2017

Numerical simulation of viscoelastic buckle folds: Implications for stress, fractures, porosity and fluid flow

Xiaolong Liu

Follow this and additional works at: https://scholarsmine.mst.edu/doctoral_dissertations

Part of the Petroleum Engineering Commons

Department: Geosciences and Geological and Petroleum Engineering

Recommended Citation

NUMERICAL SIMULATION OF VISCOELASTIC BUCKLE FOLDS:

IMPLICATIONS FOR STRESS, FRACTURES, POROSITY AND FLUID FLOW

by

XIAOLONG LIU

A DISSERTATION

Presented to the Faculty of the Graduate School of the

MISSOURI UNIVERSITY OF SCIENCE AND TECHNOLOGY

In Partial Fulfillment of the Requirements for the Degree

DOCTOR OF PHILOSOPHY
in
PETROLEUM ENGINEERING

2017

Approved by

Andreas Eckert, Advisor
John Hogan
Wan Yang
Peyman Heidari
Dean Thornton

PUBLICATION DISSERTATION OPTION

This dissertation consists of the following three articles, formatted in the style used by the Missouri University of Science and Technology:

Paper I: Pages 4-50 were published in TECTONOPHYSICS.

Paper II: Pages 51-93 are intended for submission to published in the Journal of JOURNAL OF STRUCTURAL GEOLOGY.

Paper III: Pages 94-138 have been submitted to the Journal of AMERICAN ASSOCIATION OF PETROLEUM GEOLOGISTS BULLETIN.

ABSTRACT

Over the past several decades, buckle folds have been exclusively studied by numerous methods. However, lots of assumptions and simplifications are made, which may not result in realistic in-situ stress conditions leading to rock failure. This study represents the first numerical simulation of folding under the consideration of gravity and pore pressure to simulate the structural development of buckle folds.

The first topic covered in this dissertation is the fracture associated to the single layer fold. It is concluded that burial depth, viscosity, and permeability are critical for the initiation of major fracture sets at the hinge zone with varying degrees. Moreover, this study provides a detail research on the stress and strain distribution in the multilayer folds and it is concluded that the stress/strain state within the folding layer(s) are determined by the buckling process, fold geometry and material parameters. The second topic covered in this dissertation is the numerical simulation of multilayer folds. This study demonstrates that the shapes of the multilayer folds are influenced by the various parameters. In addition, the numerical simulations provide a general understanding of the stress/strain distribution in the multilayer system. The third topic covered in this dissertation is the numerical simulation of parasitic folds. This study demonstrates that the shapes of the parasitic folds depend on the buckling of both the large- and small-scale folds and are influenced by the various parameters. The numerical modeling results show a large variability in porosity changes due to the complex distribution of the volumetric strain. In addition, the numerical simulations provide a general understanding of the influence of the various model parameters on the resulting porosity distribution.

ACKNOWLEDGMENTS

First, I want to express my sincere gratitude to my advisor, Dr. Andreas Eckert, for guiding and teaching me over the past four years. I gained a great deal from his immense knowledge, sheer tenacity, and great perception on research. I really appreciate his continuous support and patience.

Besides my advisor, I would like to thank the members of my dissertation committee, Dr. John Hogan, Dr. Wan Yang, Dr. Peyman Heidari, and Dr. Dean Thornton, for their constructive suggestions throughout this process. I appreciate your discussions, reviews and feedback on my dissertation. The financial support from Chevron ETC is greatly appreciated. I want to express my special thanks to Dr. Peter Connolly for his valuable and constructive reviews, which greatly improved the quality of my research.

I am grateful to the staff of Geosciences and Geological and Petroleum Engineering department, Patti Adams, Paula Cochran, Sharon Lauck, Patti Robertson, and Amy McMillen, Katherine Wagner in Graduate office, for all the assistances over the past several years. I want to thank the help from my friends and colleagues of the numerical geomechanics group, including Nevan Himmelberg, Weicheng Zhang, Eli Steinbeck, Davi Damasceno, Avery Welker, Jianbo Liu, Yuxing Wu.

Last but not least, I want to thank my loving wife, Daisy, my daughter, Olivia, and my parents. I cannot accomplish my doctoral dissertation without their understanding, support, encouragement, and constant love.

TABLE OF CONTENTS

LIST OF ILLUSTRATIONS

PAPER Ⅱ

LIST OF TABLES

NOMENCLATURE

Symbol	Description

PAPER I

σ_{xx}	Stress tensor at x direction
σ_{yy}	Stress tensor at y direction
σ_{zz}	Stress tensor at z direction
σ_{xy}	Shear stress at x-y plane
σ_{xz}	Shear stress at x-z plane
σ_{yz}	Shear stress at y-z plane
P_p	Pore pressure
v_x	Velocity along x direction
v_y	Velocity along y direction
v_z	Velocity along z direction
ρ_m	Material density
K	Bulk modulus
G	Shear modulus
E	Young's modulus
μ	Viscosity
α	Biot coefficient
k_x	Permeability along x direction
k_y	Permeability along y direction
k_z	Permeability along z direction
ϕ	Porosity
T_0	Tensile strength

PAPER II

σ_{xx}	Stress tensor at x direction
σ_{yy}	Stress tensor at y direction
σ_{xy}	Shear stress at x-y plane
P_p	Pore pressure

v_x	Velocity along x direction
v_y	Velocity along y direction
ρ_m	Material density
K	Bulk modulus
G	Shear modulus
E	Young's modulus
μ	Viscosity
α	Biot coefficient
k_x	Permeability along x direction
k_y	Permeability along y direction
ϕ	Porosity

PAPER III

σ_{xx}	Stress tensor at x direction
σ_{yy}	Stress tensor at y direction
σ_{xy}	Shear stress at x-y plane
P_p	Pore pressure
v_x	Velocity along x direction
v_y	Velocity along y direction
ρ_m	Material density
K	Bulk modulus
G	Shear modulus
E	Young's modulus
μ	Viscosity
α	Biot coefficient
k_x	Permeability along x direction
k_y	Permeability along y direction
ϕ	Porosity
H	Thickness of competent layer
S	Thickness of less competent layer
ε_v	Volumetric strain

N   Layer numbers

A   Amplitude

A′   Normalized amplitude

SECTION

1. INTRODUCTION

Folds are spectacular structures in deformed rocks, affecting single or multiple layers on all scales. They have played an important part, historically, in understanding episodes of deformation in orogenic belts. In addition, buckle folds of sedimentary strata represent prime examples of structural traps for hydrocarbon accumulation sites. These structures commonly feature a variety of different fracture sets, which may affect the structural permeability of potential reservoirs. Some fracture sets including outer arc tensile fractures and inner arc shear fractures at the fold hinge zones are well understood by the extensional and compressional strain/stress pattern. However, other commonly observed fracture sets, including tensile fractures parallel to the fold axis, tensile fractures cutting through the limb, extensional faults at the fold hinge, and other shear fractures of various orientations in the fold limb, fail to be intuitively explained by the strain/stress regimes during the buckling process. In addition to the occurrence of fractures, pore pressure and fluid flow during the deformational history of geologic structures are directly influenced by tectonic deformation events.

In addition, the viscoelastic behavior of deformed geological materials has not been widely considered for multilayer folds. It is known that magnitudes and orientations of principal stresses/strains vary significantly for different layers with respect to their relative location in the multilayer stack. The detailed influence of a larger number of layers and varying layer thickness ratios, which significantly affect the shape of multilayer folds and associated stress/strain distribution, remains unclear.

Moreover, in porous, granular rocks, compaction related porosity-loss is observed under loading as a result of the existence of the deformable grains in the sediment. Reduced porosity and pore connectivity would significantly reduce the permeability of deformed rocks by one to four orders of magnitude relative to the host rock matrix (Pittman, 1981). If tectonic compaction occurs in an active aquifer or reservoir, the reduced porosity connectivity would cause substantial fluid-flow effects at scales relevant to production and management. The change of porosity and permeability due to compaction and lateral loading depends strongly on the tectonic evolution, the original

porosity, the physical properties of the surrounding matrix, and the micro-tectonics of the rock fabric such as the development of foliations and/or cleavage. For complex deformation such as multi scale multilayer folding, the distribution of porosity which is related to the volumetric stain is strongly depend on the folding deformation. However, the strain evolution and distribution during the folding of one scale/multi scale multilayer remain unclear.

The dissertation is mainly composed of three parts. The first part provides results of the buckle folds of sedimentary strata commonly feature a variety of different fracture sets. Some fracture sets including outer arc tensile fractures and inner arc shear fractures at the fold hinge zones are well understood by the extensional and compressional strain/stress pattern. However, other commonly observed fracture sets, including tensile fractures parallel to the fold axis, tensile fractures cutting through the limb, extensional faults at the fold hinge, and other shear fractures of various orientations in the fold limb, fail to be intuitively explained by the strain/stress regimes during the buckling process. To obtain a better understanding of the conditions for the initiation of the various fractures sets associated with single-layer cylindrical buckle folds, a 3D finite element modeling approach using a Maxwell visco-elastic rheology is utilized. The influences of three model parameters with significant influence on fracture initiation are considered: burial depth, viscosity, and permeability. It is concluded that these parameters are critical for the initiation of major fracture sets at the hinge zone with varying degrees. The numerical simulation results further show that the buckling process fails to explain most of the fracture sets occurring in the limb unless the process of erosional unloading as a post-fold phenomenon is considered. For fracture sets that only develop under unrealistic boundary conditions, the results demonstrate that their development is realistic for a perclinal fold geometry. In summary, a more thorough understanding of fractures sets associated with buckle folds is obtained based on the simulation of in-situ stress conditions during the structural development of buckle folds.

The second part conducted the numerical simulation of multilayers and associated stress/strain distribution. In this study, a 2-D plane strain finite element modeling approach is used to simulate multilayer, viscoelastic buckle folds under in-situ stress and pore pressure conditions. A variety of material and model parameters (including the

elastic modulus contrast, viscosity contrast, initial overburden, number of layers, and layer thickness ratio) are considered and their influence on the shape of folds and on the resulting stress/strain distribution is analyzed. This study demonstrates that the shapes of the multilayer folds are influenced by the various parameters. The numerical modeling results show that tensile stress occurs at the hinge and the region between the hinge and the limb for certain layers and are influenced by the material and model parameters by various degree. In addition, the numerical simulations provide a general understanding of the strain distribution in the multilayer system where the less competent layers exhibit a large variability in the maximum principal strain distribution. This study show that the thickness ratio of the competent and less competent layers has a major impact on the fold shapes and resulted stress/strain distribution for viscoelastic multilayer folding.

The third part conducted numerical study of parasitic folds and associated porosity distribution. Parasitic folds represent a common structure of multi-scale multilayer folds and the resulting asymmetric S- or Z-shapes and symmetric M-shapes represent a complex strain distribution. How the strain distribution affects the resulting porosity remains unclear. In this study, a 2-D plane strain finite element modeling approach is used to simulate multi-scale, multilayer, viscoelastic buckle folds under in-situ stress and pore pressure conditions. A variety of material and model parameters (including the elastic modulus contrast, number of layers, viscosity contrast, strain rate and layer thickness ratio) are considered and their influence on the shape of parasitic folds and on the resulting porosity distribution is analyzed. This study demonstrates that the shapes of the parasitic folds depend on the buckling of both the large- and small-scale folds and are influenced by the various parameters. The numerical modeling results show a large variability in porosity changes due to the complex distribution of the volumetric strain during the mutli-scale, multi-layer buckling process. Three regions, including the hinge and limb of the less competent layer in the M-shaped folds and the limb of the less competent layer in the Z-shaped folds, feature significant porosity changes. In addition, the numerical simulations provide a general understanding of the influence of the various model parameters on the resulting porosity distribution. Through the applied volumetric stain-porosity-permeability coupling, influences on the resulting fluid flow regimes in multi-scale, multilayer buckling systems are documented.

PAPER

I. STRESS EVOLUTION DURING 3D SINGLE-LAYER VISCOELASTIC BUCKLE FOLDING: IMPLICATIONS FOR THE INITIATION OF FRACTURES

Xiaolong Liu*

Department of Geosciences and Geological and Petroleum Engineering, Missouri University of Science and Technology, Rolla, Missouri. 65401-0140 USA.

Email address: xlwz9@mst.edu.Tel:01-573-3414151

Andreas Eckert

Department of Geosciences and Geological and Petroleum Engineering, Missouri University of Science and Technology, Rolla, Missouri 65401-0141. USA.

Peter Connolly

Chevron ETC, 1500 Louisiana St, Houston, TX 77002. USA.

Highlights**:**

- 3D Single-layer buckle folds are simulated under realistic stress conditions.
- Burial depth, viscosity, and permeability are critical for the initiation of major fracture sets at the hinge zone.
- Fold associated fractures in the limb are the result of a combination of buckling and erosional unloading.
- A periclinal fold geometry provides a general explaination for various fracture sets at significant depth.

ABSTRACT

Buckle folds of sedimentary strata commonly feature a variety of different fracture sets. Some fracture sets including outer arc tensile fractures and inner arc shear fractures at the fold hinge zones are well understood by the extensional and compressional strain/stress pattern. However, other commonly observed fracture sets, including tensile fractures parallel to the fold axis, tensile fractures cutting through the limb, extensional faults at the fold hinge, and other shear fractures of various orientations in the fold limb, fail to be intuitively explained by the strain/stress regimes during the buckling process. To obtain a better understanding of the conditions for the initiation of the various fractures sets associated with single-layer cylindrical buckle folds, a 3D finite element modeling approach using a Maxwell visco-elastic rheology is utilized. The influences of three model parameters with significant influence on fracture initiation are considered: burial depth, viscosity, and permeability. It is concluded that these parameters are critical for the initiation of major fracture sets at the hinge zone with varying degrees. The numerical simulation results further show that the buckling process fails to explain most of the fracture sets occurring in the limb unless the process of erosional unloading as a post-fold phenomenon is considered. For fracture sets that only develop under unrealistic boundary conditions, the results demonstrate that their development is realistic for a perclinal fold geometry. In summary, a more thorough understanding of fractures sets associated with buckle folds is obtained based on the simulation of in-situ stress conditions during the structural development of buckle folds.

Key words: 3D single-layer visco-elastic buckle folding; Fracture initiation; Stress evolution; Erosional unloading; Pericline.

1. INTRODUCTION

Observations from various types of folds in nature show an abundance of folding related fractures, both shear and tensile. The location, type, extent, orientation, and likelihood of occurrence of these fractures are of importance in geomechanical analyses of folded strata both for fluid flow pathway and reservoir stability prediction. Numerous studies have been conducted to investigate the distribution and patterns of fractures associated with folds based on field observations (e.g. McQuillan, 1973, McQuillan, 1974; Groshong, 1975; Catherine et al., 1997; Hennings et al., 2000; Guiton et al., 2003; Bergbauer and Pollard, 2004; Florez-Niño et al., 2005; Bellahsen et al., 2006; Wennberg et al., 2006, Stephenson et al., 2007; Ismat, 2008; Ghosh and Mitra, 2009; Reber et al., 2010; Barbier et al., 2012; Iñigo et al., 2012; Vitale et al., 2012; Awdal et al., 2013; Watkins et al., 2015). The relation between the occurrence and development of the fracture systems and folding are dependent on a variety of parameters, such as layer thickness (McQuillan, 1973; Tavani et al. 2015), lithology (e.g. Catherine et al., 1997; Ericsson et al., 1998; Wennberg et al., 2006; Ghosh and Mitra, 2009; Watkins et al., 2015), curvature (e.g. Lisle, 1992; 1994; Hennings et al., 2000), the state of stress (Price, 1966; Ramsay, 1967; Stearns, 1968; Groshong, 1975; Price and Cosgrove, 1990; Lemiszki et al., 1994; Guiton et al.,2003; Reber et al., 2010; Eckert et al., 2014), interlayer slip (Chapple and Spang, 1974; Cooke and Underwood, 2001; Smart et al., 2009), their position in the fold system (e.g. Cloos, 1948; Price and Cosgrove, 1990; Bellahsen et al., 2006; Ismat, 2008; Jäger et al.,2008; Awdal et al., 2013; Eckert et al., 2014) and deformation history (Bergbauer and Pollard, 2004; Florez-Niño et al., 2005; Stephenson et al., 2007; Smart et al., 2010; Smart et al., 2012; Vitale et al., 2012). The often cited conceptual model by Price (1966) and Stearns (1968) suggests that there are 5 common fracture sets forming systematically with respect to the fold axis.

However, it is clear that the existence of fractures and the conditions for their initiation within fold structures can be attributed to various different, specific folding mechanisms (such as forced folding or buckle folding) and the stress evolution during either pre-folding, folding or post-folding (Price and Cosgrove, 1990; Eckert et al., 2014). Due to the several different types of forced folds, a generalized fold-fracture model does

not exist and the fracture pattern strongly depends on the specific type of forced folding (Cooke et al., 1999; Cosgrove and Ameen, 2000; Couples and Lewis, 1999; Laubach et al., 1999; Smart et al., 2010; Smart et al., 2012).

For buckle folds, the relation of various fractures types and the fold geometry is discussed by Price and Cosgrove (1990) and a general comparison of fracture patterns associated with buckle folds and various types of forced folds has been established by Cosgrove and Ameen (2000). Fractures associated with buckle folding may result from the regional principal stresses, which are either parallel/subparallel or normal/subnormal to bedding during buckling of originally horizontal layers (Dieterich and Carter, 1969; Dieterich, 1969; Parrish et al. 1976). Figure 1 shows the orientations of the various types of tensile and shear fractures associated with buckle folds, their locations and the stress conditions for their occurrence (after Price and Cosgrove, 1990). As stated by Price and Cosgrove (1990), different sets of tensile fractures (Fractures 1-4 in Figure 1), and conjugate shear fractures (fracture Sets 5-10 in Figure 1) require different relations of the principal stresses, and thus these fractures develop at different times during the deformation history of the fold, including pre-folding and post-folding stages, as the stress state changes. It should be noted that these fractures represent various joint and fracture types including extensional faults (i.e. fracture Sets 6 and 9), compressive faults (i.e. fracture Set 5), conjugate shear fractures (i.e. fracture Sets 7, 8 10 and 11) and dilational joints (i.e. Fractures 1-4).

Amongst the most noticeable fractures associated with buckle folds are tensile fractures occurring at the outer hinges of the fold crest (Fracture 1), and shear fractures at the bottom of fold hinge zones (Set 5). The conditions for their occurrence are well understood and are related to the tensional and compressional strain/stress pattern developing in buckled elastic materials (Ramsay, 1967; Turcotte and Schubert, 2002) and also in the fold hinge zone of buckled rocks (e.g. Price and Cosgrove, 1990; Lemiszki et al., 1994; Reber et al., 2010; Frehner, 2011; Eckert et al., 2014). Shear fractures in the fold limb (Set 7) are frequently observed (e.g. Price and Cosgrove, 1990; Ismat, 2008) and attributed to the state of stress during the horizontal compression. Bedding parallel tensile failure (Fracture 4), i.e. bedding-parallel fibrous veins, also

termed as "Beef" (Cobbold, 2013) can be attributed to fluid overpressure in combination with horizontal compression during buckling (Eckert et al., 2014).

There are fracture sets that are not intuitively linked to the stress regime occurring during buckling. These include layer penetrating tensile fractures parallel to the fold axis in the limb with various dip angles (Fracture 2 in Figure 1; Engelder et al., 2009), layer penetrating tensile fractures perpendicular to the fold axis in the limb (Fracture 3 in Figure 1, Price and Cosgrove, 1990; Bergabuer and Pollard, 2004 Engelder, 2007; Ismat, 2008), extensional (i.e. normal) faults at the fold hinge (fracture Set 6 in Figure 1, Price and Cosgrove, 1990), conjugate shear fractures with the acute bisector sub-parallel to the fold trend (fracture Set 8 in Figure 1; Price and Cosgrove, 1990), oblique faults (in the limb) or extensional faults (at the hinge) with steep dip angles (fracture Set 9 in Figure 1; Price and Cosgrove, 1990; Ismat, 2008), conjugate faults with the acute bisector sub-perpendicular to the bedding surface in the limb (fracture Set 10 in Figure 1; Ismat, 2008) and conjugate faults with the acute bisector sub-parallel to the bedding and perpendicular to the fold axis in the limb (fracture Set 11 in Figure 1, Price and Cosgrove, 1990; Lemiszki et al., 1994). In particular, shear factures Set 10 and Set 11 may separate the fold hinge from the limbs.

Of all these fracture sets identified, the association of Sets 8 and 10 to buckle folding is questionable since the maximum principal stress, σ'_1, is mostly parallel to the shortening direction during buckling (Eckert et al., 2014). Furthermore, tensile fractures 2 remain difficult to explain since the necessary direction of the minimum principal stress, σ'_3, perpendicular to the fracture, is unlikely to be sub-parallel to the shortening direction at the fold limb during the buckling process. Hence this fracture is more likely to be influenced by either pre-folding deformation or post-folding deformation (Engelder, 2009).

In summary, the fractures shown in Figure 1 are all based on observations from field studies (e.g. Price and Cosgrove, 1990; Cosgrove and Ameen, 2000) and any given fracture pattern is the result of some stage during the complete stress history undergone by the rocks, including the deformation history during buckle folding. In this regard, a distinction has to be made relative to the time of fracture development, i.e. if the fractures developed before, during or after buckle folding, since it is very unlikely that all these
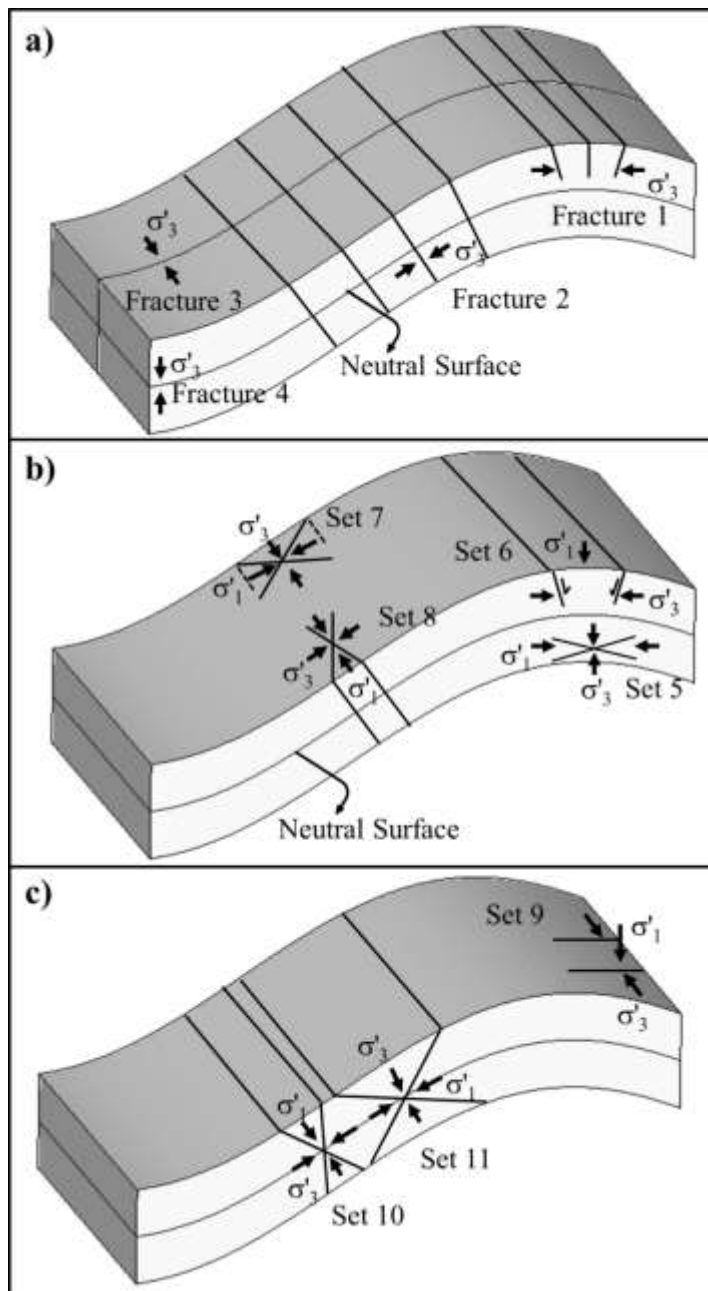
Figure 1. Fracture sets commonly identified within fold structures, and the inferred orientations of the minimum and maximum principal stresses (σ'_3 and σ'_1) necessary to form them. a) 4 different tensile fractures commonly associated with buckle folds. b) Conjugate shear fracture Sets 5 to 8 associated with buckle folds. c) Conjugate shear fracture Sets 9 with 11 associated to buckle folds.

fracture sets are formed coevally or during a single buckling episode (Price, 1966). This becomes of particular interest for Fractures 2 and 3, as different studies (Price and Cosgrove, 1990; Twiss and Moores, 1992; Engelder, et al., 2009) have concluded that

pre-existing bedding normal joint sets (i.e. Mode 1 fractures) play an important role in the distribution of fold related fractures. These observations support Casey and Butler (2004), who stated that the timing and evolution of fracture occurrence is not sufficiently understood. One of their main conclusions is that due to the complexity of the stress history in fold hinges the prediction of timing and location of fracturing requires methods and/or (numerical) models that include the stress evolution.

A common technique for fracture prediction for developed fold shapes is fold curvature analysis (e.g., Lisle, 1994; Fischer and Wilkerson, 2000; Bergbauer and Pollard, 2004) for which the neutral surface concept (Ramsay, 1967; Price and Cosgrove, 1990; Twiss and Moores, 2007; Frehner, 2011) is used to distinguish compressional failure and tensile failure. As Lisle (1992, 1994) pointed out, the fracture density within a fold may be directly related to the curvature of the fold. However, curvature analysis by itself is inherently limited since it does not account for the stress differences arising from material heterogeneities or changing pore pressure and moreover cannot consider the timing of fracture formation during the stress evolution (Smart et al., 2009).

A review of numerical modeling studies (e.g. Lemiszki et al., 1994; Casey and Butler, 2004; Reber et al., 2010; Frehner, 2011) investigating the occurrence of buckle fold related fractures shows that a great amount of knowledge has been gained on the evolution of buckle folds and their stress and strain history. However, lots of assumptions and simplifications are made, which may not result in realistic in-situ stress conditions leading to rock failure. Only a few numerical studies consider the influence of gravity (Schmalholz et al., 2002; Eckert et al., 2014) and the influence of pore pressure / overpressure is often reduced to the analysis of the mean stress (e.g. Stephansson, 1974; Mancktelow, 2008; Schmid et al., 2008). For the example of tensile fracture initiation Lemiszki et al. (1994) conclude that folding at depths of more than 3000 m requires significant overpressures. However, one drawback in Lemiszki et al.'s (1994) study is the numeric addition of pore pressure to Dieterich and Carter's (1969) model results; the influence of the material's permeability to allow generation of compression related over-pressures and subsequent failure conditions are not considered. In their recent study, using 2D finite element analysis, Eckert et al. (2014) show that conditions of low overburden pressures and/or high viscosities and/or low permeabilities promote the

initiation of tensile fractures parallel to the fold axis and normal to bedding on the fold hinge. Tensile fractures 2 are explained by erosional unloading of high permeability rocks following buckling. However, since the model of Eckert et al. (2014) is 2D, it could not deal with tensile fractures 3.

While Eckert et al.'s (2014) study simulates the buckling associated state of stress under in-situ stress conditions, including pore pressure and permeability, to the authors' knowledge, no numerical modeling study comprehensively and quantitatively has addressed the relation between the conditions of fracture initiation and/or occurrence for various possible fractures (shear and tensile) during the deformation history of buckle folds under stress magnitudes occurring at various depths. The present study utilizes 3D finite element analysis (FEA) using visco-elastic rheology to simulate single-layer buckle fold development of one class of sedimentary rocks under in-situ stress and pore pressure conditions to quantify the evolution of stress during large strain folding and provide further understanding of the relation between fractures and buckle folds. Cylindrical folds are considered since most of the studied fracture sets within buckle folds are based on three-dimensional cylindrical folds (Price and Cosgrove, 1990; Lemiszki et al., 1994; Cosgrove and Ameen, 2000; Fischer and Wilkerson, 2000; Florez-Nio, et al., 2005; Bellahsen et al., 2006; Ismat, 2008; Jager et al., 2008; Sanz et al., 2008). The main objective of this study is to determine the conditions necessary for fractures 1-11 to develop during single layer visco-elastic buckle folding. The influence of material parameters, burial depth, and various boundary conditions are studied to gain a more thorough understanding of the initiation of visco-elastic buckle folding related fractures. If conditions during folding do not support the initiation of specific fracture sets, the influence of post folding erosional unloading is investigated (e.g. Haxby and Turcotte, 1976; Eckert et al., 2014).

2. MODELING APPROACH

2.1. GOVERNING EQUATIONS

Following the studies of Mancktelow (1999), Zhang et al. (2000) and Schmalholz et al. (2001) the visco-elastic behavior of deformed geological materials (e.g.Ramsay and Huber 1987; Turcotte and Schubert, 2002; Fowler 2005) is simulated utilizing a linear Maxwell model. This Maxwell visco-elastic rheology, which exhibits instantaneous elastic response to fast strain rates and time-dependent viscous behavior to slow strain rates, is especially suitable to simulate buckling (Schmalholz et al., 2001). Pore pressure is introduced by utilizing effective stress analysis assuming an incompressible fluid and rock grains (i.e. Biot coefficient $\alpha=1$, Biot and Willis, 1957; Nur and Byerlee, 1971). 3D finite element analysis (via the commercial software package ABAQUS^{TM}) is employed to solve the equations of equilibrium, conservation of mass, constitutive equations, and the equations for pore fluid flow. The unknowns of the problem comprise the stress tensor components σ_{xx}, σ_{yy}, σ_{zz}, σ_{xy}, σ_{xz}, and σ_{yz} , the pore pressure Pp, the material velocities along two horizontal directions v_x, v_y, and vertical direction (z-axis) v_z, and the material density ρ_m.

The equilibrium equations for this model are given by (Eckert et al., 2014):

$$\frac{\partial \sigma_{xx}}{\partial x} - \frac{\partial (\alpha P_p)}{\partial x} + \frac{\partial \sigma_{yz}}{\partial y} + \frac{\partial \sigma_{xz}}{\partial z} = 0 \tag{1}$$

$$\frac{\partial \sigma_{yy}}{\partial y} - \frac{\partial (\alpha P_p)}{\partial y} + \frac{\partial \sigma_{xy}}{\partial x} + \frac{\partial \sigma_{yz}}{\partial z} = 0 \tag{2}$$

$$\frac{\partial \sigma_{zz}}{\partial z} - \frac{\partial (\alpha P_p)}{\partial z} + \frac{\partial \sigma_{xz}}{\partial x} + \frac{\partial \sigma_{yz}}{\partial y} + \rho_m g_z = 0 \tag{3}$$

The constitutive relationships for a compressible Maxwell rheology are:

$$\dot{\varepsilon}_{xx} = \frac{1}{3K}\frac{\partial \sigma_{xx}^{iso}}{\partial t} - \frac{\alpha}{3K}\frac{\partial P_p}{\partial t} + \frac{1}{2G}\frac{\partial \sigma_{xx}^{dev}}{\partial t} + \frac{\sigma_{xx}^{dev}}{2\mu}$$

(4)

$$\dot{\varepsilon}_{yy} = \frac{1}{3K}\frac{\partial \sigma_{yy}^{iso}}{\partial t} - \frac{\alpha}{3K}\frac{\partial P_p}{\partial t} + \frac{1}{2G}\frac{\partial \sigma_{yy}^{dev}}{\partial t} + \frac{\sigma_{yy}^{dev}}{2\mu}$$

(5)

$$\dot{\varepsilon}_{zz} = \frac{1}{3K}\frac{\partial \sigma_{zz}^{iso}}{\partial t} - \frac{\alpha}{3K}\frac{\partial P_p}{\partial t} + \frac{1}{2G}\frac{\partial \sigma_{zz}^{dev}}{\partial t} + \frac{\sigma_{zz}^{dev}}{2\mu}$$

(6)

$$\dot{\varepsilon}_{xy} = \frac{1}{2G}\frac{\partial \sigma_{xy}^{dev}}{\partial t} + \frac{\sigma_{xy}^{dev}}{2\mu}$$

(7)

$$\dot{\varepsilon}_{xz} = \frac{1}{2G}\frac{\partial \sigma_{xz}^{dev}}{\partial t} + \frac{\sigma_{xz}^{dev}}{2\mu}$$

(8)

$$\dot{\varepsilon}_{yz} = \frac{1}{2G}\frac{\partial \sigma_{yz}^{dev}}{\partial t} + \frac{\sigma_{yz}^{dev}}{2\mu}$$

(9)

where K is the Bulk modulus, G the Shear modulus, μ the viscosity, and α the Biot coefficient. The superscript "iso" represents the isotropic part of the stress tensor and "dev" represents the deviatoric part. Since the material density, ρ_m, in the model is depth dependent and depth changes with time, the conservation of mass is represented as:

$$\frac{\partial \rho_m}{\partial t} + \rho_m \left(\frac{\partial v_x}{\partial x} + \frac{\partial v_y}{\partial y} + \frac{\partial v_z}{\partial z} \right) = 0$$

(10)

Fluid flow is simulated using Darcy's law (Jaeger et al., 2007) and since it assumed that $\alpha=1$, the governing diffusion equation for the pore pressure is given by:

$$\frac{Kk_x}{\mu_f}\frac{\partial^2 P_p}{\partial x^2} + \frac{Kk_y}{\mu_f}\frac{\partial^2 P_p}{\partial y^2} + \frac{Kk_z}{\mu_f}\frac{\partial^2 P_p}{\partial z^2} - \frac{\partial P_P}{\partial t} + \dot{\sigma}^{iso} = 0$$

(11)

where k_x, k_y and k_z are the permeabilities along the x, y and z axes, respectively. μ_f stands for the fluid (i.e. water) viscosity. Since the pore pressure response depends on the volumetric strain, the fluid flow is coupled to the strain resulting from pore volume changes. Equations 1 to 11 represent the 11 governing equations to solve for the 11 unknowns of the problem. The detailed derivation of the equation system follows the 2D plane strain approach presented by Eckert et al. (2014) and is slightly modified to account for 3 dimensions.

2.2. MODEL SETUP AND MATERIAL PROPERTIES

Since many natural folds surfaces can be approximated by the cylindrical fold model (Ramsay and Huber, 1987), a three-dimensional cylindrical fold subjected to horizontal shortening (along x-axis) is simulated here. The model geometry comprises a central single folding layer 30 m thick embedded in a less competent matrix with 1000 m initial overburden (Figure 2). The initial geometry of the folding layer is characterized by small periodic perturbations of the appropriate dominant wavelength along the shortening direction (x-axis) and 2.5 m amplitude. The model is horizontally compressed using a strain rate of 10^{-14} s^{-1}, representative of a reasonable geologic deformation rate (Twiss and Moores, 2007). For selecting the appropriate dominant wavelength the same method presented by Eckert et al. (2014) is followed where the parameter R (after Schmalholz and Podladchikov, 1999; Schmalholz et al.,2001) is used to determine if the competent layer is folded viscously (R<1) or elastically (R>1). R is defined as the ratio between the viscous dominant wavelength, λ_{dv}, and the elastic dominant wavelength, λ_{de}:

$$R = \frac{\lambda_{dv}}{\lambda_{de}} = \sqrt[3]{\frac{\mu_l}{6\mu_m}}\sqrt{\frac{P_0}{G}} \tag{12}$$

where G is the shear modulus and P_0 is the initial layer parallel stress. For the range of viscosities μ_l (i.e. 10^{21}- 2×10^{21} Pa s) in the numerical models the initial layer parallel stress is given by $P_0 = 4\mu_f\dot{\varepsilon}$ (Schmalholz and Podladchikov, 1999). With a constant viscosity ratio of 50 (between the folding layer and the matrix; Zhang, et al., 1996; Mancktelow, 1999; Zhang et al., 2000; Eckert et al., 2014) R from equation 12 is in the range of 0.074 to 0.104 and indicates that deformation is dominated by viscous behavior. Therefore, for these models the viscous dominant wavelength $\lambda_{dv} = 2\pi h\sqrt[3]{\frac{\mu_l}{6\mu_m}}$ of 382.2 m is chosen. The final model dimensions are 1720m in the x-direction and 150m in the y-direction.

The model also considers porosity and permeability changes with depth and this planar anisotropy follows the plane of bedding during buckling. The relations between porosity and permeability are expressed as (after Medina et al., 2011):

$$\varphi(z) = 16.39e^{-0.00039z} \tag{13}$$

$$k(z) = 7.583 \cdot 10^{-17} e^{0.283\phi} \tag{14}$$

where ϕ is the porosity, z is the depth in m and k is the permeability in m^2. Hydrostatic pore pressure is assigned to the model as an initial condition and the permeability is considered to be anisotropic with the horizontal permeabilities both being 5 times the vertical permeability. Table 1 lists the material parameters used for all models unless specified differently for special cases.

Table 1. Material properties for general sedimentary rocks for the base model (Eckert et al., 2014).

Properties	Folding Layer	Matrix/Overburden/Base
Specific Gravity	2.75	2.75
Viscosity	10^{21} (Pa s)	$2*10^{19}$ (Pa s)
Young's Modulus	$33.7(1-0.1639e^{-0.00039z})$ (GPa)	$3.37(1-0.1639e^{-0.00039z})$ (GPa)
Poisson Ratio	0.25	0.25
Permeability (at 1000 m)	$1.75 \cdot 10^{-15}$ (m^2)	$1.75 \cdot 10^{-15}$ (m^2)
Strain Rate	10^{-14} (s^{-1})	10^{-14} (s^{-1})

A natural system is in a state of continuous quasi-equilibrium. In order to mimic this condition, a stress initialization procedure (following Buchmann and Connolly, 2007; Smart et al., 2009; Eckert and Liu, 2014) is necessary, to precondition the model with stresses of in-situ conditions, before subjecting the model domain to loads designed to induce buckling. The procedure includes a gravitational pre-stressing step (Figure 2a), followed by a second load step applying 50% horizontal shortening along the x-direction with a constant strain rate (10^{-14} s^{-1}) to simulate the one-directional horizontal compression to initiate buckling (Figure 2b). No deformation boundary conditions are applied along the y-direction unless certain fracture sets require such an addition. If conditions for fracture initiation cannot be explained by the buckling process alone, a

third load step simulating erosional unloading (Eckert et al., 2014) is added. In this load step, the magnitude of the gravitational acceleration of the overburden layer is gradually reduced using an erosion/exhumation rate of 1 mm/yr (Burbank, 2002) while conserving the deformation obtained during buckling (Figure 2c).
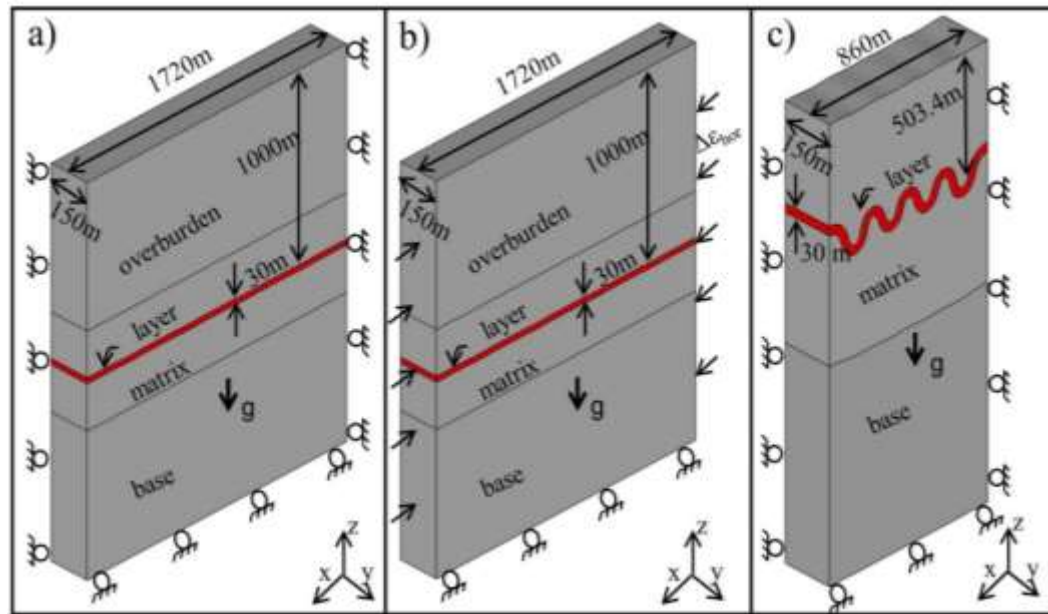
Figure 2. Model setup and boundary conditions for 3D numerical models. a) Pre-stressing boundary conditions allow for in plane displacements during gravitational compaction. The resulting state of stress is used as initial condition for the following load steps. b) A constant tectonic strain rate is applied along the x-axis to initiate buckling. c) Model geometry after the erosional load step. Note model dimensions in Figure 2 are not to scale.

2.3. FRACTURE INITIATION CONDITIONS

In order to evaluate the conditions needed for the initiation of the various fracture sets in Figure 1 the stress evolution during the buckling (and erosion, if necessary) process is analyzed. The likelihood of fracture initiation is evaluated when the stress conditions meet a combined Griffith-Coulomb failure envelope (Hafner, 1951;Chinnery, 1966a and b; Segall and Pollard, 1980; Schultz and Zuber, 1994; Sibson, 2003; Jaeger et al., 2007). It needs to be noted that in order to reduce the number of assumptions about the rocks' tensile and cohesive strengths, the failure criterion is not applied as a plasticity criterion in the finite element analysis but as a post processing indicator of possible

fracture initiation during the various stages of the buckling process. Considering that the study of discrete fractures and their evolution is not part of the objective of this simulation, the post-processing approach of identifying where and when fractures are most likely to initiate is chosen. While this represents a limitation for considering the post failure behavior and stress evolution, this approach enables the study of fracture initiation conditions for various rock strengths, while also limiting the amount of simulations to be run.

The initiation of tensile fractures using the combined Griffith-Coulomb criterion is evaluated when the effective minimum principal stress, σ'_3, equals the tensile strength (T_0) of the rock, i.e. $\sigma'_3 = -T_0$, and when the differential stress is smaller than 4 times the tensile strength, i.e. $\sigma_d < 4T_0$ (Connolly and Cosgrove, 1999). The spatial and temporal evolutions of both the maximum and the minimum effective principal stresses (i.e. σ'_1 and σ'_3) are used to define the stress conditions for shear fracture initiation. For the combined Griffith-Coulomb criterion it has long been recognized that two sets of fractures dominate, shear and extensional. It has also been argued that a third type, extensional shear fractures, are initiated when $4T_0 < \sigma_d < 5.66T_0$ (Secor, 1965; Hancock, 1985; Sibson, 2003), with compressional shear fractures initiated when $\sigma_d > 5.66T_0$ and when:

$$\left(\sigma'_1 - \sigma'_3\right) = 2C_0 \cos\phi + \left(\sigma'_1 + \sigma'_3\right)\sin\phi \qquad (16)$$

where C_0 represents the cohesion with $C_0 = 2T_0$ (Sibson, 2003, Jaeger et al. 2007) and ϕ the angle of internal friction. The angle between the fracture plane and σ'_1 is less for the extensional shear fractures than that of the compressional shear fractures (Sibson, 2003). Note that using a different failure criterion would change the specifics of this distinction. However, since the combined Griffith-Coulomb criterion is the most commonly used one, situations where extensional shear fractures may potentially occur are clearly identified. The orientation of the potential shear fracture is determined by the orientation of the principle stresses. The other failure types can also be analyzed and predicted by the state of stress, however, which is beyond the scope of this study. The reader is then free to use either the two fractures or three fracture systems as appropriate.

It needs to be noted that the models do not consider the existence of pre-existing fractures. The study of pre-existing fractures and their evolution during structural deformation is beyond the scope of this study, Further, it would require a different numerical modeling approach, such as the hybrid discrete finite element method.

3. RESULTS

In order to evaluate the conditions for each fracture set to occur, the stress conditions illustrated in Figure 1 are analyzed for different boundary conditions and material properties. For the following analyses, the angle of internal friction is assumed to be 30° (Jaeger et al., 2007) and two different magnitudes for tensile strength and rock cohesion are chosen to evaluate failure, for strong rock (T_0=6 MPa, C_0=12 MPa) and weak rock (T_0 =3 MPa, C_0=6 MPa) based on experimental data (Bieniawski, 1984; Goodman, 1989; Dubey, 2006). It should be noted that for the following results sections only parameter variations that contribute to conditions resulting in fracture initiation are presented.

The results for the various fracture sets and the conditions for their initiation are summarized and listed in Table 2. The timing of the fracture initiation is given in terms of the dimensionless amplitude A_n, which represents the ratio of fold amplitude over layer thickness, i.e. A_n=A/H, where A is the fold amplitude and H is the layer thickness (Schmalholz and Podladchikov, 2001). Detailed descriptions are presented for Sets 2, 5, 6, and 11 (highlighted in grey in Table 2). Sets 1 and 4 are described in detail in Eckert et al. (2014) and documented for the 3D models in the Appendix. Sets 3, 7, 8, 9, and 10 are described in the Appendix as their initiation during buckling requires "unrealistic" boundary conditions.

Table 2. List of boundary conditions, load steps and model/rock properties needed for each fracture set to be initiated.

Set	Necessary boundary conditions and load steps	Model/rock properties	Comments
1	Buckling due to horizontal compression (along x-axis)	Low permeability or low overburden conditions	Fracture 1 initiated at A_n=0.61 (25 % shortening) for strong rocks (T_0=6 MPa); earlier for weaker rocks; detailed analysis of Fracture 1 can be found in Eckert et al. (2014).

Table 2. List of boundary conditions, load steps and model/rock properties needed for each fracture set to be initiated (cont.).

2	Buckling due to horizontal compression (30-50% shortening along x-axis) plus erosional unloading step	High permeability	Fracture 2 initiated only for strong rocks in folds with $A_n=0.77$ (30 % shortening) shortening. Folds with larger shortening and weak rocks result in shear fractures of Set 10.
3	Buckling due to horizontal compression (50% shortening along x-axis) plus 30-50 % extension along y-axis	High and low permeability	Unrealistic conditions; more likely to represent pre-buckling feature or post-buckling deformation under a different stress field.
4	Buckling due to horizontal compression (along x-axis)	Low permeability	Fracture 4 initiated at $A_n=0.02$ (1-2 % shortening) for weak and strong rocks.
5	Buckling due to horizontal compression (along x-axis)	High and low permeability, low overburden	Set 5 initiated at $A_n=0.43$ (~20% shortening) for weak rocks ($C_0=6$ MPa); for strong rocks ($C_0=6$ MPa) low overburden and/or low permeability promote the initiation of Set 5.
6	Buckling due to horizontal compression (along x-axis)	Increased folding layer viscosity (2×10^{21} Pa·s)	Set 6 is initiated at $A_n=0.43$ (20% shortening) for weak rocks ($T_0=3$ MPa) and at $A_n=0.47$ (21 % shortening) for stronger rocks ($T_0=6$ MPa).

Table 2. List of boundary conditions, load steps and model/rock properties needed for each fracture set to be initiated (cont.).

7	Buckling due to horizontal compression (50% shortening along x-axis) plus 50 % extension along y-axis	High and low permeability	During the very early stages of horizontal compression ($A_n=0.02$, ~1.5% shortening) the differential stress is large enough and σ'_3 small enough such that for weak rocks Set 7 can be initiated
8	Buckling due to horizontal compression (50% shortening along x-axis) plus 40 % compression along y-axis	High and low permeability	Set 8 is possible to be initiated when $A_n=0.66$ (~ 20% shortening) at the hinge zone of folds for relative weak rocks (6 MPa $>T_0>$3 MPa).
9	Buckling due to horizontal compression (50% shortening along x-axis) plus 50 % extension along y-axis	High and low permeability	Set 9 can be initiated at $A_n=0.40$ (~36% shortening) for rocks in the range of 5.5 MPa$>T_0>$3 MPa. For stronger rocks tensile fractures (Fracture 3) are initiated.
10	Buckling due to horizontal compression (30-50% shortening along x-axis) plus erosional unloading step	High permeability	Set 10 is likely to occur during erosional unloading for folds with 35%-50% shortening for strong rocks ($0.77<A_n<1.23$).
11	Buckling due to horizontal compression (along x-axis)	Low permeability and low overburden	Set 11 is possible to be initiated during buckling in the fold limb for a weak rock ($T_0=3$ MPa)

3.1. TENSILE FRACTURE 2

Similar to the 2D results of Eckert et al. (2014), tensile stress does not develop in the fold limb during buckling and the addition of erosional unloading is necessary to explain widespread tensile stress magnitudes in the fold limb for high permeability rocks (for folds with up to 40% shortening). The 3D stress evolution during the erosional unloading step (Figure 3a) confirms the initiation of Fracture 2 when erosion is applied after 30% shortening (A_n=0.77) for strong rocks (T_0=6 MPa), as the differential stress remains < $4T_0$ (solid line in Figure 3d). Tensile stress magnitudes are widespread across the fold limb and σ'_3 orientations (Figure 3g) indicate tensile fractures which are approximately perpendicular to the bedding near the hinge, and at a lower angle to bedding in the fold limb (red solid line in Figure 3g). In contrast to Eckert et al.'s (2014) results, which predict Fracture 2 in general without considering the differential stress, this study can only explain the initiation of Fracture 2 for strong rocks at A_n=0.77, i.e. 30% shortening (solid black line in Figure 3d). For weaker rocks, compressional shear fractures of Set 10 are initiated prior to tensile fractures 2 as σ_d>$5.66T_0$ (dashed line in Figure 3d).

If erosion occurs after 30% of shortening, the resulting differential stress becomes larger and extensional shear fractures similar to Set 10 are/could be initiated prior to tensile fractures 2 as $4T_0$<σ_d<$5.66T_0$ (solid line Figure 3e and 3f; red dashed line in Figure 3h and 3i) for strong rocks (T_0=6 MPa). For weaker rocks (T_0=3 MPa), compressional shear fractures of Set 10 are initiated prior to tensile fractures 2 as σ_d>$5.66T_0$ (dashed line Figure 3e and 3f; black dotted line in Figure 3h and 3i).

3.2. SHEAR FRACTURE SET 5

In order to investigate the initiation of compressive faults (fracture Set 5; Figure 1) the effective principal stresses at the bottom of the fold hinge for various overburden thicknesses and permeabilities are shown in Figure 4. Figure 4a shows the temporal evolution of σ'_1 and σ'_3 for a model featuring 1000 m overburden depth and high permeability rock, i.e. k=10^{-13} m^2 (base model, solid lines in Figure 4a), for a model featuring 500 m overburden depth and high permeability rock, i.e. k=10^{-13} m^2 (dash line
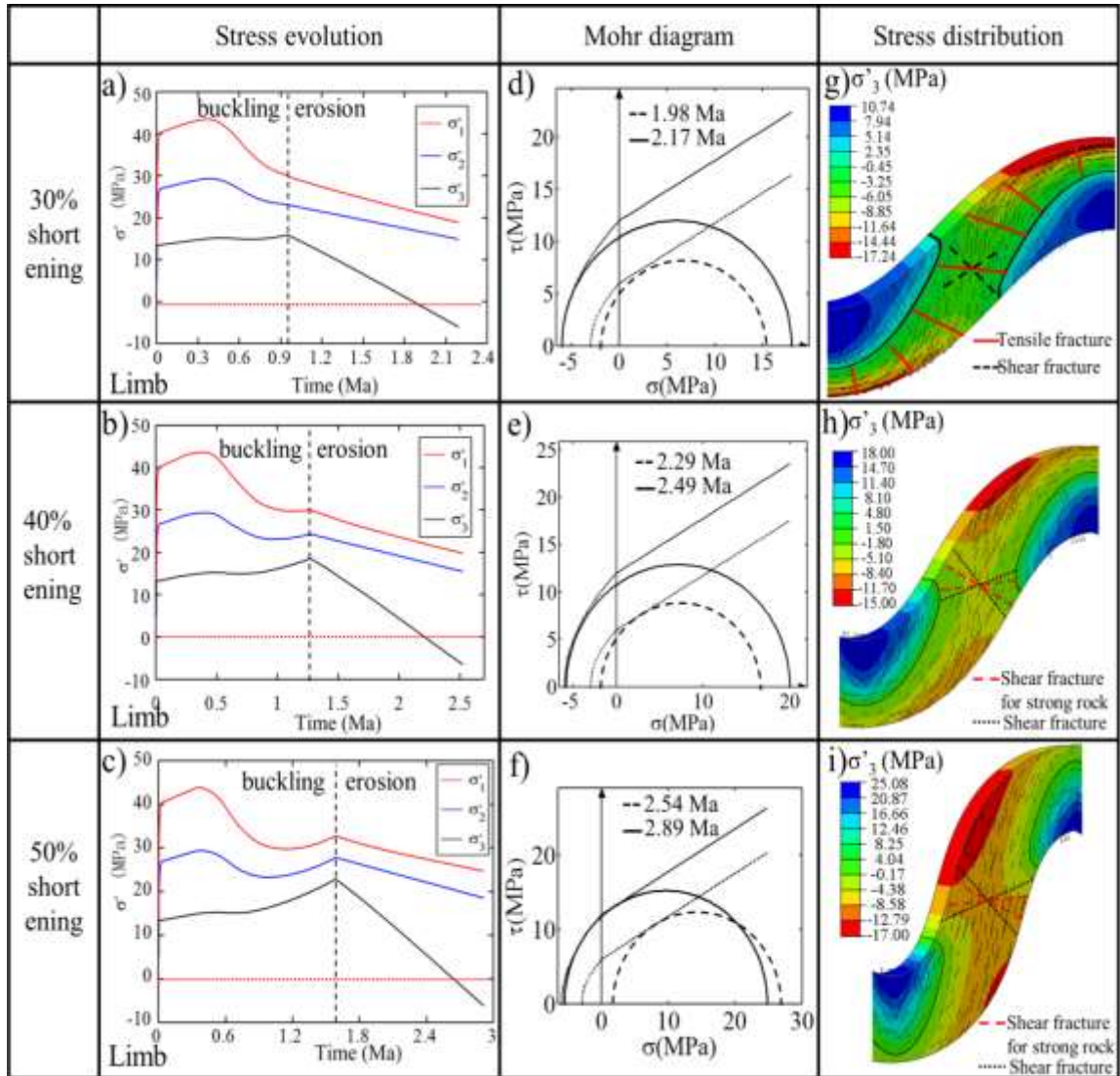
Figure 3. a-c) Evolution of the effective principal stresses at the fold limb during buckling (30-50% shortening) and erosional unloading. The red dotted line represents zero principal stress. d-f) Mohr diagram based on the state of stress at various times after erosion for different rock strengths of T_0=6 MPa (solid line, $4T_0 < \sigma_d < 5.66T_0$) and T_0=3 MPa (dashed line, $\sigma_d > 5.66T_0$). g-i) σ'_3 magnitudes after 2.19 ma (g), 2.5 ma (h), and 2.97 ma (i) of exhumation. The black line separates compressive from tensile stresses. The red lines indicate the location and orientation of possible tensile fractures. The dotted black lines indicate possible conjugate shear fractures, and the dashed red lines indicate possible extensional faults.

in Figure 4a), for a model featuring 1000 m overburden depth and low permeability rock, i.e. k=10^{-21} m^2 (dotted lines in Figure 4a) and for a model featuring 1000 m overburden depth and a high viscosity contrast, i.e. R_μ=100 (dash-dotted lines in Figure 4a). The

Mohr circle plots in Figure 4b are plotted for the value of A_n which features the largest differential stress. The Mohr circles show that Set 5 is likely to be initiated under all conditions considered for weak rocks (C_0=6 MPa). For stronger rocks (C_0= 12 MPa), conditions of lower overburden pressure and/or low permeability promote the initiation of Set 5. It is observed that the high viscosity ratio, which results in a much larger A_n, has little influence on the magnitude of differential stress at the bottom of the hinge. The principal stress orientations confirm that σ'_1 is horizontal and σ'_3 is vertical at the bottom of the hinge zone (Figure 4c). These findings are in agreement with compressional strain/stress patterns in the fold hinge zone and multiple field studies (e.g. Price and Cosgrove, 1990; Lemiszki et al., 1994; Reber et al., 2010; Frehner, 2011).
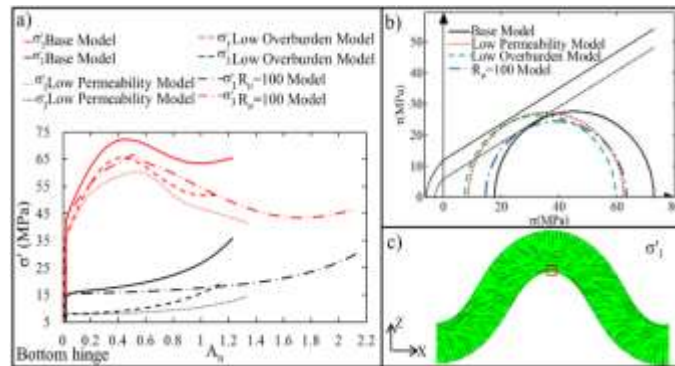
Figure 4. Results of effective principal stress at the bottom of the fold hinge. a) Effective principal stresses for the base model (high permeability with initial 1000 m overburden depth; solid line) and the low permeability model (k=10^{-21} m^2; dotted line) and the low overburden model (initial 500 m; dashed line). b) Mohr diagram based on the state of stress which features the largest differential stress for base model (solid line) and low permeability model (dotted line) and low overburden model (dashed line) and Griffith-Coulomb failure criterion for T_0=3 MPa (dotted line) and T_0=6 MPa (solid line). c) Orientation of the maximum principal stress of the folding layer and the bottom of the fold hinge is highlighted by red color.

3.3. SHEAR FRACTURE SET 6

Extensional faults (Set 6) are most likely to be initiated at the top the hinge where σ'_3 is parallel to the shortening direction and σ'_1 is vertical (Figure 4c). It is observed that the stress conditions for the models based on the material parameters given in Table 1 promote the initiation of tensile fractures (Fracture 1), as the differential stress is insufficient for shear failure (auxiliary material and Figure F01). However, a slightly

higher folding layer viscosity (2×10^{21} Pa·s), with a folding layer : matrix viscosity ratio of 50, enables the initiation of this fracture set. The increase in viscosity results in a steep decrease of σ'_3 (Figure 5a) after A_n=0.32 (around 16% shortening) resulting in σ_d>$4T_0$. For weak rocks (i.e. T_0=3 MPa), σ_d is larger than $5.66T_0$ after A_n=0.43 (around 20% shortening) and fracture Set 6 is initiated as compressional shear fractures. For strong rocks (i.e. T_0=6 MPa), after A_n=0.47 (around 21% shortening), fracture Set 6 is/could be initiated as extensional shear fractures since $4T_0$<σ_d <$5.66T_0$. It is important to note that the relatively high differential stress (for the model featuring the increased viscosity), especially after A_n=0.43 (i.e. 20% shortening), is the reason that extensional fault Set 6 occurs at the top hinge instead of tensile fractures 1. The larger differential stress can be explained by the increase of the factor R when the viscosity is increased, resulting in a more elastic response and thus larger stress magnitudes.
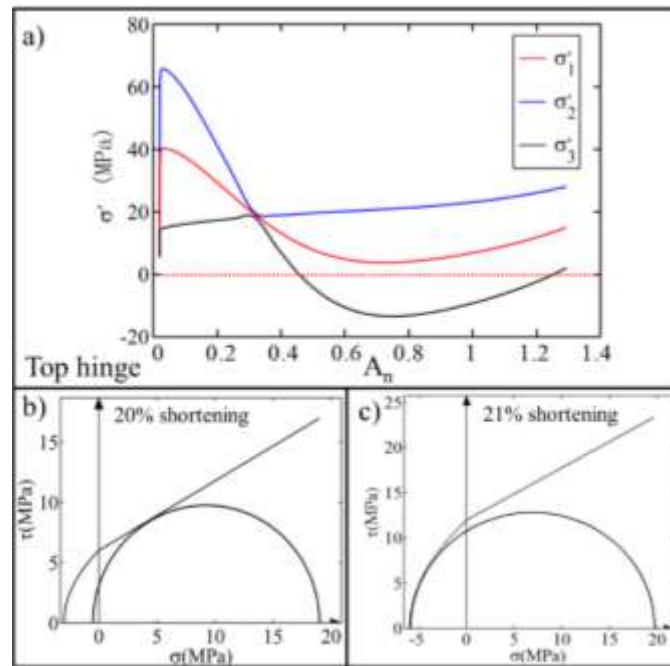
Figure 5. a) Results of the effective principal stress at the top of the fold hinge for the high viscosity model (2×10^{21} Pa·s in the folding layer). The red dotted line represents zero principal stress. b) Mohr diagram based on the state of stress at A_n=0.43 (20% shortening) and Griffith-Coulomb failure criterion for T_0=3 MPa and σ_d >$5.66T_0$. c) Mohr diagram based on the state of stress at A_n=0.47 (21% shortening) and Griffith-Coulomb failure criterion for T_0=6 MPa and $4T_0$<σ_d <$5.66T_0$.

3.4. SHEAR FRACTURE SET 11

Shear fracture Set 11 in the fold limb requires similar orientations of principal stresses as Set 5 for the fold hinge, which indicates that the maximum effective principal stress is sub-parallel to the bedding plane. The stress evolution for the base model featuring high permeability and 1000 m overburden thickness (dashed lines in Figure 6) show that σ'_3 is too large to initiate shear failure during buckling. In order to reduce the compressional stresses, a model with low overburden (500 m) and low permeability (10^{-21} m^2) is analyzed. For these conditions (solid lines in Figure 6), shear fracture Set 11 is possible to be initiated during buckling in the fold limb for a weak rock (T_0=3 MPa). These findings are in agreement with compressional strain/stress pattern in the fold limb and multiple field studies (e.g. Price and Cosgrove, 1990; Lemiszki et al., 1994; Reber et al., 2010).
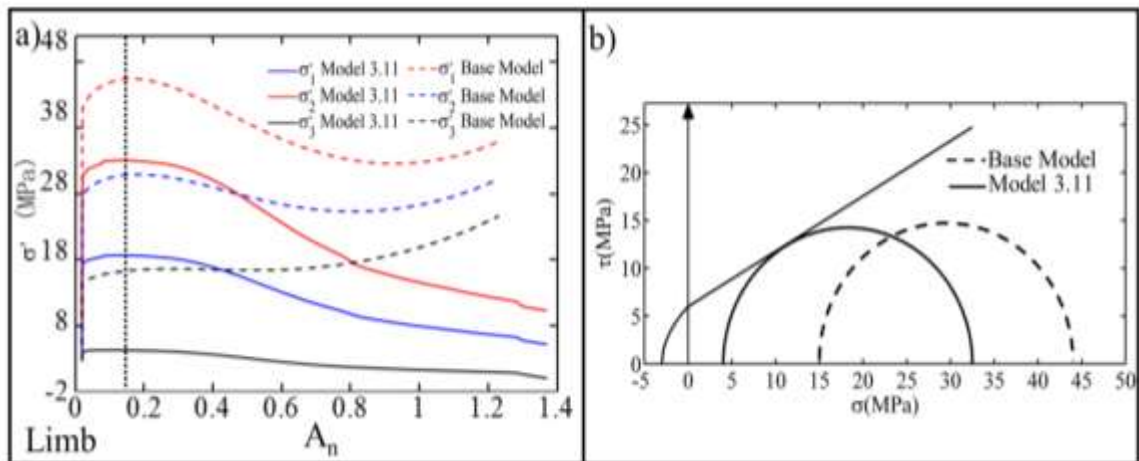
Figure 6. a) Results of the effective principal stress at the fold limb for Model 3.11 (low permeability and low overburden depth; solid line) and for the base model (initial 1000 m overburden and high permeability; dashed line). b) Mohr diagram based on the state of stress at A_n=0.16 (~12% shortening) for Model 3.11 (solid line) and base model (dashed line) and Griffith-Coulomb failure criterion for T_0=3 MPa.

4. SUMMARY

The 3D modeling approach presented in this study shows that the stress history during the development of visco-elastic cylindrical single layer buckle folds can be successfully simulated for in-situ stress and pore pressure conditions and help provide a better understanding of the initiation of various types of fractures as recorded for folded outcrops (e.g. Price and Cosgrove, 1990; Bergbauer and Pollard, 2004; Reber et al., 2010). As pointed out by Eckert et al. (2014), permeability and post folding deformation processes such as erosional unloading play a key role in understanding fracture initiation for single layer buckle folds. Since Eckert et al.'s (2014) study was 2D, it considered only the initiation of tensile fractures. The initiation of shear fractures was not investigated. Based on the analysis of the simulation results presented here, the fracture systems of Sets 1 – 11 (Figure 1) can be classified into three groups. The conditions for fracture initiation of each group are summarized in Table 3).

- Group I includes fractures that are characterized by the strong dependence on the distribution of model and material parameters (i.e. burial depth, viscosity and permeability) during the process of buckling, including: tensile fractures 1 and extensional fault Set 6 at the top of the hinge zone, tensile fractures 4 throughout the folding layer, thrust fault Set 5 at the bottom of the hinge zone, and shear fracture Set 11 in the fold limb.

- Group II includes fractures that require extensional or compressional boundary conditions along the fold axis, such as tensile fractures 3, extensional fault Set 9, and strike-slip fault Set 8 at the top of the hinge zone, and oblique strike-slip fault Set 7 in the limb of the folding layer. This suggests that fractures of Group II, especially Fracture 3 and Set 9 are likely to represent pre-folding/post-folding features.

- Group III is unlikely to be initiated during buckling and the process of erosional unloading is confirmed as a very likely cause. Tensile fractures 2 and oblique extensional fault Set 10 in the limb belong to this group.

Table 3. Summary of fracture sets in Groups I-III.

Group	Loading/Deformation conditions during buckling	Sets	Comments
I	Buckling due to horizontal compression (along x-axis)	1, 4, 5, 6, 11	Buckling fractures: Fracture initiation of different sets is dependent on material properties (permeability and viscosity), initial overburden pressure, and rock strength during buckling.
II	Buckling due to horizontal compression (along x-axis) and a) 30-50 % extension along y-axis b) 40 % compression along y-axis	3, 7, 9 8	Fracture initiation of different sets during buckling requires unrealistic deformation. Possible explanations: a) Periclinal geometry may explain Set 7 (see 5.2). b) Periclinal geometry may explain Set 8 (see 5.2). c) Fractures likely represent pre-folding or post folding deformation.
III	Buckling due to horizontal compression (30-50% shortening along x-axis) plus erosional unloading step	2, 10	Erosional fractures: Fracture 2 initiated only for strong rocks in folds with $A_n \sim 0.77$, i.e. 30 % shortening. Folds with larger shortening and weak rocks result in shear fractures of Set 10.

5. DISCUSSION

5.1. GROUP I FRACTURES

Comparison of Sets 1 and 6, which can both be initiated during the buckling process at the top of the hinge zone, shows that the material properties determine what type of fracturing occur at the top of the fold hinge. Fracture 1 is only likely to occur for low overburden pressure (initial 500m) and/or low permeability (10^{-21} m^2) rock, which results in tensile stress in a strong rock ($T_0=6$ MPa, Figure 3) by overcoming the compressional state of stress generated by the overburden pressure. These findings are equivalent to the 2D plane strain model results presented by Eckert et al. (2014) and consistent with their conclusions. In addition to being initiated during buckling, fractures of Fracture 1 can also occur during erosional unloading as presented by Eckert et al. (2014), which explains the frequent observation of this fracture set in field outcrops. Set 6 is initiated for fold layers with a high viscosity (2×10^{21} Pa·s), resulting in a more elastic response and greater differential stress during buckling (Figure 8). In addition to the dependence on the viscosity, Set 6 is also sensitive to the rock strength and the amount of shortening. For weak rocks (3 MPa $<T_0<6$ MPa), Set 6 is initiated as an extensional fault at $A_n=0.43$ (~20% shortening). For stronger rocks, Set 6 is initiated as an extensional fracture of mixed modes 1 and 2 at $A_n=0.47$ (~ 21% shortening).

Fracture 4 is initiated during the initial stages of horizontal compression for impermeable rocks (10^{-23} m^2) with low overburden pressure (500 m) and low rock strength ($T_0=3$ MPa). These results are consistent with those of Eckert et al. (2014).

Set 5 (thrust fault at the bottom of the hinge) is likely to be initiated for weak rocks ($C_0=6$ MPa) independent of permeability. For stronger rocks ($C_0=2T_0=12$ MPa), conditions of lower overburden pressure and/or low permeability promote the initiation of Set 5. It should be noted that the largest differential stress for the initiation of Set 5 occurs at only $A_n=0.43$ (20% shortening, see Figure 7), which makes Set 5 a feature possible in low amplitude folds.

Set 11(shear fracture in the limb) is only likely to be initiated for conditions of low overburden thickness (500 m) and low permeability (10^{-21} m^2) during the early stages of buckling (i.e. $A_n=0.16$, ~12% shortening, Figure 6) for weak rocks ($T_0=3$ MPa). These

limiting conditions confirm the rare observations of this fracture set in natural examples (Price and Cosgrove, 1990).

5.2. GROUP II FRACTURES

The initiation of fracture sets 3, 7, and 9 requires σ'_3 to be parallel to the fold axis, a stress condition which is difficult to develop during cylindrical single-layer buckle folding, where σ'_3 is mostly layer parallel or layer perpendicular on the plane perpendicular to the fold axis (Price and Cosgrove, 1990; Eckert et al., 2014). The models presented show that additional boundary conditions up to 50% extension along the fold axis are necessary to establish such stress conditions. This represents an extremely unrealistic deformation scenario. Therefore, these fracture sets are likely to represent a pre-folding or post-folding feature for cylindrical buckle folds.

In particular Fracture 3, which is frequently observed in natural buckle fold examples (Price and Cosgrove, 1990; Fischer and Wilkerson, 2000; Engelder et al., 2009), can be characterized as a pre-folding joint set common in sedimentary rocks (Price, 1966; Price and Cosgrove, 1990; Engelder, et al., 2009).

Fracture Set 7 is frequently observed in natural fold examples (Price and Cosgrove, 1990) and may represent a pre-folding strike-slip fracture during horizontal compression prior to buckling.

For Set 8, σ'_1 is parallel to the fold axis, which in the numerical models is achieved after 40% shortening along the fold axis. This stress condition can be considered uncommon during buckling as layer parallel shortening is the main driving force for deformation. These boundary conditions also represent an extremely unrealistic deformation scenario, which confirms the infrequent observations of this fracture set (Price and Cosgrove, 1990). This also suggests that Set 8 is likely to represent a pre-folding or post-folding feature.

5.3. GROUP III FRACTURES

Group III (Fracture 2 and Set 10) cannot be explained by buckling. In their recent study, Eckert et al. (2014) propose that the addition of an erosional unloading step after buckling can explain the initiation of tensile fractures 2 penetrating the fold limb for folds which have undergone 40% of shortening. While Eckert et al. (2014) show that during

erosional unloading sufficient tensile effective stresses are generated in the fold limb, their study does not consider the differential stress evolution. The results of this 3D modeling study show that Fracture 2 may only be initiated when erosion is applied for low amplitude folds (i.e. A_n=0.77, 30% shortening) for strong rocks (T_0=6 MPa), as the differential stress remains $< 4T_0$. However, based on the stress orientation during erosion, the resulting tensile fracture is not layer perpendicular but at a high angle (Figure 3g). For weaker rocks, shear fractures of Set 10 are initiated instead of tensile fractures 2 as σ_d>5.66T_0 (dashed lines in Figure 3d to 3f). Hence, Eckert et al.'s (2014) results presented for folds with 40% shortening may only be valid for very strong rocks (T_0> 6.5 MPa).

Figure 7a, b shows the Mohr circle, stress orientations and associated fracture orientations for such a scenario. If erosion occurs for high amplitude folds (i.e. A_n=1.02, 40% shortening and more), the resulting differential stress in the fold limb becomes larger (i.e. $4T_0<\sigma_d$) and shear fractures similar to Set 10 are initiated prior to tensile fracture 2. For the shear fractures, one set of the conjugate failure planes is perpendicular to bedding. Hence, if such fractures are mapped in the field, slip indicators need to be recorded or these shear fractures might be mistaken as tensile fracture 2.

These observations promote the conclusion that Fracture 2 may only be initiated for specific conditions (i.e. high rock strength or low amplitude folds) during erosional unloading of buckle folds (e.g. conditions presented in Eckert et al., 2014) and is more likely a pre-folding feature (Engelder et al., 2007; Berbauer and Pollard, 2004).
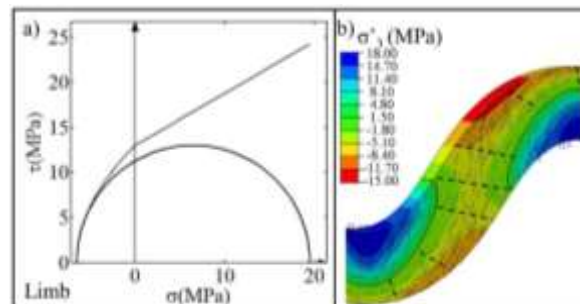
Figure 7. a) Mohr diagram based on the state of stress at 2.19 ma with Griffith-Coulomb failure criterion for T_0=6.5 MPa. c) σ'_3 magnitudes after 2.19 ma of exhumation with orientation of tensile failure (dashed lines). The black line separates compressive from tensile stresses.

5.4. NUMERICAL SIMULATION OF SINGLE LAYER PERICLINE

Since the conditions for initiation of fracture Set 7 in the numerical models presented are unrealistic, alternate model scenarios need to be considered to provide an explanation for the occurrence of this frequently observed fracture set in field outcrops (Price and Cosgrove, 1990). A possible solution can be obtained by considering the geometry of single layer pericline structures (Campbell, 1958). The periclinal geometry is described by the ratio of the fold half wavelength to the hinge length along the fold axis (Cosgrove and Ameen, 2000), which was found to vary between 0.1 and 0.2 for the majority of buckle folds (Dubey and Cobbold, 1977; Blay et al. 1977).

In order to simulate a 3D pericline geometry using the numerical modeling approach described in Section 2, a small periodic perturbation is assigned to the initial geometry along the fold axis direction (y-axis) with a wavelength of 2.5 times the viscous dominant wavelength. 50% shortening is applied along the x-direction (i.e. buckling direction), while the y-direction is constrained to in-plane displacements (Figure 8). These boundary conditions result in a 3D periclinal geometry with an aspect ratio of 0.2 after 50% of shortening, confirming these previous studies (e.g. Ramsay and Huber, 1987; Abbassi and Mancktelow, 1992; Ghosh et al., 1995; Schmalholz, 2008) which show that non-cylindrical three-dimensional fold shapes can form during a single, unidirectional shortening event. The model setup is shown in Figure 8 with material properties as listed in Table 1. Furthermore, an erosional unloading step using a constant rate of 1 mm/yr is applied over a period of 1.37 Ma (Figure 8b). The final 3D geometry of the pericline is shown in Figure 18c. Figure 8c also depicts 2 cross sections, A & B, along the hinge line and along the shortening direction with the maximum fold amplitude, respectively.

In order to identify locations for the initiation of fracture Set 7, the orientations of the principal stresses at various locations in the pericline structure are analyzed. Figure 9 a-d shows the orientations of σ'_1 and σ'_3 and their magnitude evolution after buckling and erosional unloading respectively along cross section A. In the fold limb (Element 1 in Figure 8c), σ'_1 is always oriented along the shortening direction (Figure 9a-c). σ'_3 orientations are dependent on the amount of shortening during buckling. σ'_3 is vertical to sub-vertical before 25% shortening (i.e. A_n=0.94, Figure 9d), and switches to parallel to
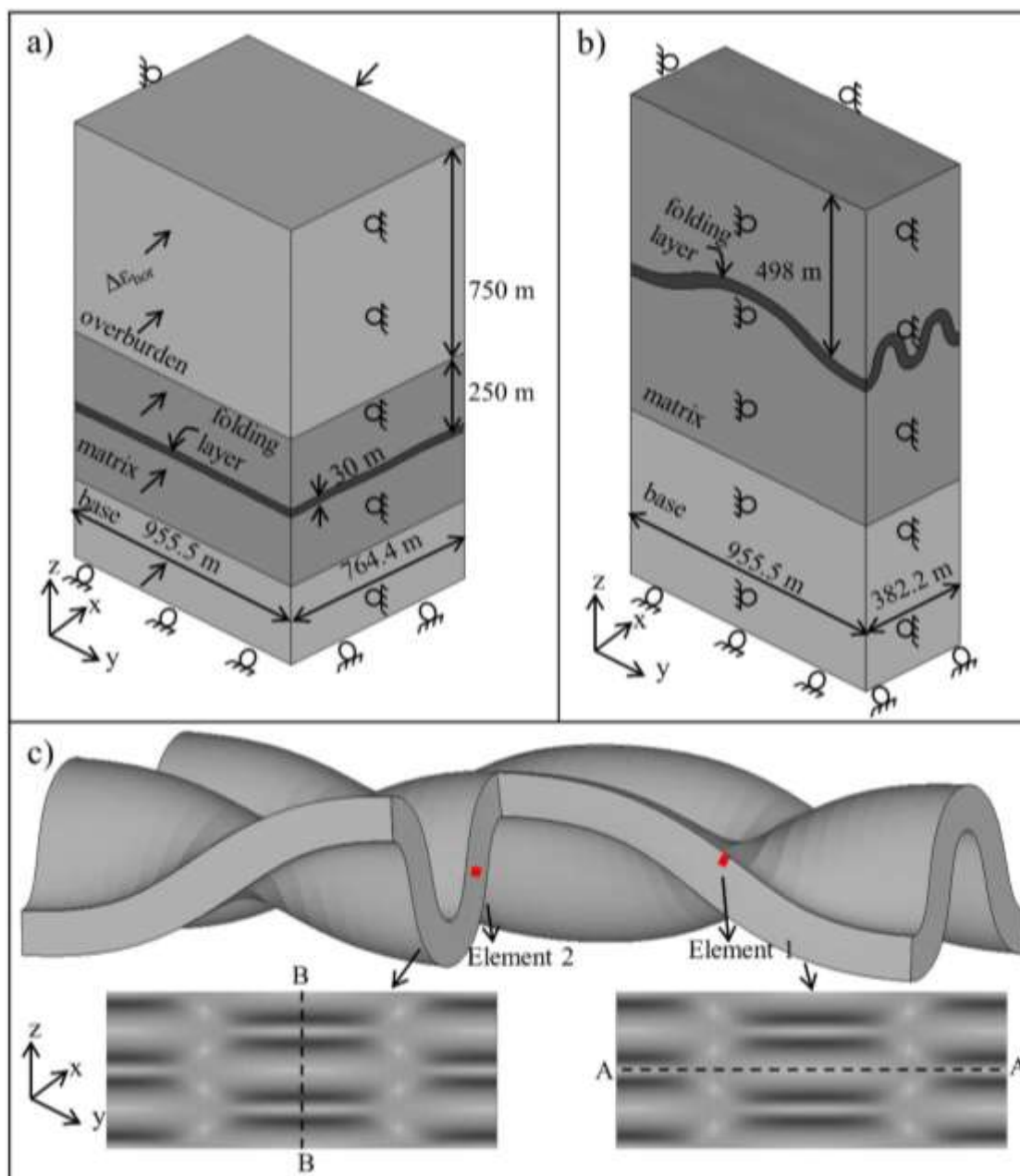
Figure 8. a) Model setup for the pericline geometry. The folding layer is embedded in a 250m thick high permeable matrix. The remaining overburden and base also have a high permeability. b) Model geometry and dimensions after the erosional load step with 50% shortening applied during buckling along the x-axis. (c) Resulting pericline geometry after buckling showing two cross sections, A along the fold axis and B parallel to shortening along the maximum fold amplitude. Element 1 is at the top of the limb of cross section A and Element 2 is at the center of the limb of cross section B.

the hinge line (Figure 9e) after 28.6% shortening and maintains this direction during erosion (Figure 9f). Hence, after 28.6% (i.e. A_n=1.06) shortening and during erosion, favorable orientations for fracture Set 7 are present. Yet, for the model parameters considered (1000 m overburden thickness, high permeability), fracture Set 7 is unlikely to be initiated during buckling as the σ'_3 magnitude is too high (Figure 9e) and the associated Mohr circle (solid line Mohr circle in Figure 9h) is far from failure, even for weak rocks (i.e. T_0=3 MPa). During erosional unloading, σ'_3 decreases and the differential stress increases (Figure 9g), thus enhancing the likelihood for Set 7 to be initiated for both strong and weak rocks as compressional shear fractures (σ_d >5.66T_0, see dashed and dash-dotted Mohr circles in Figure 9h). In conclusion, Set 7 most likely represents formation during erosion. The changing orientations of σ'_3 in the limb during erosion indicate that Set 7 is only initiated at the top of the limb. Pericline structures forming in scenarios with lower rock permeability and lower overburden loads may result in lower σ'_3 magnitudes during buckling (Eckert et al., 2014) and thus Set 7 may be initiated for high amplitude folds, i.e. >28.6% shortening, during buckling. Moreover, different aspect ratios of the pericline structure may also result in different degrees of compression and extension in the various sections of the structure. In order to verify these influences, extensive sensitivity analyses on the formation of 3D periclines are necessary and these are beyond the scope of this contribution.

It is interesting to note that the conditions for Set 7 to be initiated only occur along cross section A and do not occur along cross section B (featuring the largest fold amplitude), where σ'_1 is parallel to the hinge line. This is in agreement with fracture patterns presented by Cooper et al. (2004) which show an increased frequency of fracture Set 7 away the location represented by cross section B.

In addition to providing an explanation for Set 7, the pericline model can also be used to explain conditions possible for the initiation of Set 8. The analysis of the principal stress orientations and magnitudes in the limb of cross section B (Element 2 in Figure 8c) show that after 29.7% shortening (A_n=1.09), the σ'_1 direction switches from parallel to the shortening direction (Figure 10a) to parallel to the fold axis during buckling (Figure10b) and during erosion (Figure 10c), hence providing favorable orientations for
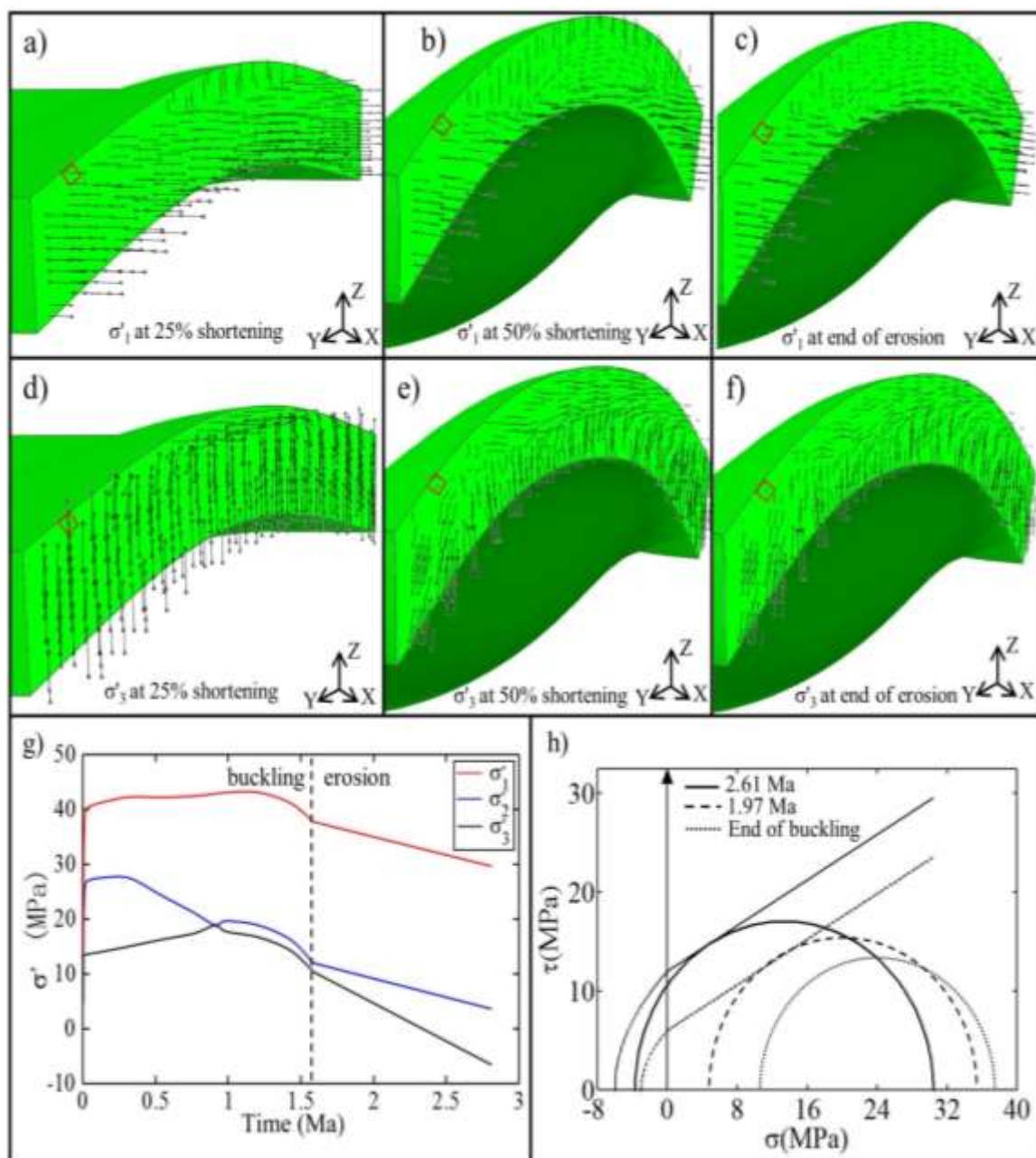
Figure 9. a-f) Stress orientations along cross section A. a) σ'_1 orientation at 25% shortening/A_n=0.94. b) σ'_1 orientation after buckling. c) σ'_1 orientation after erosion. d) σ'_3 orientation at 25% shortening. e) σ'_3 orientation after buckling. f) σ'_3 orientation after erosion. g) Evolution of effective principal stress at Element 1 during buckling and erosional unloading. h) Mohr diagram based on the state of stress at the end of buckling (dotted line) and at 1.97 ma with Griffith-Coulomb failure criterion for T_0=3 MPa (dashed line) and at 2.61 ma for T_0=6 MPa (solid line). It should be noted that all featured stress orientations on the cross section are either perpendicular to or in the plane of the cross section. The oblique view is used for better visualization.

Set 8. As for Set 7, Set 8 is unlikely to be initiated during buckling because the σ'_3 magnitude is too high (Figure 10e) and the associated Mohr circle (solid line dash dotted Mohr circle in Figure 10f) is far from weak rock failure (i.e. $T_0=3$ MPa). During erosional unloading, σ'_3 decreases and the differential stress increases (Figure 10g), thus enhancing the likelihood that Set 8 is initiated as either compressional shear fracture in weak rocks ($\sigma_d > 5.66T_0$, dashed Mohr circles in Figure 9h) or extensional shear fracture in strong rocks ($4T_0 < \sigma_d < 5.66T_0$, solid Mohr circles in Figure 9h) in association with erosion of high amplitude folds.

It should be noted that the principal stresses shown in Figure 9 and 10 only represent 2 cross-sections through the pericline structure. However, the stress orientations throughout the 3D geometry of the pericline are far more complex than that of a cylindrical fold. This indicates that the geometry of periclines may provide additional or different conditions for the various fracture sets observed in the field. Documenting such relations requires detailed analyses of different pericline geometries. This is beyond the scope of this paper, but very tractable using the numerical simulation method presented here.

5.5.LIMITATIONS

One limitation of the majority of the 3D finite element modeling results presented here is the single-layer cylindrical fold geometry simulated. This geometry is adopted to enable simple comparison with previously documented fracture sets associated with cylindrical buckle folds. While the 3D geometry presented enables more sophisticated and detailed analysis of the spatio-temporal evolution of stress state in the folding layer when compared to 2D models (e.g. Eckert et al., 2014), a detailed analysis of the conditions for all fractures associated with buckle folds is restricted since one of the principal stresses is always sub-parallel to the fold axis. As shown in principle in Section 4.2, periclinal geometries may offer a better explanation for certain fracture sets (e.g. Set 7). Besides the shape of the fold, the influence of a multilayer geometry also has implications for the stress distribution and the resulting conditions for fracture initiation. However, multilayer fold geometries may either feature less competent layers embedded
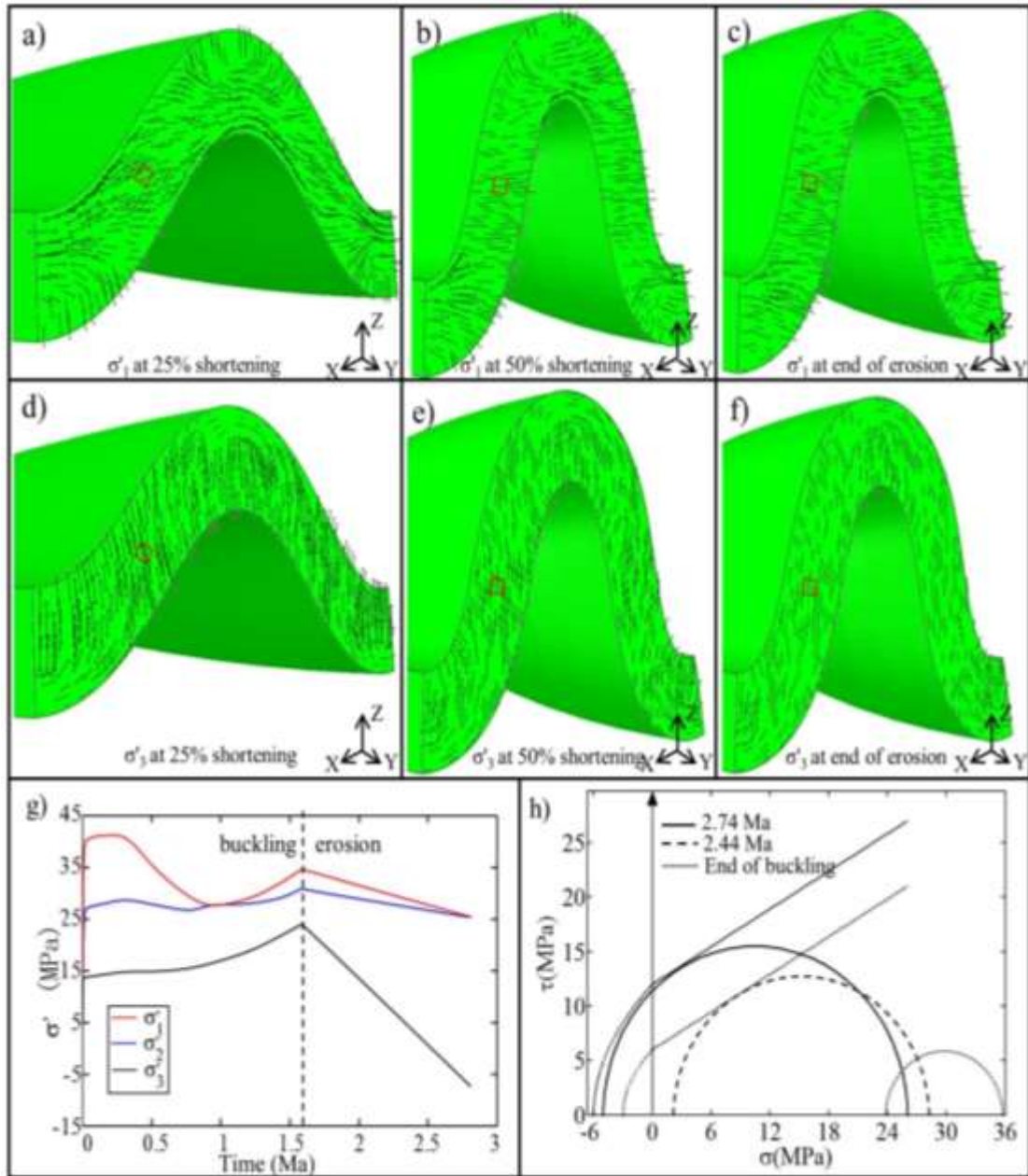
Figure 10. a-f) Stress orientations along cross section B. a) σ'_1 orientation at 25% shortening/A_n=0.94. b) σ'_1 orientation after buckling. c) σ'_1 orientation after erosion. d) σ'_3 orientation at 25% shortening. e) σ'_3 orientation after buckling. f) σ'_3 orientation after erosion. g) Evolution of effective principal stress at Element 2 during buckling and erosional unloading. h) Mohr diagram based on the state of stress at the end of buckling (dotted line) and at 2.44 ma with Griffith-Coulomb failure criterion for T_0=3 MPa (dashed line, $\sigma_d > 5.66T_0$) and at 2.74 ma for T_0=6 MPa (solid line, $4T_0 < \sigma_d < 5.66T_0$). It should be noted that all featured stress orientations on the cross section are either perpendicular to or in the plane of the cross section. The oblique view is used for better visualization.

within competent layers (true multilayer; Schmid and Podladchikov, 2006) or may feature several mechanical units within a stiff single layer (effective single layer; Schmid and Podladchikov, 2006), and thus require an extensive comparison which is beyond the scope of this contribution. In addition, in a recent study based on 2D finite element analysis, Liu et al. [2015] compared the stress evolution of single-layer and true multilayer buckle folds. They showed that the multilayer geometry has some influence on the stress distribution but the general picture of how fractures are initiated during buckle folding remains the same as for a single layer.

Another important limitation of the numerical method employed is the omission of plastic deformation. When rocks fail, strain softening (Goodman, 1989) or hardening (Fjaer et al., 2008) may occur and the post-yield evolution of the stress state will affect fracture propagation and distribution. Moreover, the induced fractures represent regions of increased permeability which in turn significantly affect the resulting effective stress evolution. However, the main purpose of this study is to focus on and pinpoint the relationship between the structural development of single layer buckle folds and the associated spatial and temporal initiation of various fractures. Therefore, the post processing indicators based on the combined Griffith Coulomb failure criteria are considered reasonable for studying the initiation of buckle fold related fractures. An advantage of this approach is the possibility to consider rocks of various strengths without making assumptions about the subsequent yield behavior (hardening or softening) of the rock.

In the models involving the erosional load step, isothermal processes are assumed and thus thermal stresses due to cooling during exhumation are not included. Clearly, the addition of a changing temperature field (particularly for high geothermal gradient regions) is required in order to investigate specific geological scenarios. These specific features are beyond the scope of this contribution, but are very tractable using the methodology presented. Lastly, a detailed understanding of the strain history of structures in the field is necessary such that a robust comparison of the numerical results and field observations can be made.

6. CONCLUSIONS

The 3D numerical models presented here illustrate that a thorough understanding of the interplay between material properties, model boundary conditions and model strain history is necessary in order to better understand and make reasonable predictions about the initiation of fracture associated with large-scale buckle fold systems. Based on the presented stress evolution during single-layer viscoelastic buckling this study confirms the conclusion that not all observed fractures are likely to form during one folding event (Price and Cosgrove, 1990; Cosgrove and Ameen, 2000). Moreover, the results of the numerical simulations provide a quantitative analysis of the relationship between fracture initiation and buckle folding and a general understanding of the timing of their formation. The conditions necessary for initiation of fracture Sets 1-11 during single layer buckle folding are analyzed and related to the stress evolution during buckle folding and erosional unloading, and are summarized in Figure 11. The 3D numerical modeling results show that fractures can be categorized in 3 groups:

- Group I specifies fractures that are directly related to the stress conditions during the process of buckling and are likely to be initiated during folding. Group I fracture sets are characterized by the strong dependence on the distribution of material parameters and include tensile fractures 1 and fracture Sets 4, 5, 6, and 11.

- Group II represents fractures (i.e. sets 3, 7, 8, and 9) that are thought to represent pre-folding features. Their initiation during buckling requires extensional or compressional boundary conditions along the (cylindrical) fold axis, indicating that these fractures, especially Fracture 3 and Set 9 are unlikely to be initiated during folding. For Set 7 and 8, 3D pericline geometries may help to understand the stress conditions for their initiation. The state of stress in the 3D pericline models considered is more complex and fracture sets with various orientations (beyond the orientations listed in Figure 1) are likely to be initiated during buckling.

- Group III fractures are unlikely to be initiated during buckling and the process of erosional unloading is confirmed as a very likely cause. Tensile fracture 2 and oblique extensional fault Set 10 in the limb belong to this group. It can be concluded that this

group of fractures can be attributed to the stress evolution during pre-folding or post-folding.

In summary, this study has shown that the conditions for the initiation of fractures commonly associated with buckle folds can be explained by a combination of dependence on material properties, post buckling processes such as erosional unloading and non-cylindrical pericline geometries. Fractures that cannot be explained by the stress conditions during buckling likely represent pre-folding or post-folding features.

Group	Fracture Set	Conditions during buckling	Other Conditions	Rock Strength
Group I	Tensile Fracture 1 (hinge)	Low overburden and/or low permeability	N/A	Strong rock (T_0=6MPa)
	Tensile Fracture 4 (hinge and limb)	Low permeability and low overburden during early stage of buckling		Strong rock (T_0=6MPa)
	Shear Fracture Set 5(hinge)	Low overburden and low permeability		Weak rock (T_0=3MPa)
	Shear Fracture Set 6(hinge)	High viscosity		Less strong rock (T_0<6MPa)
	Shear Fracture Set 11(limb)	Low permeability and low overburden depth		Weak rock (T_0=3MPa)
Group II	Tensile Fracture 3 (hinge)	High extensional boundary condition along fold axis	Pre-folding	Strong rock (T_0=6MPa)
	Shear Fracture Set 7(limb)	High extensional boundary condition along fold axis	Pre-folding or Pericline	Less strong rock (T_0<6MPa)
	Shear Fracture Set 8(hinge)	High compressional boundary condition along fold axis		Less strong rock (T_0<6MPa)
	Shear Fracture Set 9(hinge)	High extensional boundary condition along fold axis	Pre-folding	Weak rock (T_0=3MPa)
Group III	Tensile Fracture 2 (limb)	N/A	Erosional unloading	Strong rock (T_0=6MPa)
	Shear Fracture Set 10(limb)	N/A		Weak rock (T_0=3MPa)

Figure 11. Conditions for the initiation of the various fracture sets associated to cylindrical buckle folds.

ACKNOWLEDGMENTS

REFERENCES

Abbassi, M.R. and Mancktelow, N.S., 1992. Single layer buckle folding in non-linear materials—I. Experimental study of fold development from an isolated initial perturbation. Journal of Structural Geology, 14(1), 85-104.

Ameen, M. S., 1988. Folding of layered cover due to dip-slip basement faulting (Doctoral dissertation, Imperial College London (University of London)).

Ameen, M. S., 1990. Macrofaulting in the Purbeck-Isle of Wight monocline. Proceedings of the Geologists' Association, 101(1), 31-46.

Ameen, M. S., 1992. Strain pattern in the Purbeck-Isle of Wight monocline: A case study of folding due to dip-slip fault in the basement. In Basement Tectonics 8 (pp. 559-578). Springer Netherlands.

Awdal, A. H., Braathen, A., Wennberg, O. P., Sherwani, G. H., 2013. The characteristics of fracture networks in the Shiranish formation of the Bina Bawi Anticline; comparison with the Taq Taq field, zagros, Kurdistan, NE Iraq.Petroleum Geoscience, 19(2), 139-155.

Bai, T., Pollard, D. D., 2000. Fracture spacing in layered rocks: a new explanation based on the stress transition. Journal of Structural Geology, 22(1), 43-57.

Barbier, M., Hamon, Y., Callot, J. P., Floquet, M., Daniel, J. M., 2012. Sedimentary and diagenetic controls on the multiscale fracturing pattern of a carbonate reservoir: The Madison Formation (Sheep Mountain, Wyoming, USA). Marine and Petroleum Geology, 29(1), 50-67.

Bellahsen, N., Fiore, P., Pollard, D. D., 2006. The role of fractures in the structural interpretation of Sheep Mountain Anticline, Wyoming. Journal of Structural Geology, 28(5), 850-867.

Bergbauer, S., Pollard, D. D., 2004. A new conceptual fold-fracture model including prefolding joints, based on the Emigrant Gap anticline, Wyoming. Geological Society of America Bulletin, 116(3-4), 294-307.

Bieniawski Z. T., 1984. Rock Mechanics Design in Mining and Tunnelling, Balkema, Rotterdam,pp. 272.

Blay, P. K., Cosgrove, J. W. Summers, J. M. 1977. An experimental investigation of the development of structures in multilayers under the influence of gravity. Journal of the Geological Society, London, 133, 329-342.

Biot, M. A., 1961, Theory of folding of stratified viscoelastic media and its implications in tectonics and orogenesis. Geological Society of America Bulletin, 72(11), 1595-1620.

Biot, M. A., Willis, D. G.,1957, The elastic coefficients of the theory of consolidation. Journal of Applied Mechanics, 24, 594-601.

Bourne, S. J., 2003. Contrast of elastic properties between rock layers as a mechanism for the initiation and orientation of tensile failure under uniform remote compression. Journal of Geophysical Research: Solid Earth (1978–2012), 108(B8).

Buchmann, T. J., Connolly, P. T., 2007. Contemporary kinematics of the Upper Rhine Graben: a 3D finite element approach. Global and Planetary Change, 58(1), 287-309.

Burbank, D. W., 2002. Rates of erosion and their implications for exhumation. Mineralogical Magazine, 66(1), 25-52.

Campbell, J. D., 1958. "En Echelon" Folding: Economic Geology, v. 53, pp. 448-472.

Casey, M., Butler, R. W., 2004. Modelling approaches to understanding fold development: implications for hydrocarbon reservoirs. Marine and Petroleum Geology, 21(7), 933-946.

Catherine, L. H., Lorenz, J., Lawrence, T. I., 1997. Lithological and structural controls on natural fracture distribution and behavior with in the Lisburne group, northeastern Brooks Range and north slope subsurface, Alaska. American Association of Petroleum Geologists Bulletin, 81(10), 1700-20.

Chapple, W. M., Spang, J. H., 1974. Significance of layer-parallel slip during folding of layered sedimentary rocks. Geological Society of America Bulletin, 85(10), 1523-1534.

Chinnery, M., 1966a. Secondary faulting: I. Theoretical aspects. Canadian Journal of Earth Sciences, 3(2), pp.163-174.

Chinnery, M.A., 1966b. Secondary faulting: II. Geological aspects. Canadian Journal of Earth Sciences, 3(2), pp.175-190.

Cloos, H.,1948, Gang und Gehwerk einer Falte. Zeitschrift Deutsche Geologische Gesellschaft,100,290-303.

Cobbold, P. R., Zanella, A., Rodrigues, N., Løseth, H., 2013. Bedding-parallel fibrous veins (beef and cone-in-cone): Worldwide occurrence and possible significance in terms of fluid overpressure, hydrocarbon generation and mineralization. Marine and Petroleum Geology, 43, 1-20.

Connolly P., Cosgrove, J., 1999. Prediction of static and dynamic fluid pathways within and around dilational jogs, Fractures, Fluid Flow and Mineralization, Editors: McCaffrey, Geological Society, London, Special Publications, 155:105-121, doi:10.1144/GSL.SP.1999.155.01.09

Cooke, M.L., Mollema, P.N., Pollard, D.D. and Aydin, A., 1999. Interlayer slip and joint localization in the East Kaibab Monocline, Utah: field evidence and results from numerical modelling. Geological Society, London, Special Publications, 169(1), 23-49.

Cooke, M. L., Underwood, C. A., 2001. Fracture termination and step-over at bedding interfaces due to frictional slip and interface opening. Journal of Structural Geology, 23(2), 223-238.

Cooper, S. P., Goodwin, L. B., Lorenz, J. C., 2006. Fracture and fault patterns associated with basement-cored anticlines: The example of Teapot Dome, Wyoming. American Association of Petroleum Geologists Bulletin, 90(12), 1903-1920.

Cosgrove, J. W., Ameen, M. S., 2000. A comparison of the geometry, spatial organization and fracture patterns associated with forced folds and buckle folds, in: Cosgrove, J. W., Ameen, M. S.(eds), Forced Folds and Fractures. Geological Society, London, Special Publications, 169(1), 7-21.

Cosgrove, J. W., Ameen, M. S., 2000. Forced Folds and Fractures. Geological Society of London.

Couples, G. D., Lewis, H., 1999. Effects of interlayer slip in model forced folds. Geological Society, London, Special Publications, 169(1), 129-144.

Dieterich, J. H., 1969. Origin of cleavage in folded rocks. American Journal of Science 267: 155-65.

Dieterich, J. H., Carter, N. L., 1969, Stress history of folding, American Journal of Science, 267:129-154

Dubey, A. K., Cobbold, P. R., 1977. Non-cylindrical flexural slip folds in nature and experiment. Tectonophysics, 38, 223-239.

Dubey, R.K., 2006. Mechanical response of Vindhyan Sandstones under drained and confined conditions. In Rock Mechanics in Underground Construction: ISRM International Symposium 2006: 4th Asian Rock Mechanics Symposium, 8-10 November 2006, Singapore.

Dunne, W. M., 1986. Mesostructural development in detached folds: an example from West Virginia. The Journal of Geology, 473-488.

Eckert A., Liu, X., 2014. An improved method for numerically modeling the minimum horizontal stress magnitude in extensional stress regimes. International Journal of Rock Mechanics and Mining Sciences, 9(70):581–592. DOI: 10.1016/j.ijrmms.2014.04.020

Eckert, A., Connolly, P., Liu, X. 2014. Large-scale mechanical buckle fold development and the initiation of tensile fractures. Geochemistry, Geophysics, Geosystems, 15(11), 4570-4587.

Engelder, T., Lash, G. G.,Uzcátegui, R. S., 2009. Joint sets that enhance production from Middle and Upper Devonian gas shales of the Appalachian Basin. American Association of Petroleum Geologists Bulletin, 93(7), 857-889.

Ericsson, J. B., McKean, H. C., Hooper, R. J., 1998. Facies and curvature controlled 3D fracture models in a Cretaceous carbonate reservoir, Arabian Gulf. Geological Society, London, Special Publications, 147(1), 299-312.

Ferrill, D. A., Morris, A. P., 2003. Dilational normal faults. Journal of Structural Geology, 25(2), 183-196.

Fischer, M.P., Wilkerson, M.S., 2000. Predicting the orientation of joints from fold shape: results of pseudo-three-dimensional modeling and curvature analysis. Geology 28, 15–18.

Florez-Nio, J. M., Aydin, A., Mavko, G., Antonellini, M., Ayaviri, A., 2005. Fault and fracture systems in a fold and thrust belt: An example from Bolivia. American Association of Petroleum Geologists Bulletin, 89(4), 471-493.

Fowler, C.M.R., 2005. The Solid Earth, Cambridge University Press, Cambridge, 557-577.

Frehner, M., 2011. The neutral lines in buckle folds. Journal of Structural Geology: 33(10), 1501-1508.

Ghosh, S.K., Khan, D. and Sengupta, S., 1995. Interfering folds in constrictional deformation. Journal of Structural Geology, 17(10), 1361-1373.

Ghosh, K., Mitra, S., 2009. Structural controls of fracture orientations, intensity, and connectivity, Teton anticline, Sawtooth Range, Montana. American Association of Petroleum Geologists Bulletin, 93(8), 995-1014.

Groshong, R. H., 1975. Strain, fractures, and pressure solution in natural single-layer folds. Geological Society of America Bulletin, 86(10), 1363-1376.

Guiton, M. L., Sassi, W., Leroy, Y. M., Gauthier, B. D., 2003. Mechanical constraints on the chronology of fracture activation in folded Devonian sandstone of the western Moroccan Anti-Atlas. Journal of Structural Geology,25(8), 1317-1330.

Goodman, R. E., 1989. Introduction to rock mechanics (2nd ed). New York: John Wiley & Sons: 80-84.

Hafner, W., 1951. Stress distribution and faulting. Bulletin of the Geological Society of America 62, 373–398.

Hancock, P.L., 1985. Brittle microtectonics: principles and practice. Journal of structural geology, 7(3), 437-457.

Haxby, W. F., Turcotte, D. L., 1976. Stresses induced by the addition or removal of overburden and associated thermal effects. Geology, 4(3), 181-184.

Hennings, P. H., Olson, J. E., Thompson, L. B., 2000. Combining outcrop data and three-dimensional structural models to characterize fractured reservoirs: An example from Wyoming. American Association of Petroleum Geologists Bulletin, 84(6), 830-849.

Iñigo, J. F., Laubach, S. E., Hooker, J. N., 2012. Fracture abundance and patterns in the Subandean fold and thrust belt, Devonian Huamampampa Formation petroleum reservoirs and outcrops, Argentina and Bolivia. Marine and Petroleum Geology, 35(1), 201-218.

Ismat, Z., 2008. Folding kinematics expressed in fracture patterns: An example from the Anti-Atlas fold belt, Morocco. Journal of Structural Geology, 30(11), 1396-1404.

Jaeger, J. C., N. G. Cook, Zimmerman, R. W., 2007. Fundamentals of Rock Mechanics. Blackwell Publishing Ltd, Oxford, UK, pp. 90-91;185-187.Jäger, P., Schmalholz, S. M., Schmid, D. W., and Kuhl, E., 2008. Brittle fracture during folding of rocks: A finite element study. Philosophical Magazine, 88(28-29), 3245-3263.

Laubach, S. E., Schultz-Ela, D. D., and Tyler, R., 1999. Differential compaction of interbedded sandstone and coal. Geological Society, London, Special Publications, 169(1), 51-60.

Lemiszki, P. J., Landes, J. D., Hatcher, R. D., 1994. Controls on hinge‐parallel extension fracturing in single‐layer tangential‐longitudinal strain folds. Journal of Geophysical Research: Solid Earth (1978–2012), 99(B11), 22027-22041.

Lisle, R. J., 1992. Constant bed-length folding: three-dimensional geometrical implications. Journal of Structural Geology, 14(2), 245-252.

Lisle, R. J., 1994. Detection of zones of abnormal strains in structures using Gaussian curvature analysis. American Association of Petroleum Geologists Bulletin, 78(12), 1811-1819.

Liu, X., Eckert, A., Connolly, P. 2015. A Comparison of Stress Evolution in Single-layer and Multilayer Buckle Folds. ARMA 49th US Rock Mechanics/ Geomechanics American Rock Mechanics Association Symposium. San Francisco, CA, p. ARMA 219.

Mancktelow, N. S., 1999. Finite-element modelling of single-layer folding in elasto-viscous materials: the effect of initial perturbation geometry. Journal of Structural Geology, 21(2), 161-177.

Mancktelow, N. S,. 2008. Tectonic pressure: theoretical concepts and modelled examples. Lithos, 103(1), 149-177.

McQuillan, H., 1973, Small-scale fracture density in Asmari Formation of southwest Iran and its relation to bed thickness and structural setting, American Association of Petroleum Geologists Bulletin,57(12),2367-2385.

McQuillan, H., 1974. Fracture patterns on Kuh-e Asmari anticline, southwest Iran. American Association of Petroleum Geologists Bulletin, 58(2), 236-246.

Medina, C. R., Rupp, J. A., Barnes, D. A., 2011. Effects of reduction in porosity and permeability with depth on storage capacity and injectivity in deep saline aquifers: A case study from the Mount Simon Sandstone aquifer. International Journal of Greenhouse Gas Control, 5(1), 146-156.

Nur, A., and Byerlee, J., 1971, An exact effective stress law for elastic deformation of rock with fluids. Journal of Geophysical Research, 76(26), 6414-6419.

Parrish, D. K., Krivz, A. L., Carter, N. L., 1976. Finite-element folds of similar geometry. Tectonophysics, 32(3), 183-207.

Perritt, S. H., Watkeys, M. K., 2003. Implications of late Pan-African shearing in western Dronning Maud Land, Antarctica. Geological Society, London, Special Publications, 210(1), 135-143.

Price, N. J., 1966. Fault and joint development in brittle and semi-brittle rock (Vol. 1). Oxford: Pergamon Press, pp.113-117;148-156.

Price N. J. Cosgrove, J. W., 1990. Analysis of Geological Structures, Cambridge University Press, UK, pp.378-383.

Ramsay, J. G., 1967. Folding and Fracturing of Rocks. McGraw-Hill, New York, pp. 372-386; 398; 401.

Reber, J. E., S. M. Schmalholz, Burg, J. P., 2010. Stress orientation and fracturing during three-dimensional buckling: Numerical simulation and application to chocolate-tablet structures in folded turbidites, SW Portugal, Tectonophysics, 493(1), 187-195, doi: 10.1016/j.tecto.2010.07.016.

Richard, P., 1989. Champs de failles au dessus d'un décrochement de socle: modélisation expérimentale (Doctoral dissertation, Université Rennes).

Richard, P., 1991. Experiments on faulting in a two-layer cover sequence overlying a reactivated basement fault with oblique-slip. Journal of Structural Geology, 13(4), 459-469.

Sanz, P. F., Pollard, D.D., Allwardt, P.F., Borja, R.I., 2008. Mechanical models of fracture reactivation and slip on bedding surfaces during folding of the asymmetric anticline at Sheep Mountain, Wyoming. Journal of Structural Geology, v. 30, 1177-1191

Schmalholz, S. M., Podladchikov, Y., 1999. Buckling versus folding: importance of viscoelasticity. Geophysical Research Letters, 26(17), 2641-2644.

Schmalholz, S. M., Podladchikov, Y. Y., 2001. Strain and competence contrast estimation from fold shape. Tectonophysics, 340(3), 195-213.

Schmalholz, S. M., Podladchikov, Y. Y., Schmid, D. W., 2001. A spectral/finite difference method for simulating large deformations of heterogeneous, viscoelastic materials. Geophysical Journal International, 145(1), 199-208.

Schmalholz, S. M., Podladchikov, Y. Y., Burg, J. P., 2002. Control of folding by gravity and matrix thickness: Implications for large‐scale folding. Journal of Geophysical Research: Solid Earth (1978‐2012), 107(B1), ETG-1.

Schmalholz, S. M., 2008. 3D numerical modeling of forward folding and reverse unfolding of a viscous single-layer: Implications for the formation of folds and fold patterns, Tectonophysics, 446(1), 31-41, doi: 10.1016/j.tecto.2007.09.005.

Schmid, D. W., Dabrowski, M., Krotkiewski, M., 2008. Evolution of large amplitude 3D fold patterns: A FEM study. Physics of the Earth and Planetary Interiors, 171(1), 400-408.

Schultz, R.A. and Zuber, M.T., 1994. Observations, models, and mechanisms of failure of surface rocks surrounding planetary surface loads. Journal of geophysical research, 99(E7), 14691-14702.

Segall, P., Pollard, D., 1980. Mechanics of discontinuous faults. Journal of Geophysical Research, (88) 555–568.

Sibson, R. H., 2003. Brittle-failure controls on maximum sustainable overpressure in different tectonic regimes, American Association of Petroleum Geologists Bulletin, 87(6), 901-908.

Silliphant, L. J., Engelder, T., Gross, M. R., 2002. The state of stress in the limb of the Split Mountain anticline, Utah: constraints placed by transected joints. Journal of Structural Geology, 24(1), 155-172.

Smart, K. J., Ferrill, D. A., Morris, A. P., 2009. Impact of interlayer slip on fracture prediction from geomechanical models of fault-related folds. American Association of Petroleum Geologists Bulletin, 93(11), 1447-1458.

Smart, K. J., Ferrill, D. A., Morris, A. P., Bichon, B. J., Riha, D. S., Huyse, L., 2010. Geomechanical modeling of an extensional fault-propagation fold: Big Brushy Canyon monocline, Sierra Del Carmen, Texas. American Association of Petroleum Geologists Bulletin, 94(2), 221-240.

Smart, K. J., Ferrill, D. A., Morris, A. P., McGinnis, R. N., 2012. Geomechanical modeling of stress and strain evolution during contractional fault-related folding. Tectonophysics, 576, 171-196.

Stearns, D. W., 1968. Certain aspects of fracture in naturally deformed rocks. In Rock mechanics seminar, (1) 97-118.

Stephansson, O., 1974. Stress-induced diffusion during folding, Tectonophysics, 22(3), 233-251.

Stephenson, B. J., Koopman, A., Hillgartner, H., McQuillan, H., Bourne, S., Noad, J. J., Rawnsley, K., 2007. Structural and stratigraphic controls on fold-related fracturing in the Zagros Mountains, Iran: implications for reservoir development. Geological society, London, special publications, 270(1), 1-21.

Tavani, S., Storti, F., Lacombe, O., Corradetti, A., Muñoz, J. A., Mazzoli, S., 2015. A review of deformation pattern templates in foreland basin systems and fold-and-thrust belts: Implications for the state of stress in the frontal regions of thrust wedges. Earth-Science Reviews, 141, 82-104.

Turcotte, D. L., and Schubert, G., 2002. Geodynamics, Cambridge University Press, New York, pp. 112-118;251-254..

Twiss, R.J., Moores, E.M., 2007. Structural Geology, 2nd Edition, W.H. Freeman and Company, New York, pp. 48-550;240;381-383.Vitale, S., Dati, F., Mazzoli, S., Ciarcia, S., Guerriero, V., Iannace, A., 2012. Modes and timing of fracture network development in poly-deformed carbonate reservoir analogues, Mt. Chianello, southern Italy. Journal of Structural Geology, 37, 223-235.

Watkins, H., Butler, R. W., Bond, C. E., Healy, D., 2015. Influence of structural position on fracture networks in the Torridon Group, Achnashellach fold and thrust belt, NW Scotland. Journal of Structural Geology, 74, 64-80.

Wennberg, O. P., Svånå, T., Azizzadeh, M., Aqrawi, A. M. M., Brockbank, P., Lyslo, K. B., Ogilvie, S., 2006. Fracture intensity vs. mechanical stratigraphy in platform top carbonates: the Aquitanian of the Asmari Formation, Khaviz Anticline, Zagros, SW Iran. Petroleum Geoscience, 12(3), 235-246.

Zhang, Y., Hobbs, B. E., Ord, A., Mühlhaus, H. B., 1996. Computer simulation of single-layer buckling. Journal of Structural Geology, 18(5), 643-655.

Zhang, Y., Mancktelow, N. S., Hobbs, B. E., Ord, A., Mühlhaus, H. B., 2000. Numerical modelling of single-layer folding: clarification of an issue regarding the possible effect of computer codes and the influence of initial irregularities. Journal of Structural Geology, 22(10), 1511-1522.

II. VISCO-ELASTIC MULTILAYER BUCKLE FOLDING: RESULTING FOLD SHAPES AND THEIR STRESS AND STRAIN DISTRIBUTION

Xiaolong Liu

Department of Geosciences and Geological and Petroleum Engineering, Missouri University of Science and Technology, Rolla, Missouri, USA.

Andreas Eckert

Department of Geosciences and Geological and Petroleum Engineering, Missouri University of Science and Technology, Rolla, Missouri, USA.

Peter Connolly

Chevron ETC, 1500 Louisiana St, Houston, TX 77002. USA.

ABSTRACT

Multilayer folds represent common structures and the various fold shapes feature a complex stress/strain distribution. How the stress/strain distribution develops during the buckling of multilayer folds remains unclear. In this study, a 2-D plane strain finite element modeling approach is used to simulate multilayer, viscoelastic buckle folds under in-situ stress and pore pressure conditions. A variety of material and model parameters (including the elastic modulus contrast, viscosity contrast, initial overburden, number of layers, and layer thickness ratio) are considered and their influence on the shape of folds and on the resulting stress/strain distribution is analyzed. This study demonstrates that the shapes of the multilayer folds are influenced by the various parameters. The numerical modeling results show that tensile stress occurs at the hinge and the region between the hinge and the limb for certain layers and are influenced by the material and model parameters by various degree. In addition, the numerical simulations provide a general understanding of the strain distribution in the multilayer system where the less competent layers exhibit a large variability in the maximum principal strain distribution. This study shows that the thickness ratio of the competent and less competent layers has a major impact on the fold shapes and resulting stress/strain distribution for viscoelastic multilayer folding.

1. INTRODUCTION

Multilayer buckle folds represent common structures of layered rocks undergoing compression and show a large variability in fold shapes on different scales (e.g. Price and Cosgrove, 1990). Understanding the mechanics of multilayer buckle folding and the associated stress and strain distribution is essential for an improved comprehension of tectonic deformation processes (Schmalholz and Schmid, 2012) and of associated fluid flow such as hydrocarbon migration (Sibson, 1996). Numerous studies have been performed on multilayer buckle folding (e.g. theoretical: Biot, 1961 and 1965, Johnson, 1969; Ghosh, 1970; Johnson and Fletcher, 1994; analogue: Ghosh, 1968; Ramberg, 1970; Cobbold et al., 1971; Ramberg and Strömgard, 1971; numerical: Debremaecker and Becker, 1978; Casey and Huggenberger, 1985; Schmalholz et al., 2001; Schmid and Podlachikov, 2006; Hunt et al. 2006; Treagus and Fletcher, 2009), with respect to the dominant wavelength selection, fold amplification rate, and fold shape. The structural development of multilayer folds during buckling has been extensively studied by either considering the competent and incompetent layers as separate objects (e.g. Biot, 1961; 1965), or treating the multilayer system as a homogeneous, but anisotropic body by applying average properties (e.g. Biot and Romain, 1965; Cobbold et al. 1971; Johnson and Ellen, 1974; Casey, 1976; Hobbs et al., 2001; Mühlhaus et al., 2002).

Although fold amplification in multilayer folds is understood to be mainly dependent on the viscosity contrast (e.g. Johnson and Fletcher, 1994), and the number of layers and the ratio of competent layer thickness to incompetent layer thickness (e.g. Ramsay and Huber, 1987; Schmid and Podladchikov, 2006), it cannot directly be used to explain the resulting fold shapes. Compared to single-layer folds, Hudleston and Treagus (2010) conclude that multiple factors result in the large variation of multilayer folds shapes, including sinusoidal, chevron, kinks and conjugate/box folds. In particular, observed fold shapes in multilayers are found to be dependent on the amount of bulk shortening (Schmalholz et al., 2001), layer thickness (Ramsay and Huber, 1987; Schmid and Podlachikov, 2006), the rheology applied (Schmalholz and Schmid, 2012), the viscosity ratio (Ramberg, 1962; Sherwin and Chapple, 1968; Ramsay and Huber, 1987), and the type of active folding (Price and Cosgrove, 1990). As stated and summarized by

Hudleston and Treagus (2010), "the large variation in shape of multilayer folds suggests that shape may potentially provide much more information on mechanical properties than has so far been achieved."

With respect to the description of the resulting state of strain/stress, various studies have been conducted for viscous multilayer folding. Mazzoli and Caremolla (1992) numerically study the principal strains in both the competent and less competent layer in a three-layer multilayer system. They conclude that fold limbs and hinges show complex deformation paths, with the principal axes of the total deformation ellipsoid interchanging their position several times during fold development. A later numerical study by Frehner and Schmalholz (2006) conducts a detailed analysis of the strain distribution (using finite strain ellipses) of a three-layer fold system (i.e. two competent layers and one less competent layer), and the two competent layers are found to form parallel folds. While the strain distribution in the competent layers is similar to strain observed for single layer folds (i.e. neutral surfaces separating compression from extension; e.g. Twiss and Moores, 2007; Frehner, 2010), the less competent layer shows layer-parallel shearing and layer-perpendicular compaction in the limb and pure shear at the hinge.

Although the development of multilayer buckle folds has been extensively studied for elastic and viscous materials, the viscoelastic behavior of deformed geological materials (e.g. Ramsay and Huber, 1987; Turcotte and Schubert, 2002; Fowler, 2005; Mühlhaus et al. 2002) has not been widely considered for multilayer folds. Schmalholz and Podladchikov (1999, 2001) have shown the importance of viscoelastic rheology with respect to the dominant wavelength selection in single-layer buckling, and this rheology has been adopted in recent single-layer buckling studies by Eckert et al. (2014, 2015) and Liu et al. (2016). These numerical simulations have shown the importance of both viscous and elastic contributions to the evolution of stress and strain during the deformation of viscoelastic materials. To the authors' knowledge, Schmalholz et al. (2001) represents the first study to investigate the pressure field within viscoelastic multilayers in the absence of gravity. Their results show increased pressure magnitudes in the hinge regions of the competent layers and increased amount of shear stresses in the incompetent units. A more recent study by Liu et al. (2015) investigates the stress and

strain distribution within a five-layer fold system (i.e. three competent layers) under in-situ effective stress conditions, and it represents the first study of the strain distribution in both competent and less competent layers with viscoelastic rheology. Their results show that the magnitudes and orientations of principal stresses/strains vary significantly for different layers with respect to their relative location in the multilayer stack. As shown for single-layer buckle folds by Eckert et al. (2014) and Liu et al. (2016), a detailed understanding of the principal stresses has important implications for processes such as folding associated fracture initiation. A major conclusion of Liu et al.'s (2015) study is that the stress and strain distributions within multilayer buckle folds seem to be directly dependent on the number of competent layers. One drawback of their study is that only a limited number of layers is tested. The detailed influence of a larger number of layers and varying layer thickness ratios, which significantly affect the shape of multilayer folds (Ramsay and Huber, 1987), remains unclear. In addition to these two parameters, Eckert et al. (2014, 2015) and Liu et al. (2016) have shown that the stress evolution of buckle folds is also dependent on the distribution of other material parameters when in-situ stress conditions are simulated.

The main objective of this study is to provide a comprehensive study investigating and providing a detailed distribution of stress and strain for both competent and less competent layers. 2D plane-strain finite element analysis (FEA) is used to simulate the development of viscoelastic multilayer buckle folds under in-situ stress and pore pressure conditions. Of particular interest is to document the influence of material and model parameters, i.e. Young's modulus contrast, viscosity contrast, number of layers, initial overburden thickness and layer thickness ratio, as their detailed influence on the stress/strain distribution in a multilayer system featuring a large number of layers remains unclear.

2. MODELING APPROACH

2.1. GOVERNING EQUATIONS

In this study, the multilayer folds are simulated using visco-elastic rheology (e.g.Ramsay and Huber 1987; Turcotte and Schubert, 2002; Fowler 2005), and a linear Maxwell model is utilized following the studies of Mancktelow (1999), Zhang et al. (2000), Schmalholz et al. (2001), Eckert et al. (2014, 2015) and Liu et al. (2016). For the multilayer system, it is assumed that folds extend infinitely along the fold axis since many natural folds surfaces can be approximated by the cylindrical fold model (Ramsay and Huber, 1987). A 2-dimensional plane strain finite element analysis approach (via the commercial software package ABAQUS^{TM}) is utilized (Eckert et al., 2014, 2015; Liu et al., 2015) to solve the equations of equilibrium, conservation of mass and constitutive equations. The detailed derivation of the governing equation system is presented by Eckert et al. (2014; i.e. supporting information) and not repeated here.

2.2. MODEL SETUP AND MATERIAL PROPERTIES

Considering that the number of layers in multilayer systems exhibit a strong influence on the amplification rates of the folding layers (e.g. Ramberg, 1961; Mühlhaus et al., 2002; Schmid and Podladchikov, 2006), the number of competent layers (termed as N) is initially set to 10 for a base case model. The model geometry comprises a sequence of 19 layers (i.e. 10 competent layers and 9 less competent layers) of 5m thickness embedded in a less competent matrix with 0.5km initial overburden (Figure 1). The viscosity of the competent layers (μ_l) is 100 times the viscosity of the less competent layers/matrix (μ_m) (Zhang, et al., 1996; Mancktelow, 1999; Zhang et al., 2000; Frehner and Schmalholz, 2006). The multilayer fold system model is setup such that only one wavelength is amplified for each fold. The initial geometry of the folding layers is characterized by small periodic perturbations of the appropriate dominant wavelength (Biot, 1961; Schmid and Podladchikov, 2006) along the shortening direction (x-axis). The initial ratio of amplitude to layer thickness is 0.01 (following Frehner and Schmalholz, 2006). The appropriate dominant wavelengths are selected by the same method presented by Eckert et al. (2014) where the parameter R (after Schmalholz and

Podladchikov, 1999; Schmalholz et al., 2001) is applied to determine if the competent layer is folded viscously (R<1) or elastically (R>1). R is the ratio between the multilayer viscous dominant wavelength, λ_{dv}, and the multilayer elastic dominant wavelength, λ_{de}:

$$R = \frac{\lambda_{dv}}{\lambda_{de}} = \sqrt[3]{\frac{N\mu_l}{6\mu_m}}\sqrt{\frac{P_0}{G}} \qquad (1)$$

where G is the shear modulus and P_0 is the initial layer parallel stress. For the applied viscosity μ_l (i.e. 10^{21}Pa·s) in the numerical models, the initial layer parallel stress is given by $P_0 = 4\mu_l\dot{\varepsilon}$ (Schmalholz and Podladchikov, 1999). For the applied viscosity ratios, R from equation 1 is in the range of 0.252 to 0.400 (for various viscosity contrasts and number of layers investigated) which indicates that viscous folding is the main deformation during buckling. Therefore, the viscous dominant wavelengths of $\lambda_{dv} = 2\pi h \sqrt[3]{\frac{N\mu_l}{6\mu_m}}$ is applied in this study. Moreover, the same thickness of the competent and less competent layer results in a true multilayer-folding mode (Schmid and Podlanchikov, 2006). The model is horizontally compressed under a constant strain rate of 10^{-14} s^{-1} representative of a reasonable geologic deformation rate (Twiss and Moores, 2007) and free slip boundary conditions are applied at the bottom boundary.

Moreover, depth depended porosity and permeability are also applied in the multilayer simulation following Medina et al. (2011):

$$\varphi(z) = 16.39e^{-0.00039z} \qquad (2)$$

$$k(z) = 7.583\cdot10^{-17}e^{0.283\phi} \qquad (3)$$

where ϕ is the porosity (%), z is the depth in m and k is the permeability in m^2. Anisotropic permeability (i.e. the permeability along the X-axis being 5 times of the vertical permeability) is assigned to the model and hydrostatic pore pressure is applied as an initial condition. All material parameters are given in Table 1, unless specified differently for special cases. As described in Eckert and Liu (2014) and Liu et al. (2016) a static pre-stressing step (Figure 1a) is applied to account for gravitational equilibrium before horizontal compression (applying 50% horizontal shortening along the x-direction; Figure 1b) is imposed on the model.

Table 1. Material properties for the base model.

Properties	Folding Layer	Less Competent layer and Matrix
Specific Gravity	2.75	2.75
Viscosity	10^{21} (Pa s)	$2*10^{19}$ (Pa s)
Young's Modulus	$33.7(1-0.1639e^{-0.00039z})$ (GPa)	$3.37(1-0.1639e^{-0.00039z})$ (GPa)
Permeability (at 1000 m)	$1.75\cdot10^{-15}$ (m^2)	$1.75\cdot10^{-15}$ (m^2)
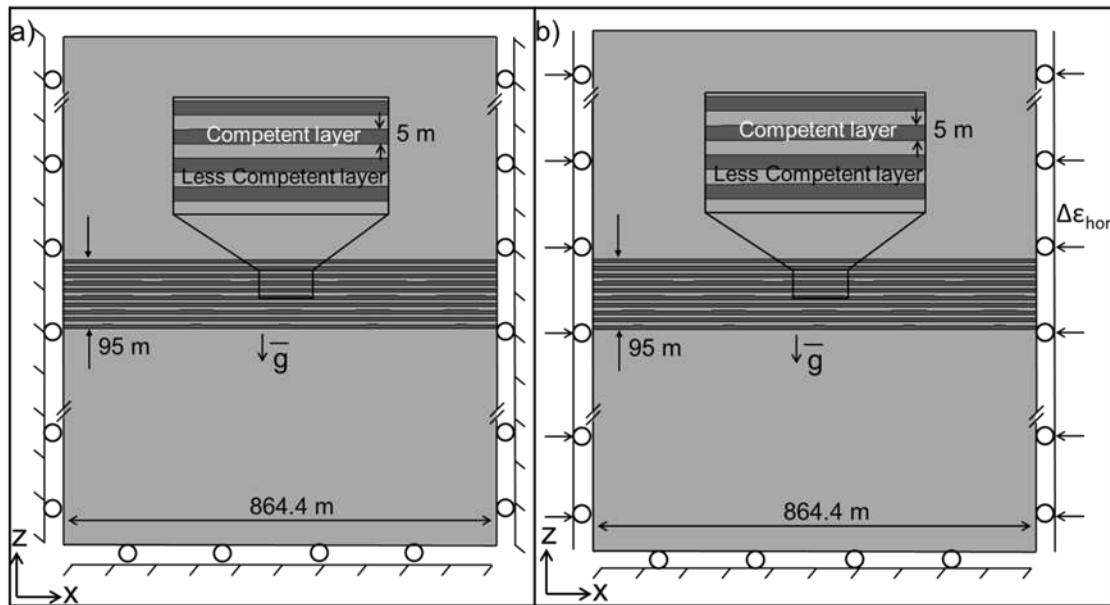
Figure 1. Sketch (not to scale) of the 2D numerical model setup and boundary conditions. A 19-layer multilayer stack is embedded in a matrix with lower viscosity and elastic strength. The thicknesses of the competent and less competent layers (featuring lower viscosity and elastic strength) are 5 m. a) In order to simulate in situ stress magnitudes in a numerical model gravitational pre-stressing is applied. This step utilizes a boundary condition setting where only gravity is acting and the model sides are constrained such that only in-plane displacements are allowed (rollers). b) After reaching gravitational equilibrium a constant tectonic strain ε_{hor} can be added to the model, which results in the initiation of buckling.

2.3. LIMITATIONS

In this study, the same small periodic perturbation of the dominant wavelength is used as the initial geometry for the small-scale folds. In nature, layers composed of different rock types are unlikely to feature perfect periodic perturbations and the shape of the perturbation is influenced by various factors (Frehner and Schmalholz, 2006), for example, sedimentary structures (e.g. wave ripples) or metamorphic processes (e.g. crenulation). Random perturbations of the initial geometry, which are used by Schmalholz and Podladchikov (2001) and Schmalholz and Schmid (2012) may produce comparable results. However, it can be expected that the fundamental deformation of multilayer folds remains the same. Moreover, the focus in this study is on the stress and strain distribution during the deformation of multilayer folds and the influence from various parameters such as number of layers and thickness ratios; therefore, the same periodic perturbation is used to generate comparable symmetric fold shapes (i.e. excluding the impact of random initial perturbation on the stress and strain distribution).

3. RESULTS

In the analysis of the modeling results, the spatial evolution of the minimum effective in-plane principal stress, termed σ'_3, is studied, since it also enables to evaluate the potential of tensile fracture initiation in a 2D analysis (Eckert et al., 2014). To study the strain distribution of the multilayer system, the distribution of the maximum principal strain (ε_1), which represents the long axis of the strain ellipse is investigated here. The following analyses investigate the distribution of σ'_3 and ε_1 of the developed multilayer folds at end of the applied shortening (i.e. 50% shortening). In order to validate that the σ'_3 distribution at 50% shortening represents the possibly lowest overall magnitudes (i.e. tensile stress), the stress evolution of three elements located in the regions featuring tensile stress is plotted in Figure A1 in the Appendix. For all contour plots of effective minimum principal stress (σ'_3) in the results analysis the color scale is adjusted such that white colored contours always represent tensile stress. It needs to be stated here that the following strain analysis does not feature the spatial distribution of the finite strain ellipses (as shown in previous studies: Frehner and Schmalholz, 2006). Due to the large number of layers (and the high resolution finite element mesh) a detailed and clear visualization of strain ellipses is not advisable.

Fold systems form in a variety of geologic environments and a series of parametric studies is performed with the aim of providing a better understanding of which parameters have the greatest influence on the strain and stress distribution within the multilayer system. The parameters considered are elastic modulus contrast, viscosity contrast, overburden thickness, and layer thickness ratio. In each series of analyses, only one parameter is varied. The remaining model parameters of specific gravity, Poison's ratio, Permeability, and strain rate (Table 1) remain constant. Considering the similar distribution of ε_1 for multilayers featuring the same fold shape, the analysis of ε_1 is only performed when significant change of fold shape is observed..

3.1. BASE MODEL

As shown for the base case model (Table 1) with $R_E=10$ (R_E represents the elastic modulus contract between the competent layers and less competent layers), the highest amplitude folds are in the core of the multilayer, and the amplitudes die out towards the

less competent matrix (Figure 2), which is consistent with Kenneth and Johnson (1993). However, different fold shapes are observed here: a) Chevron folds occur in the core of the multilayer system, featuring long straight limbs and narrow hinges and noticeable hinge collapse; b) Concentric folds are observed at the margin of the multilayer stack where one hinge becomes broader and flatter and the adjacent hinge becomes narrower and pinched. Similar fold shapes are also observed by Schmalholz et al. (2001).

The minimum effective principal stress, σ'_3, in the multilayer system shows tensile stress develops at the top of the hinge zones of the antiforms and the bottom of the hinge zones of the synforms for the 3rd and 4th competent layers at the top half and the 7th and 8th competent layers at the bottom half of the 10-competent-layer system (region 1 in Figure 2a). Moreover, tensile stress is also observed at the regions between the limb and the hinge in these layers (region 2 in Figure 2a). The overall magnitude of σ'_3 in the less competent layer is larger than the magnitude in the competent layer and the highest magnitude is found at at the limbs of the less competent layers at the bottom margin of the fold stack (region 2 in Figure 2a). For the ε_1 distribution, low magnitude (<0.003) compressive strain is observed for all competent layers and no extensional strain is observed. The ε1 distribution within the less competent layer shows large magnitudes of compressive strain in the limbs of the less competent layers at the margin (region 1 in Figure 2b). Moreover, high compressive strain is also observed below/above the convex-upward and convex-downward hinge of the outermost competent layers (region 2 in Figure 2a).

To further investigate the distribution of strain, the orientations of ε1 at the end of buckling for competent (white) and less competent layers (green) are shown in Figure 3 for the layers in the core and at the bottom of the multilayer stack. For the layers in the core of the multilayer stack (Figure 3a), ε_1 in the less competent layer is sub-parallel to the shortening direction in the limb and hinge, except for the limb region which experiences the largest amount of limb thinning (red box in Figure 3a). This can be explained by the deformation of the less competent material in this region, which "flows" (due to the large amount of simple shear) from the limb into the hinge zone, which experiences significant thickening, as also observed by Ramsay and Huber (1987). ε_1 in

the competent layer is perpendicular and parallel to the shortening direction at the top and bottom of the convex-upward hinge, respectively, which is also observed by Frehner and Schmalholz (2006). It is also observed that $\varepsilon 1$ in the limb of the competent layer is parallel to the layering at the central layers (region 1 in Figure 3a) and perpendicular to the layering for the other layers. For the layers at the bottom of the multilayer stack (Figure 3b), a similar distribution of $\varepsilon 1$ is observed, except for the lowest competent layer, which features layer-parallel $\varepsilon 1$ throughout the broad and flat hinge zone (region 1 in Figure 3b).
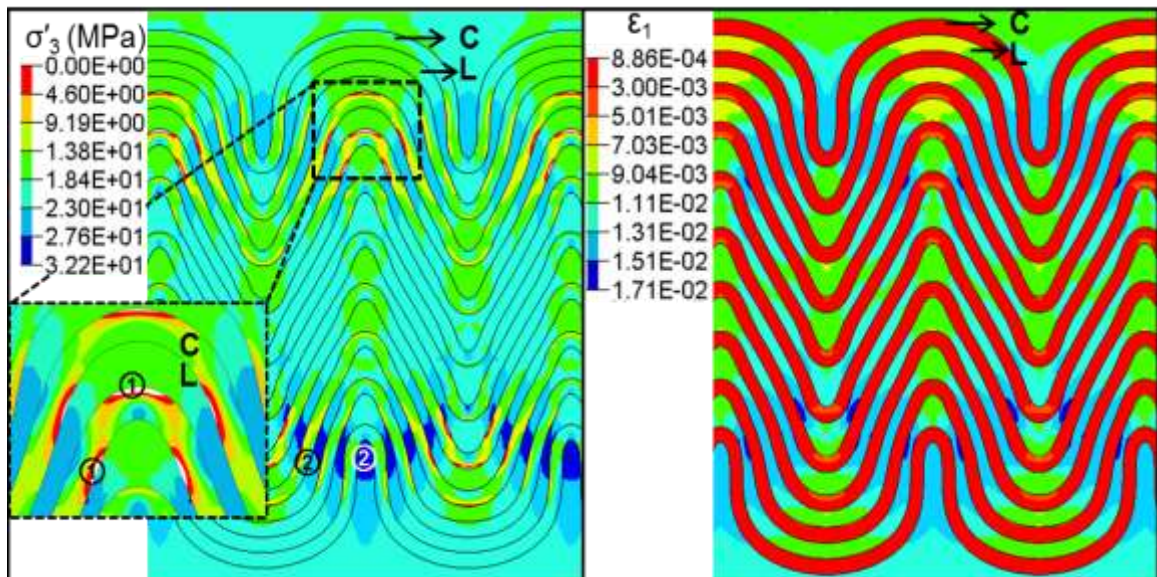
Figure 2. a) Effective minimum principal stress distribution of the multilayer folds for the base case model. The letters C and L in the insets indicate the competent and less competent thin layers, respectively. b) Maximum principal strain distribution of the multilayer folds.

3.2. INFLUENCE OF ELASTIC MODULUS CONTRAST

In order to evaluate the influence of the elastic modulus contrast (i.e. the ratio of Young's Modulus), RE, between the competent layer and the less competent layers, magnitudes of R_E=1, 50 and 100 are applied to the multilayer system. It should be noted that the less competent layers have the same material properties as the less competent matrix. Figure 4 shows the deformed multilayer folds after 50% bulk shortening for R_E=
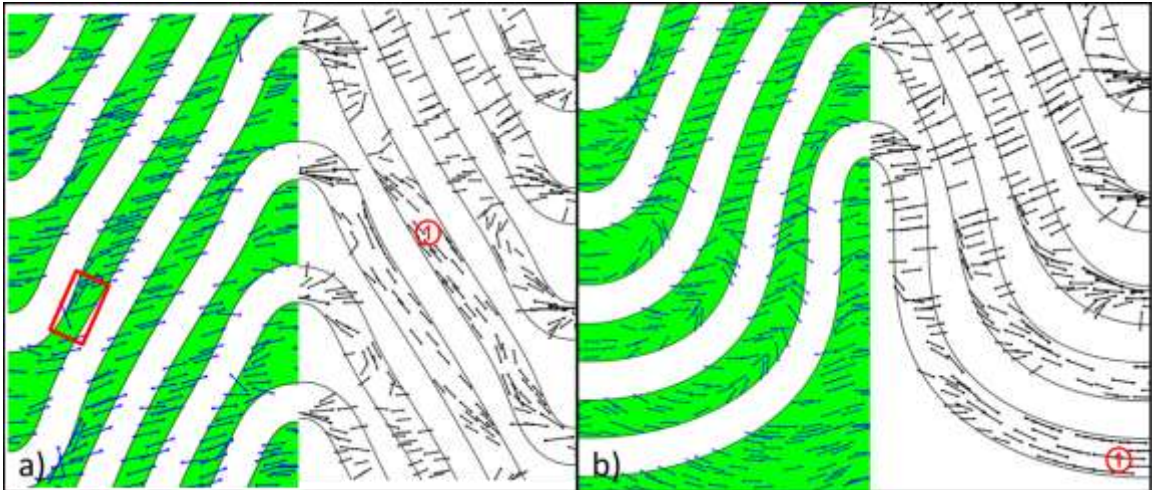
Figure 3. Orientation of the maximum principal strain in the competent and less competent layers in the core (a) and margin (b) of the multilayer stack after 50% shortening.

1, R_E= 50 and R_E= 100. For all models, chevron folds are observed in the core with hinge collapse and concentric folds are observed at the margin of the multilayer stack. For the models with R_E= 1 and R_E= 50 (Figure 3a and 3c), the distribution of the σ'_3 is similar to the base model (in which R_E=10) and tensile stress is observed at the convex-upward hinges and the regions above the limbs for the layers between the core and margin of the multilayer system. For high elastic modulus contrast (i.e. R_E= 100, Figure 3e), tensile stress is developed in more competent layers (i.e. for 6 layers, compared to 4 layers for the base case). With respect to the ε_1 distributions, it is observed that for low R_E (i.e. R_E= 1, Figure 3b), the overall magnitude is much lower than for the base model, and the maximum magnitude of ε_1 is observed at the concave-upward hinge in the competent layer. For higher R_E models (i.e. R_E= 50 and 100, Figure 3d and 3f), the distribution of $\varepsilon1$ is similar to the base model and a larger magnitude of ε_1 is observed in the limb of the less competent layer and below the convex-upward hinge of the lowest competent layer.
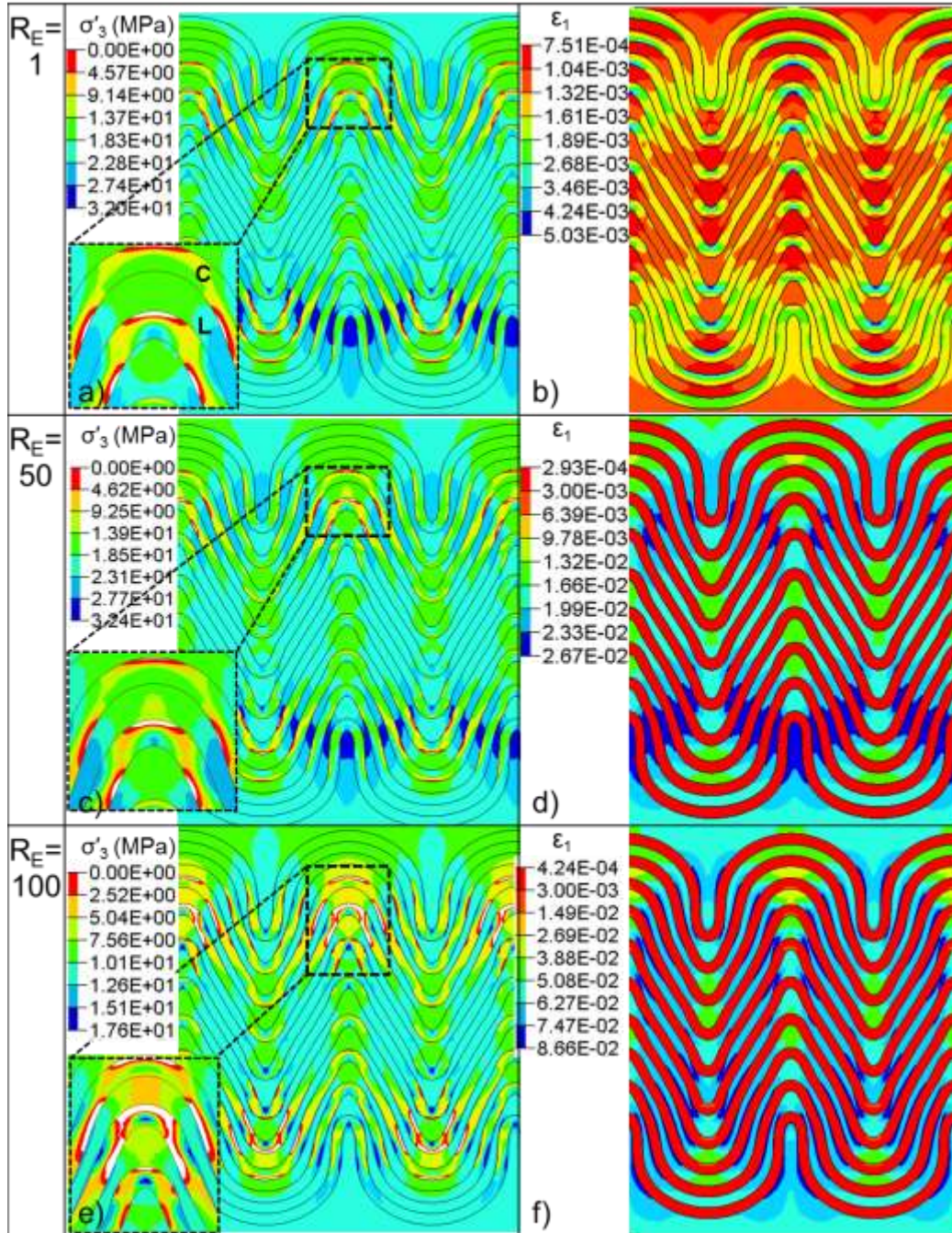
Figure 4. Effective minimum principal stress distribution of the multilayer folds for RE=1(a), RE=50(c) and RE=100(e). The right column shows the maximum principal strain distribution of the multilayer folds for RE=1(b), RE=50(d) and RE=100(f).

3.3. INFLUENCE OF VISCOSITY CONTRAST

In order to evaluate the influence of the viscosity contrast, R_μ, magnitudes of R_μ=10, 50 and 200 are applied to the multilayer system. It needs to be noted that models with a higher R_μ feature a longer dominant wavelength. It is observed that a low viscosity contrast results in sinusoidal fold shapes of all layers with a low amplitude and compressive stress is observed both in the competent and less competent layers, with higher magnitudes of σ'_3 at the hinge of the competent layers and low magnitudes in the limb of the competent layers (Figure 5a). For all models with a larger R_μ, chevron folds are observed in the core and concentric folds are observed at the margin of the multilayer stack (Figure 5c and 5e). The distributions of σ'_3 for these high R_μ models are similar to the base model (in which $R_\mu = 100$). With respect to the resulting ε_1 distributions, it is observed that for low R_μ (i.e. $R_\mu = 10$, Figure 5b), the maximum magnitude of $\varepsilon_1$is observed in the less competent layers and influenced by the depth. For higher R_μ models (i.e. $R_\mu = 50$ and 200, Figure 5d and 5f), the distribution of ε_1 is similar to the base model.

Considering that the model with low R_μ (i.e. $R_\mu = 10$) exhibits a different multilayer fold shape, the orientations of ε_1 are investigated here. The ε_1 in the less competent layer is overall parallel to the shortening direction at the hinge and sub-perpendicular to the layering in the limb region. For the competent layer, ε_1 is parallel to the shortening direction in the limb region and at the bottom of the convex-upward hinge. At the top of the convex-upward hinge, ε_1 becomes sub-vertical. The distribution of ε_1 for the multilayer system is very similar to the 3 layer model by Frehner and Schmalholz (2006). It is important to notice that no rotation of the maximum principles train is observed at the limb of the competent layers. The possible explanation is that due to the low amplitude or low number of competent layer, all the competent layers exhibit same fold shape. The detailed distribution of the maximum principle strain is not included here but can be obtained by reaching the author.
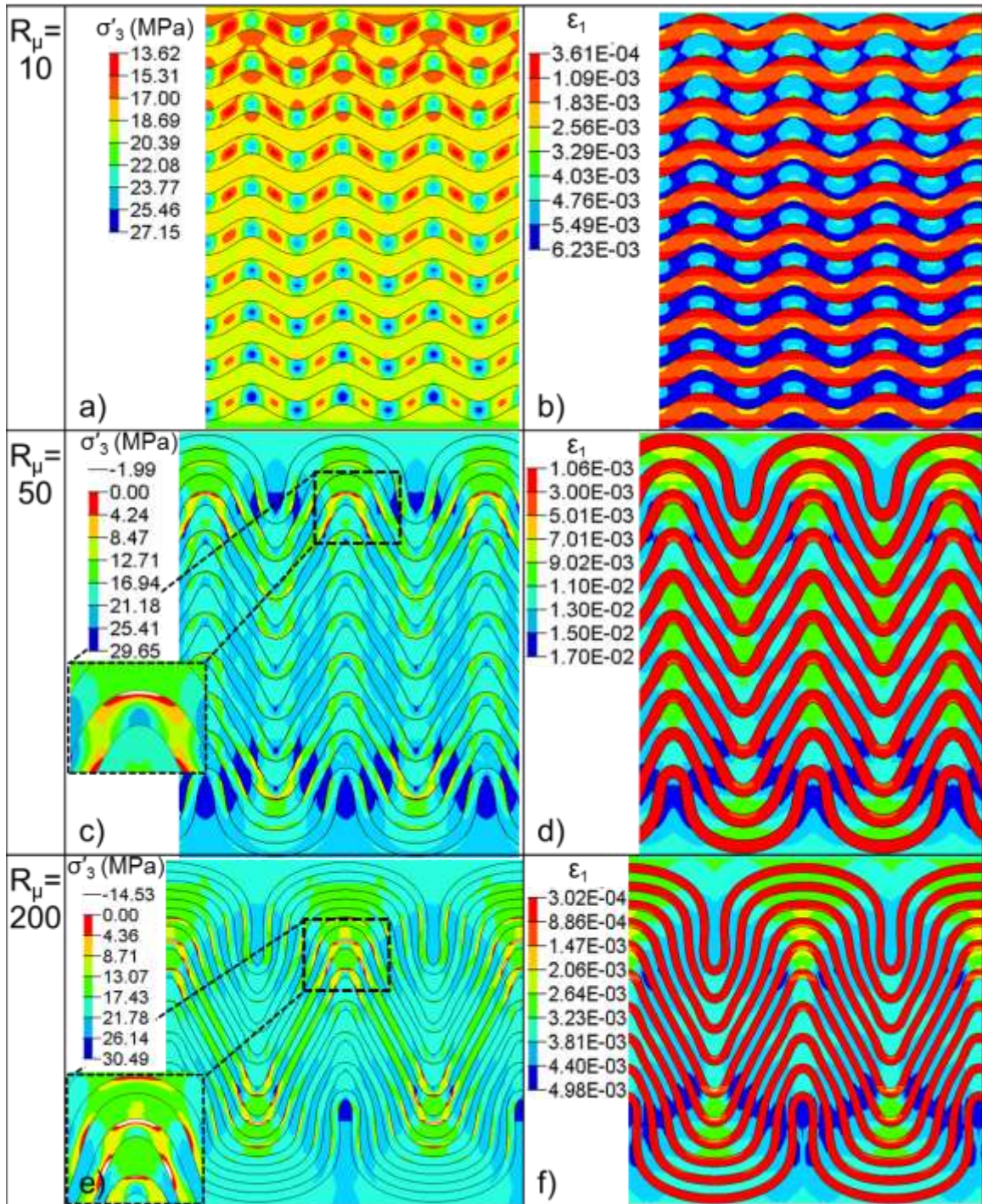
Figure 5. Effective minimum principal stress distribution of the multilayer folds for $R_\mu=10$(a), $R_\mu=50$(c) and $R_\mu=200$(e). The right column shows the maximum principal strain distribution of the multilayer folds for $R_\mu=10$(b), $R_\mu=50$(d) and $R_\mu=200$(f).

3.4. INFLUENCE OF INITIAL OVERBURDEN THICKNESS

In order to evaluate the influence of the thickness of the overburden, three more magnitudes of the initial overburden (200m, 1000m and 2000m) are applied to the multilayer system. Both the overburden depth and the rock density do not remain constant during the development of the fold. As a result of the horizontal compression significant growth of the model domain occurs along the vertical direction and the overburden stress increases. It should be noted that the overburden thickness of the multilayer after 50% shortening is less than two times of the initial overburden due to the compressibility of the model material utilized here. As expected, larger overburden thicknesses results in larger vertical stresses and thus a higher degree of compression both at the crest and the limb of the fold as described by Eckert et al. (2014).

Figure 6 shows the deformed multilayer folds after 50% bulk shortening for initial overburden thicknesses of 200m, 1000m and 2000m. For all models, chevron folds are observed in the core with hinge collapse, and concentric folds are observed at the margin of the multilayer stack. Regarding to the distribution of σ'_3, all models exhibit a pattern similar to the base model. For low overburden, it is observed that a much larger area featuring tensile stress is observed at the convex-upward hinges and the region between the hinge and the limb of the competent layers (Figure 6a). For models with a larger initial overburden, σ'_3 remains compressive and the overall magnitude increases with burial depth (Figure 6c and 6e). Moreover, the distributions of ε_1 of these three models are similar to the base model and the overall magnitude of ε_1 in the less competent layers increases with initial overburden. It is observed that the maximum magnitude of ε_1 is observed at the concave-upward hinge in the competent layer. For models with large overburden (i.e. initial overburden is 2000 m, Figure 6f), the distribution of $\varepsilon1$ is similar to the base model and a larger magnitude of ε_1 is observed in the less competent layer. Even there is no significant difference observed between the model with low and high overburden, the model with large overburden features a much larger magnitude of principle strain than the one with low overburden (maximum magnitude is 0.0131 comparing to 0.00275).
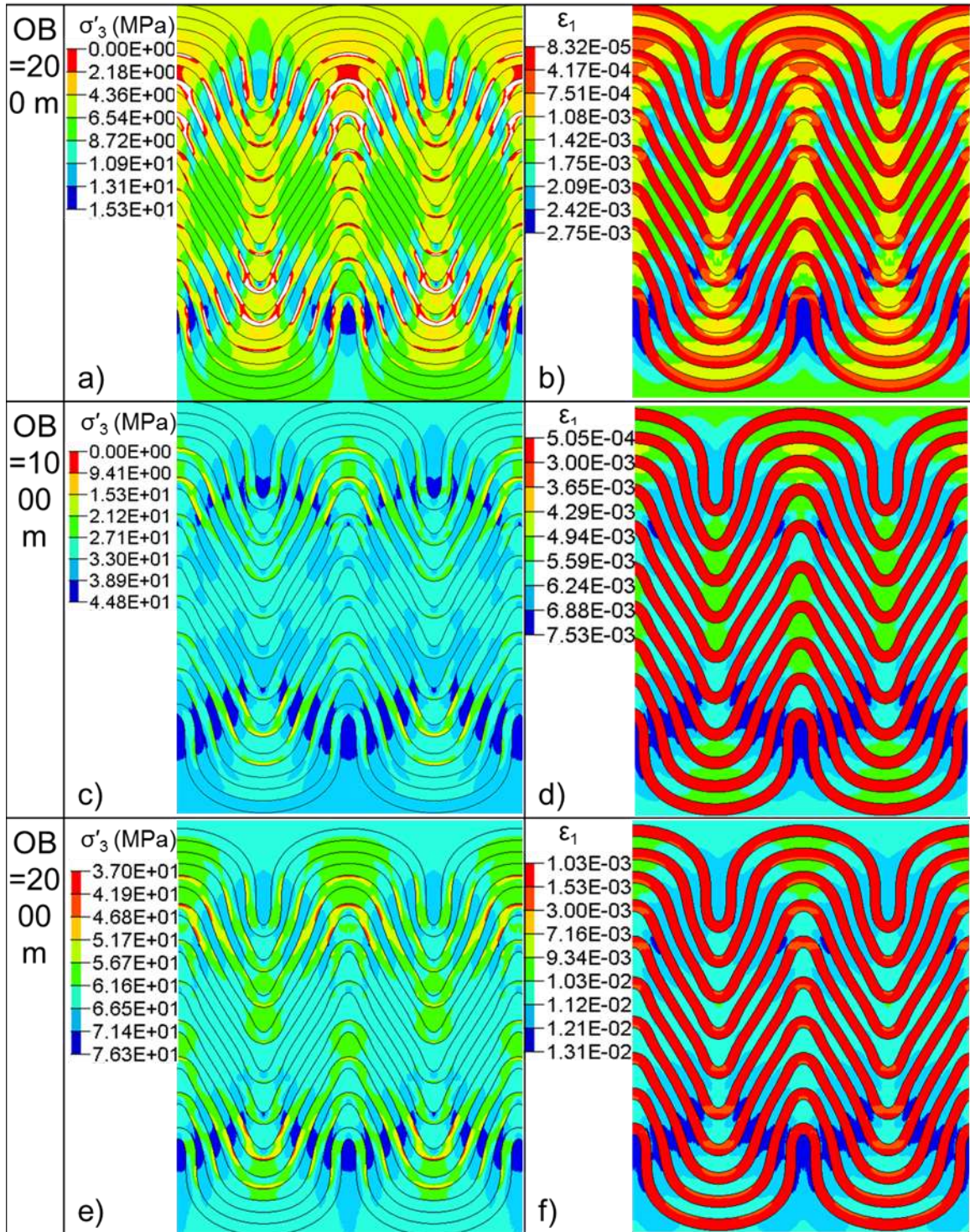
Figure 6. Effective minimum principal stress distribution of the multilayer folds for initial overburden of 200m (a), 1000 m (c) and 2000 m (e). The right column shows the maximum principal strain distribution of the multilayer folds for of 200m (b),1000 m (d) and 2000 m (f).

3.5. INFLUENCE OF THE NUMBER OF LAYERS

In order to evaluate the influence of the number of the competent layers, N, magnitudes of N=5 and 20 are applied to the multilayer system. Considering that smaller magnitudes of N (i.e. N=2 and 3) have been investigated by Liu et al. (2015) for viscoelastic multilayer buckle folds, N=5 is chosen as the minimum magnitude in this study.

Figure 8 shows that for all models, chevron folds are observed in the core, and concentric folds are observed at the margin of the multilayer stack. However, hinge collapse is not observed for the multilayer with N=5. The distribution of the σ'_3 for N=5 is similar to the base model (in which N= 10) and tensile stress is observed at the top of the the convex upward hinge and the regions between the limbs and the hinge for the central layer in the multilayer system (Figure 8a). High magnitudes of σ'_3 are observed in the limb of the less competent layers. For the model with N=20, tensile stress is observed in more competent layers close to the margin of the multilayer stack, and high magnitudes of σ'_3 are observed below the convex-upward hinge of the bottom competent layer and in the limb of the less competent layers at the bottom margin of the multilayer stack. With respect to the resulting ε_1 magnitudes, it is observed that for low N (i.e. N= 5, Figure 8b), the maximum magnitude of ε_1 is observed in the limbs of the central less competent layers. For higher N (i.e. N= 20, Figure 8d), the distribution of ε_1 is similar to the base model and less variations of ε_1 are observed for the layers at the core of the multilayer stack (region 1in Figure 8d).

While the overall distribution of strain magnitude for N=20 is similar to the base case model, a detailed analysis of the strain orientations is presented in the discussion as significant differences comparing to various other model setups are observed.

3.6.INFLUENCE OF THICKNESS RATIO H/S

In order to evaluate the influence of the thickness ratio, H/S (where S represents the thickness of the less competent layer), between the competent layer and less competent layer, five more magnitudes (4, 2, 0.5, 0.33, 0.2) are applied to the multilayer system. It should be pointed out that these magnitudes along with the base model (i.e. H/S=1) represent true multilayer buckle folding after Schmid and Podladchikov (2006).
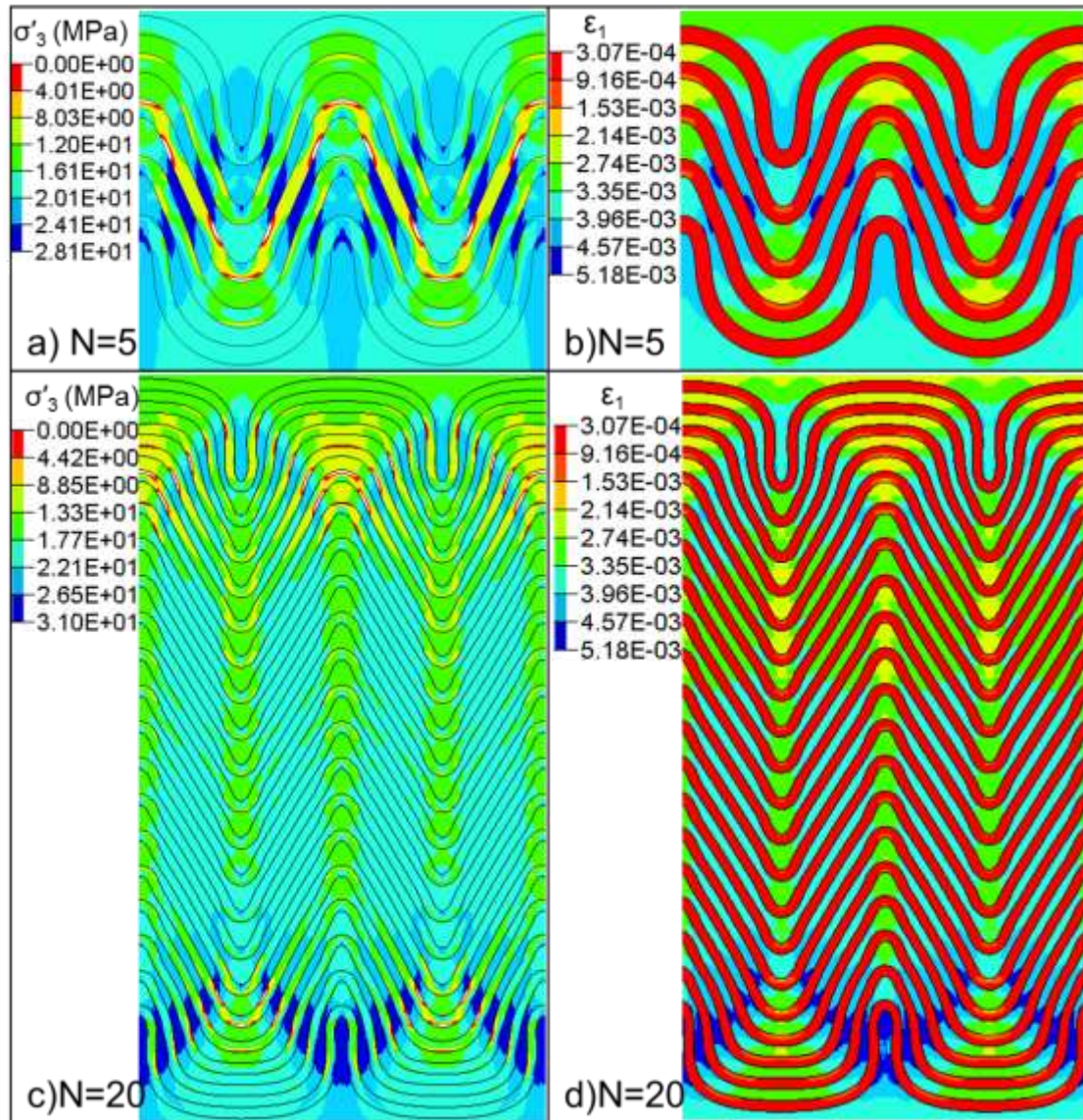
Figure 7. Effective minimum principal stress distribution of the multilayer folds with 5 competent layers (a) and 20 competent layers (c). The right column shows the maximum principal strain distribution of the multilayer folds with 5 competent layers (b) and 20 competent layers (d).

Figure 9 shows the distribution of σ'_3 and ε_1 after 50% bulk shortening for models featuring thin less competent layers (i.e. H/S=4 and 2). While concentric fold is observed at the margin of the multilayer stack, no obvious chevron shape is observed in the core (Figure 9). For the model with thinner less competent layer (i.e. H/S=4, Figure 9a), a larger region of tensile ε_1 is observed at the hinge of both the competent and less competent layers. The distributions of the σ'_3 for H/S=2 is similar to the base model

(Figure 9c). With respect to the resulting ε_1 distributions, it is observed that for H/S=4 (Figure 9b), extensional ε_1 is observed at the hinge of the less competent layer where the space between competent layers increases due to the development of chevron fold fold. For the model with H/S=2 (Figure 9d), the distribution of ε_1 is similar to the base model and a larger magnitude of ε_1 is observed below the hinge of the bottom competent layer and at the limb of the less competent layer locating at the bottom margin of the multilayer stack.

Figure 10 shows the distribution of σ'_3 and ε_1 after 50% bulk shortening for models featuring thin thick competent layers (i.e. H/S=0.5, 0.33 and 0.2). For the model featuring H/S=0.5, chevron fold is observed in the core and concentric fold is observed at the margin of the multilayer stack (Figure 10a and 10d). Low magnitude of compressive σ'_3 is observed at the hinge and the region between hinge and limb on some competent layers and no tensile stress is observed (Figure 10a). The resulting ε_1 distribution shows high compressive strain at the limb of the bottom less competent layers and the regions below the convex-upward hinge of the bottom layer (Figure 10d). The distributions of σ'_3 and ε_1 are similar to previous model and no tensile stress is observed for the model with H/S=0.33 (Figure 10b and 10e). The competent layers exhibits same sinusoid fold shape for the model with H/S=0.2 and the σ'_3 distribution in the competent layers showing low and high magnitude of compressive stress at top and bottom of the convex-upward hinge, respectively (Figure 10c) . Regarding to the stress in the less competent layer, the σ'_3 distribution exhibits a strong relation with depth and the magnitude of σ'_3 increases with depth. The ε_1 for this model shows low compressive strain in the competent layer and depth related distribution in the less competent layers where ε_1 increases with depth (Figure 10f).

Since the model with low H/S (i.e. H/S=0.2) exhibits a different multilayer fold shape, the orientations of ε_1 at the end of buckle shortening for competent (white) and less competent layers (green) are shown in Figure 11. The ε_1 in the less competent layer is overall horizontal and parallel to the shortening direction. For the competent layer, ε_1 is parallel to the shortening direction in the limb region and at the bottom of the convex-upward hinge. At the top of the convex-upward hinge, ε_1 becomes sub-vertical. The

distribution of ε_1 for the multilayer system with H/S=0.2 is very similar to the single layer buckle folds (Eckert et al.,2014).
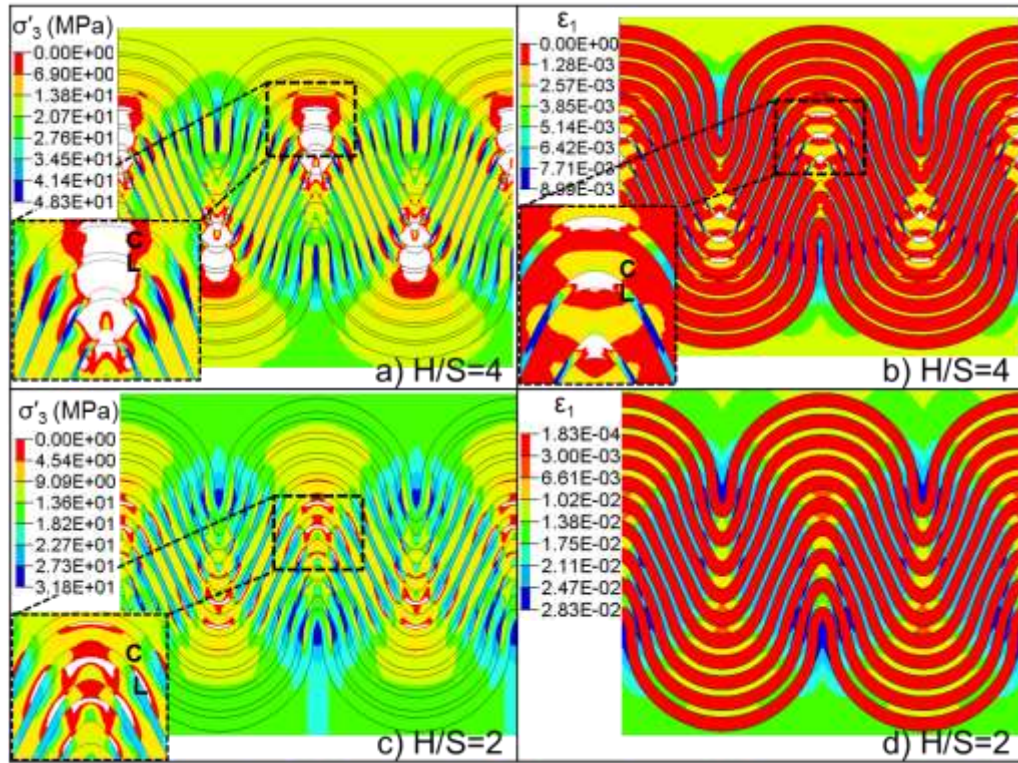
Figure 8. Effective minimum principal stress distribution of the multilayer folds with H/S=4 (a) and H/S=2 (c). The right column shows the maximum principal strain distribution of the multilayer folds with H/S=4 (b) and H/S=2 (d).
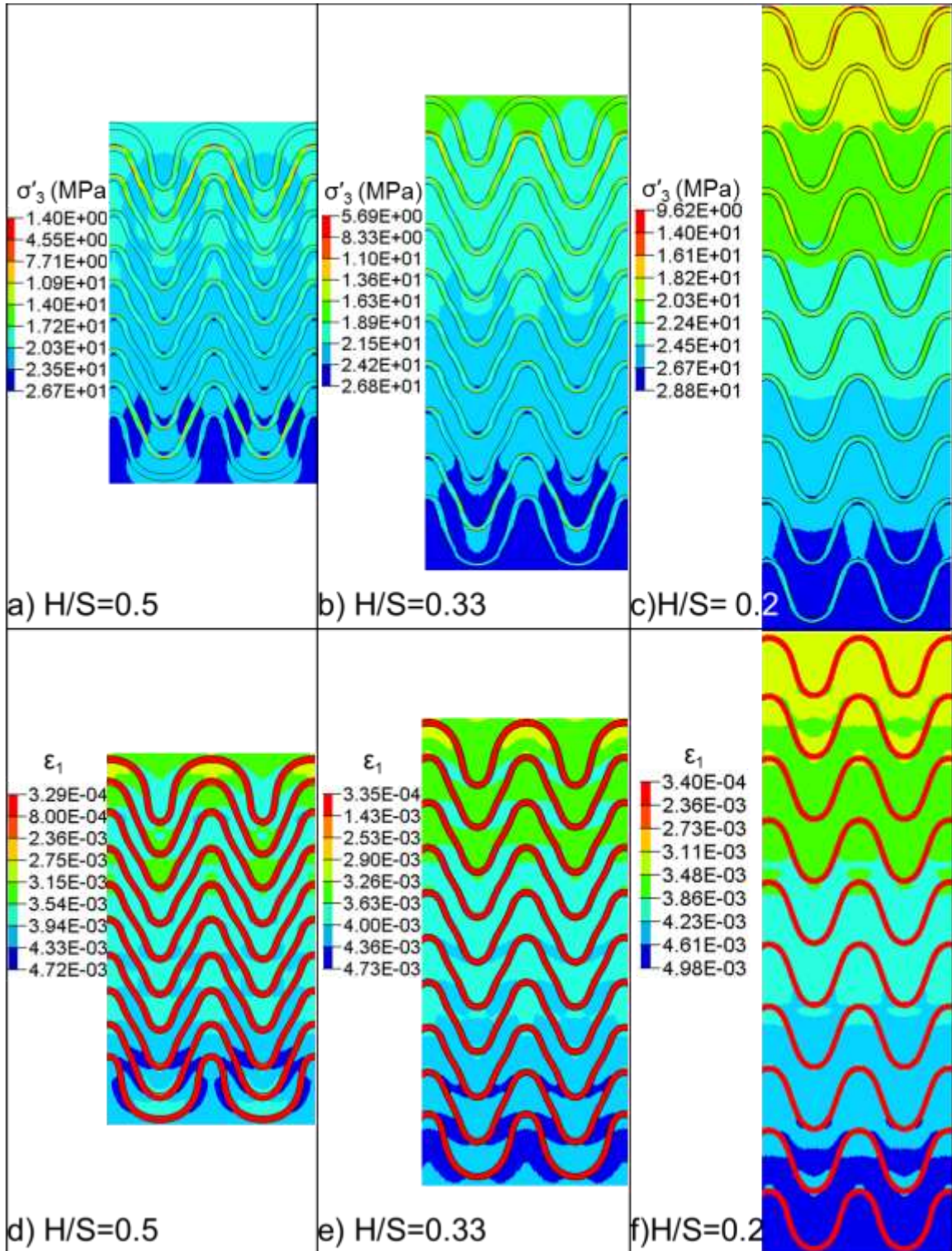
Figure 9. Effective minimum principal stress distribution of the multilayer folds with H/S=0.5 (a), H/S=0.33 (b) and H/S=0.2 (c). The bottom row shows the maximum principal strain distribution of the multilayer folds with H/S=0.5 (d), H/S=0.33 (e) and H/S=0.2 (f).
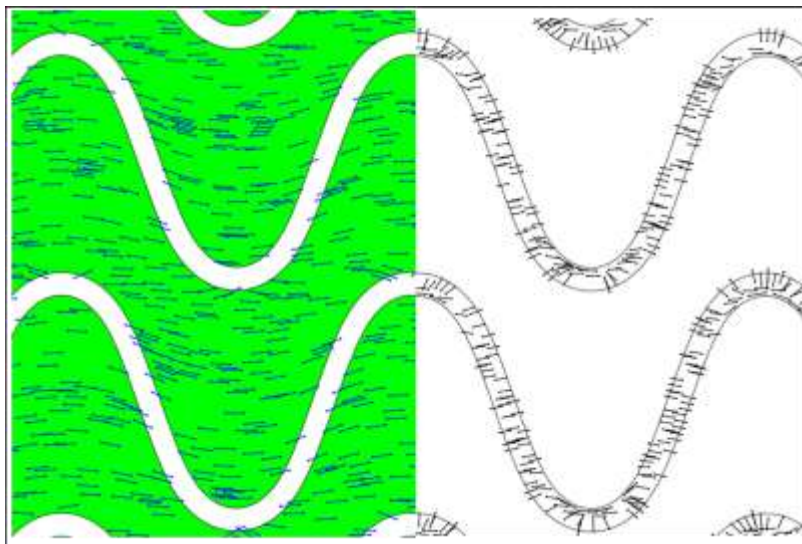
Figure 10. Orientation of the maximum principal strain in the competent and the less competent layers in the multilayer stack after 50% shortening with H/S=0.2.

4. DISCUSSION

4.1. SUMMARY

The 2-D plane strain modeling approach presented in this study shows that the deformation of visco-elastic multilayer folds can be successfully simulated and helps to provide a better understanding of multilayer fold development and the associated stress and strain distribution in both the competent and less competent material. A large variety of studies investigate the deformation of multilayer folding for various rheologies, such as elastic materials (e.g. Johnson, 1977) and viscous materials (e.g. Ramsay and Huber, 1987; Mazzoli and Caremolla, 1992; Frehner and Schmalholz, 2006; Schmid and Podladchikov, 2006; Lechmann et al., 2010) and visco-elastic materials (Schmalholz et al., 2001). An important drawback of these studies, as stated by Smart et al. (2009), is the neglect of gravity and pore pressure which prevents the analysis of in-situ stress/strain magnitudes and their distribution. As stated by Eckert et al. (2014), the in-situ state of stress is compressive and tensile buckling stresses need to be very large to overcome the compressional state of stress due to the weight of the overburden. Moreover, unlike the growth rate of multilayer fold systems, which has been thoroughly studied along with the influence of number of layers and the thickness ratio between the competent and less competent layers (Schmid and Podladchikov, 2006), the distribution of stress and strain in the multilayer system and their relation to various system parameters remains unclear. This study utilizes a modeling approach, which simulates the buckling process under realistic in-situ stress and strain conditions and the sensitivity analysis of the tested model parameters (elastic modulus contrast, viscosity contrast, overburden, number of layers and thickness ratio) shows that the both the fold shape and the distributions of stress and strain in both the competent and less competent material are depended on the model parameters.

It is commonly observed that folds in tightly stacked multilayers exhibit a large variety of shapes including chevrons, angular folds with straight limbs and sharp hinges (Schmid and Podladchikov, 2006). The results presented confirm the basic observations regarding the development of multilayer folds with individual layers featuring a more concentric fold shape at the margin of the sequence and a more chevron fold shape in the

center of the sequence, as predicted by Schmalholz et al. (2001). However, this study represents for a more complex model setup (i.e. simulating in-situ effective stress conditions) which results in some significant differences. Schmalholz et al. (2001) observe that only the marginal layers show a concentric shape, whereas all other layers show a strong chevron shape for large amplitudes. However, the base model of this study (featuring the same number of competent layers, i.e. N=10) shows an obvious concentric fold shape at the margin of the sequence and a transition to the chevron fold shape in the center of the sequence, which is more similar to the multilayer system featuring a larger initial wavelength in Schmalholz et al.'s (2001) study. The different fold geometries for visco-elastic multilayers, when the dominant wavelength is applied, can be explained by the different type of folding. In Schmalholz et al.'s (2001) study elastic folding is the dominant deformation mechanism, as R=2. Here, the magnitude of R is smaller than 1 and the dominant deformation mechanism is viscous folding. Moreover, gravity and pore pressure are not included in Schmalholz et al. (2001) study. Furthermore, the results presented show that low viscosity contrasts or thick less competent layer result in fold shapes where all competent layers exhibit the same fold shape with large inter-limb angles and chevron shapes are not observed. The influence of thickness ratio observed here is in agreement with Ramsay and Huber (1987), who show that the decrease of the thickness of the less competent layer results in chevron folds. Additionally, this study also shows that low viscosity and the resulting low amplification of the competent layers inhibit the development of chevron folds.

The results of the effective minimum principal stress presented show that tensile stress develops at certain regions, including the top of the convex-upward hinge and the region between the convex-upward hinge and the limb (Figure 3). The tensile stress at the top of the convex-upward hinge which results from the buckling of the competent layer is also observed for single-layer folding (Eckert et al., 2014). The orientation of the tensile stress observed at the region between the convex-upward hinge and the limb is observed to be layer-parallel (Figure 3), indicating that the tensile stress results from the increased thickness of the hinge of the less competent layer below. Similar observations can be found for a multilayer system with fewer layers (i.e. 3-competent-layer system, Liu et al.,2015) and a multilayer system in elastic mode (i.e. R=2, Schmalholz et al., 2001).

Compared to the single layer folding in which the development of tensile stress requires either low overburden pressures or high viscosities (Eckert et al., 2014), tensile stress in the multilayer system can be developed for more conditions, except for low viscosity ratio or high overburden or thick less competent layers. For the latter condition, the folding deformation of the multilayer system is more close to single-layer folding even though the multilayer remains in "true multilayer" mode (Schmid and Podladchikov, 2006). The findings presented here indicate that the ratio of the thickness of the competent layers to the less competent layer, H/S, has a significant influence on the distribution of stress and strain even when the multilayer system remains in a true multilayer system. It is observed that when H/S decreases from 1 to 0.25, there is a transition from "true multilayer" behavior to "real single layer" behavior, where the layers fold independently and the strain distribution in the less competent layer shows a significant dependence on depth (Fig. 10). The influence of H/S on the stress and strain distribution investigated here confirm Ramberg's (1960,1961) findings , who states that the key to determining whether the system behaves as a true multilayer or as independent single layers is the spacing between competent layers. Moreover, the results presented also show that low viscosity and the resulting low amplification of the competent layers will contribute to the "real single layer" behavior of a multilayer system (Figure 5).

Frehner and Schmalholz (2006) show the detailed distribution of principal strains in a multilayer system featuring 2 competent layers and one less competent layer and the maximum principal strain is observed to be vertical at the hinge region and parallel to the layering in the limb of the less competent layer. However, the modelling results presented show that for multilayer systems with a large number (i.e. N=10) of layers the strain distribution is more complex and the strain distribution varies not only for different locations within one layer but also for the relative location of the layers within the multilayer system. Thus, the strain distribution for a simple multilayer setup with two competent layers (e.g. Frehner and Schmalholz, 2006) cannot be applied to a multilayer system with a large number of layers.

With respect to the orientation of the maximum principal strain, the overall ε_1 orientation in the less competent layer is parallel to the shortening direction except for the region featuring hinge collapse, where ε_1 rotates to parallel to the layering direction. For

the competent layers, the distribution of ε_1 at the hinge region is close to single-layer folds except for the margin layers. For the limb of the competent layers, the distribution of ε_1 shows a large variation for models with various numbers of layers. Figure 11 shows the orientation of ε_1 for (some of) the competent layers. It is observed that when the number of layer is low (i.e. N<10), ε_1 is sub-parallel to the shortening direction for all the three competent layers in the core of the multilayer system. For multilayers with N=10, layer-parallel ε_1 is observed at the 5th and 6th competent layer and for multilayers with N=20, layer-parallel ε_1 is observed at the 7th, 8th, 13th, 14th (13th and 14th are not shown in Figure 11) competent layer. It is also observed that ε_1 rotates back to the layer-perpendicular direction for the core layers in the multilayer with N=20. For the broader and flatter hinge of the margin competent layer, ε_1 is parallel to layering throughout the entire hinge (Figure 3). Moreover, when the shape of the multilayer system deforms more closely compared to single-layer folding (e.g. low viscosity contrast or thick less competent layers), the strain distributions in the competent layers is similar to single-layer folding (i.e. Figure 6 and 11).
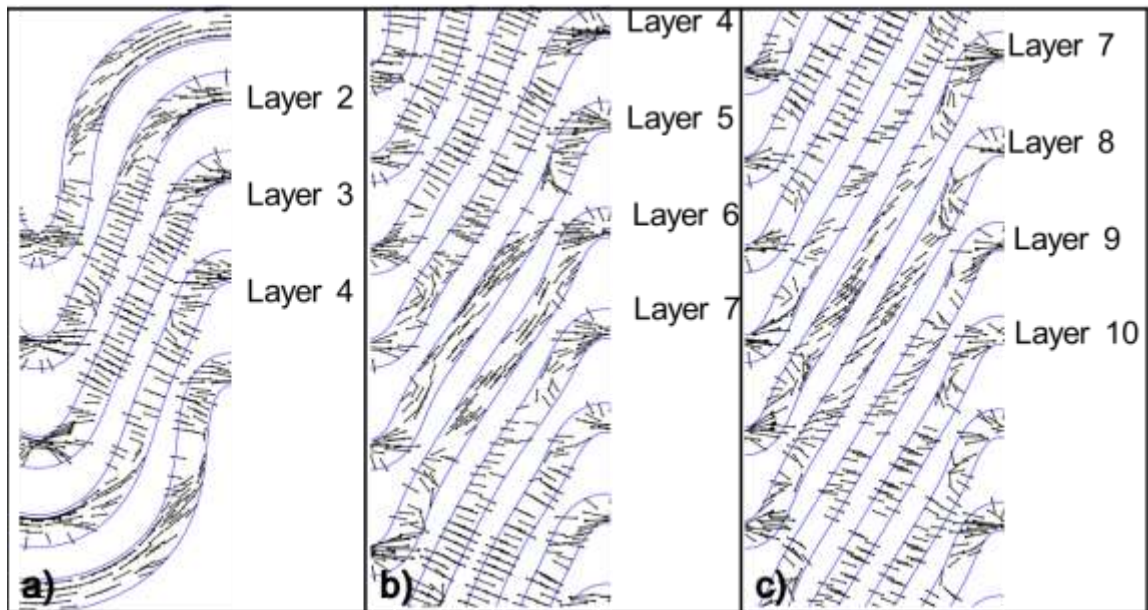
Figure 11. Orientation of the maximum principal strain in the competent layers for N=5, 10 and 20.

Clearly, there are other parameters of the multilayer folds that may influence the buckling of multilayer such as initial geometry (Schmalholz and Schmid, 2012) and heterogeneous materials (Schmalholz et al., 2001). A detailed investigation on the influence of these parameters on the multilayer folding is beyond the scope of the paper but is vary tractable using the numerical simulation presented.

4.2. SHAPE OF FOLDS

In the simulations presented, the multilayer folds exhibit a large variability in fold shapes, including chevron shape, concentric shape and regular sinusoidal shape. For the chevron shape observed in the models presented, it is interesting to notice that neither anisotropic material properties (Bayly, 1970; Cobbold et al., 1971; Price and Cosgrove, 1990) nor flexural slip (e.g. Ramsay, 1974, Dubey and Cobbold, 1977, Behzadi and Dubey, 1980; Hudleston et al., 1996) or intersection of kink bands (Paterson and Weiss, 1966; Cobbold et al., 1971) has contributed to the development of these chevron folds. Hinge collapse is also observed along with the chevron folds (e.g. Figure 2). In order to compare the shape of the central layer in the multilayer folds at different stages of shortening with various magnitudes of system parameters, the evolution of the angle of the limb dip with shortening is plotted in Figure 12. The relationship between the shortening and limb dip for three ideal fold shapes, circular, sinusoidal and chevron, are also plotted here (Treagus, 1997). Five models are included in Figure 12. For the base model (red), the shape of the central competent layer is between the sinusoidal and chevron shape at early stages (i.e. ≤30% shortening) and deforms into chevron folds after 40% shortening. When high viscosity contrast is applied (i.e., $R\mu=200$, green), the fold shape for the central layer remains sinusoidal until 35% shortening and deforms into chevron folds at 50% shortening. For the model with a large number of competent layers (i.e. N=20, purple), chevron shape is observed at early stages of shortening (15%) and the sinusoidal shape is not observed. For thin less competent layers (i.e. H/S=4, brown), the fold shape remains sinusoidal and chevron shape is not observed. When the less competent layers become thick (i.e. H/S=0.25, blue), the shape of the fold deforms into sinusoidal shape. It can be concluded that the different parameters have influence on the shape of the multilayer folds with a various degree. As Hudleston and Treagus (2010)

point out, the various shapes in multilayer fold systems suggest that shape may potentially represent much more information on mechanical properties than has so far been achieved. However, the facts that folds of a given shape can be deformed by different processes and multiple multilayer systems may develop due to varying thickness and rheological properties make the relation between fold shape and system properties more complicated. A more detailed investigation on the influence of various parameters on fold shape is therefore considered beyond the scope of this paper.
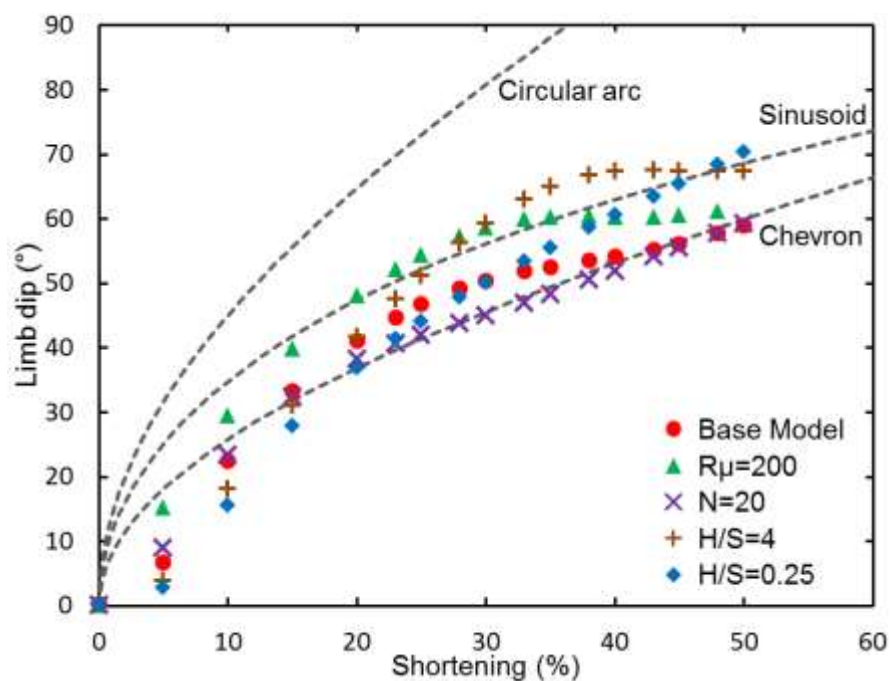
Figure 12. The evolution of limb dip with shortening for various models tested. The dashed lines represent the evolutions for circular arc, sinusoid and chevron shape, respectively (after Treagus, 1997).

4.3. DISTRIBUTION OF POTENTIAL TENSILE FRACTURES

As shown by Eckert et al (2014) and Liu et al. (2016) the distribution of tensile stresses in a fold system has important implications with respect to the initiation of tensile fractures. We compare the location of tensile stress magnitudes with their respective orientations to pinpoint the distribution of tensile fracture for the base model and the model with H/S=4 featuring the largest region of tensile stress. Figure 13 shows the spatial extent and orientation of tensile stress at the end of shortening, in addition with the

orientation of likely tensile fractures. For the base model (Figure 13a), tensile fractures (normal to bedding and parallel to fold axis) are likely to be initiated at the top of the hinge zones of the competent layer 3 and 4, which is similar to the findings of Eckert et al. (2014). It needs to be pointed out that even though low permeability is critical for tensile fractures to be initiated at the top of the hinge for single-layer folds (Eckert et al. 2014), the permeability in the base model is much higher and hydrostatic pore pressure develops during shortening. Moreover, tensile fractures normal to the layering are also likely to be initiated at the region between the hinge and the limb (Figure 13a). Compared to a multilayer system with less competent layers where overpressure (due to low permeability) is required to initiate tensile fracture in the same region (Liu et al.,2015), the results presented here indicate that tensile fractures can develop without overpressure and low permeability.

The distribution of tensile σ'_3 magnitudes and tensile fractures for the model with thin less competent layers (i.e. H/S=4, Figure 13b) shows that more tensile fractures are initiated at the hinge regions, both in the competent and less competent layers with various orientations. It is important to notice that tensile stress is developed throughout both the competent and less competent layer at the hinge region, including the bottom of the hinge featuring compressive strain. Horizontal tensile fractures are observed at the hinge of both the competent and the less competent layers. Near the hinge zone tensile fractures become sub-horizontal in the competent layer. Tensile fractures which are normal to bedding and parallel to fold axis are only observed at the top of the hinge in competent layer 6. The tensile σ'_3 orientations, which show an overall parallel trend with respect to the fold axis in the hinge zone indicate that the hinges in the core of the multilayer with thin less competent layers are under significant horizontal compression. This observation may explain commonly observed tensile fractures perpendicular to the fold axis (e.g. Price and Cosgrove, 1990; Jager et al., 2008). It should be pointed out that these bedding parallel tensile fractures, i.e. bedding-parallel fibrous veins, also termed as "Beef" (Cobbold, 2013) can also be attributed to fluid overpressure in combination with horizontal compression during single-layer buckling (Eckert et al., 2014; Liu et al., 2016). Moreover, tensile fractures perpendicular to bedding are also observed at the region between the limb and the hinge in this model (Figure 13b).
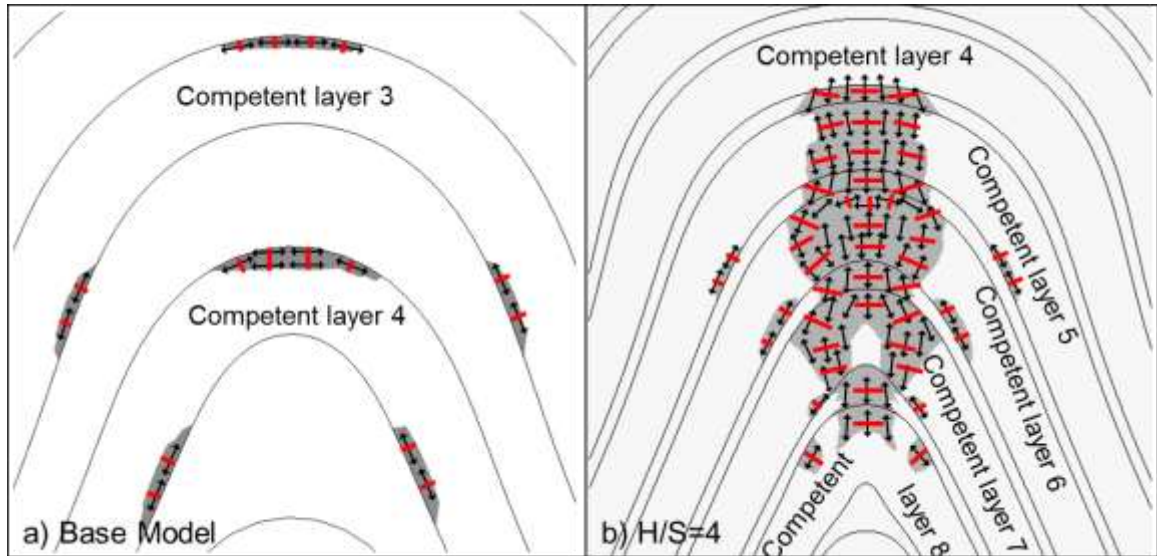
Figure 13. a) Orientation of tensile failure (red lines) perpendicular to bedding for the base model after 50% shortening. The black lines represent the orientations of σ'_3. The light gray contours show the spatial extent of tensile stress magnitudes. b) Orientation of tensile failure (red lines) perpendicular to bedding for the model with H/S=4 after 50% shortening. The black lines represent the orientations of σ'_3. The light gray contours show the spatial extent of tensile stress magnitudes.

4.4. MULTILAYER MODEL WITH VARIOUS LAYER THICKNESS

Considering that natural multilayer fold stacks are more complex having various thicknesses of competent and less competent layers, a multilayer system characterized by a heterogeneous thickness of both competent layers and less competent layer is investigated here. The number of competent layers, N, is 30 (i.e. resulting in a 59 layer stack, see Figure 14) with random H/S distributions within the range of 0.1-10. The thickness of the competent layer ranges from 1<H<5m, and from 1<S<20m for the less competent layer. It needs to be noted that the initial wavelength is depended on the thickness of the competent layer as single-layer and thus only one wavelength is amplified. The initial amplitude of these perturbations for all layers is set to be 0.01 of the layer thickness. The rest of the model setup and material properties are the same as for the base model (Figure 14).
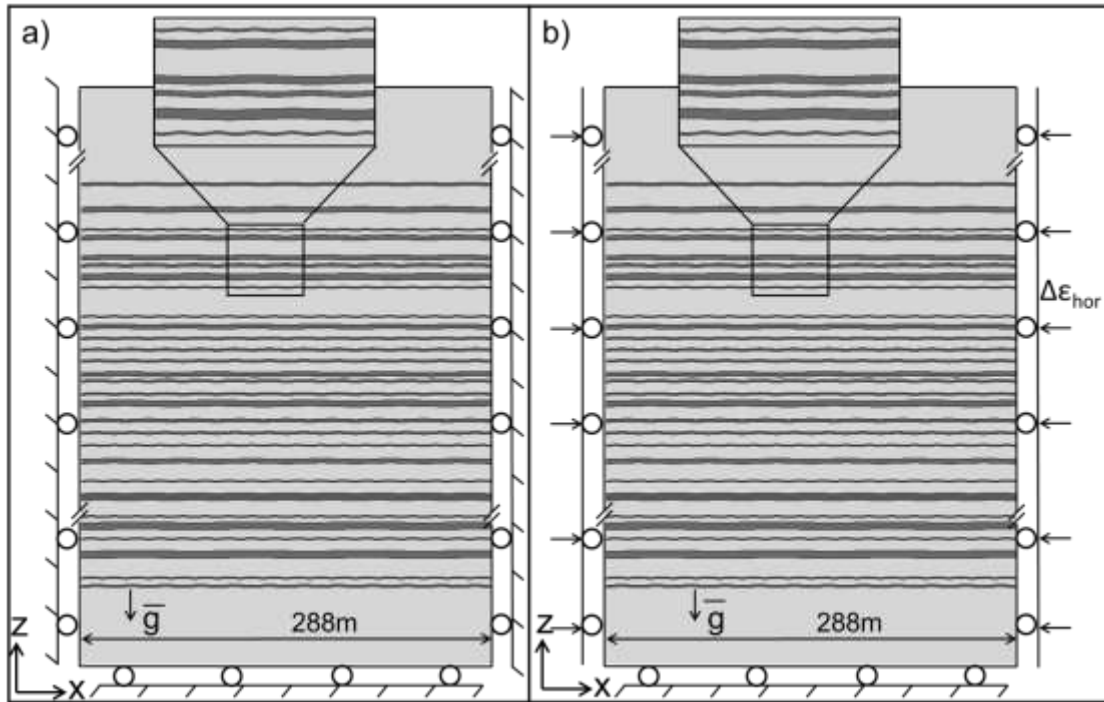
Figure 14. Sketch (not to scale) of the 2D numerical model setup and boundary condition. A 59-layer multilayer is embedded in a matrix with lower viscosity and elastic strength. The thicknesses of the competent and less competent layers vary. a) In order to simulate realistic stress magnitudes in a numerical model gravitational pre-stressing is applied. This step utilizes a boundary condition setting where only gravity is acting and the model sides are constrained such that only in-plane displacements are allowed (rollers). b) After reaching gravitational equilibrium a constant tectonic strain ε_{hor} can be added to the model, which results in the initiation of buckling.

After 20% shortening, the amplitude and limb dips of the thinner layers are larger than those of the thicker layers because the initial ratio of amplitude to thickness is larger in the in the thicker layers. This indicates that thin folding layers develop and grow more quickly than thick folding layers (Frehner and Schmalholz, 2006). In particular, the thin layers fold having more angular hinges. Moreover, the folding of the thin competent layers which are close to a thick competent layer shows a significant dependence on the adjacent thick layer and polyharmonic folds are generated. After 50% shortening, the overall fold shapes are considerably irregular (Figure 15b). The thin layers develop larger wavelength folds as a consequence of the influence of folding of the thicker layers. It is observed that the orientation of fold axial planes varies significantly and shapes of some folding layers are strongly asymmetric. These finds are in agreement with previous

studies on different scales of fold (e.g. Ramsay and Huber, 1987; Treagus and Fletcher, 2009; Schmalholz and Schmid 2012). Moreover, unfolding is observed on the thin competent layer embedded with two competent thick layers compared to earlier stages (e.g. layer A in Figure 15) which is results from the compression of the adjacent thick competent layers. Similar findings are also observed in Frehner and Schmalholz's (2006) study on the deformation of parasitic folding.
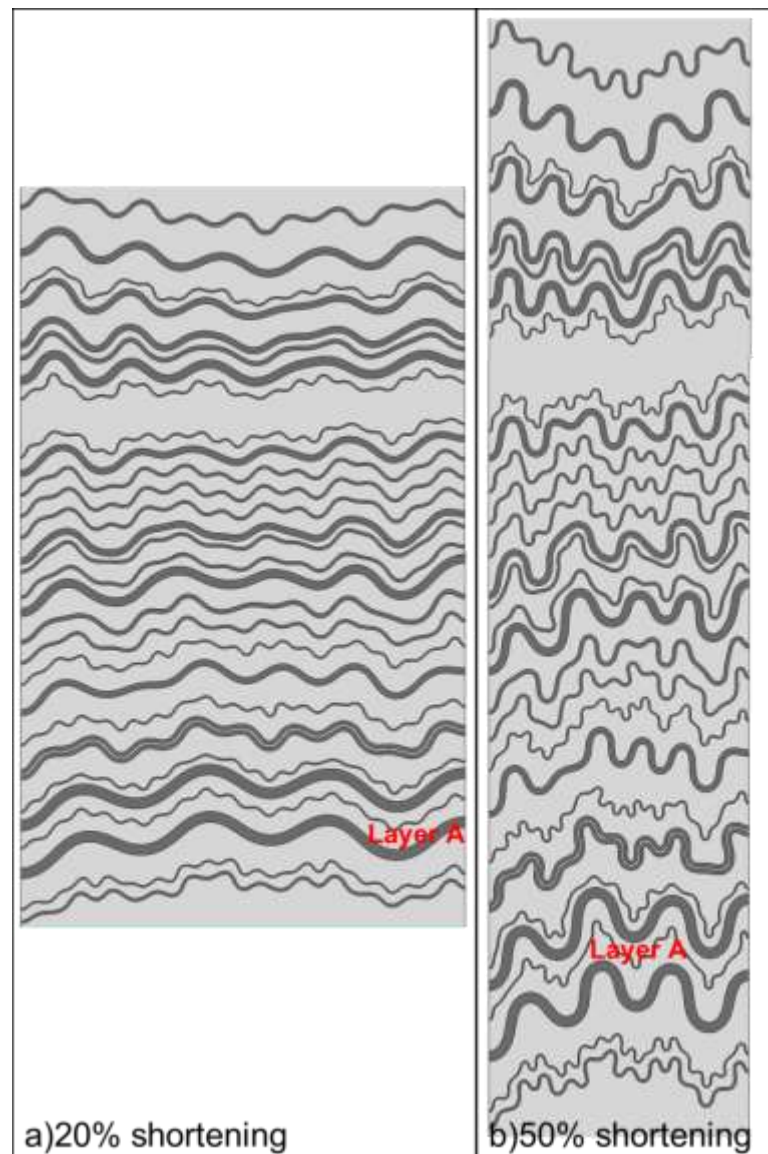
Figure 15. Fold shape of the multilayer model with various thicknesses after 20% shortening (a) and 50% shortening (b).

Figure 16 shows the σ'_3 distribution of the multilayer folds after 50% shortening. It is observed that the complex deformation of this multilayer system result in not only irregular fold shapes but also unsymmetrical stress distribution. Tensile stress (white color) is observed both in the thin and thick competent layers. As shown in the upper inset in Figure 16, tensile stress is observed at top of the convex-upward hinge and the region between the hinge and the limb of the thick competent layer. For the thin layer tensile stress is observed at multiple locations. Large magnitudes of compressive σ'_3 is mainly observed in the bottom layers, both in the competent and less competent material. It needs to be pointed out that no general description can be provided due to the complex distribution. Figure 16 illustrates that the complex process of multilayer folding and the progressive change from initially symmetric to asymmetric, irregular shapes and associated stress distribution. This represents an interesting observation and further investigations on multilayer folds with heterogeneous distribution of competent and less competent layers are necessary, which are beyond the scope of this contribution.
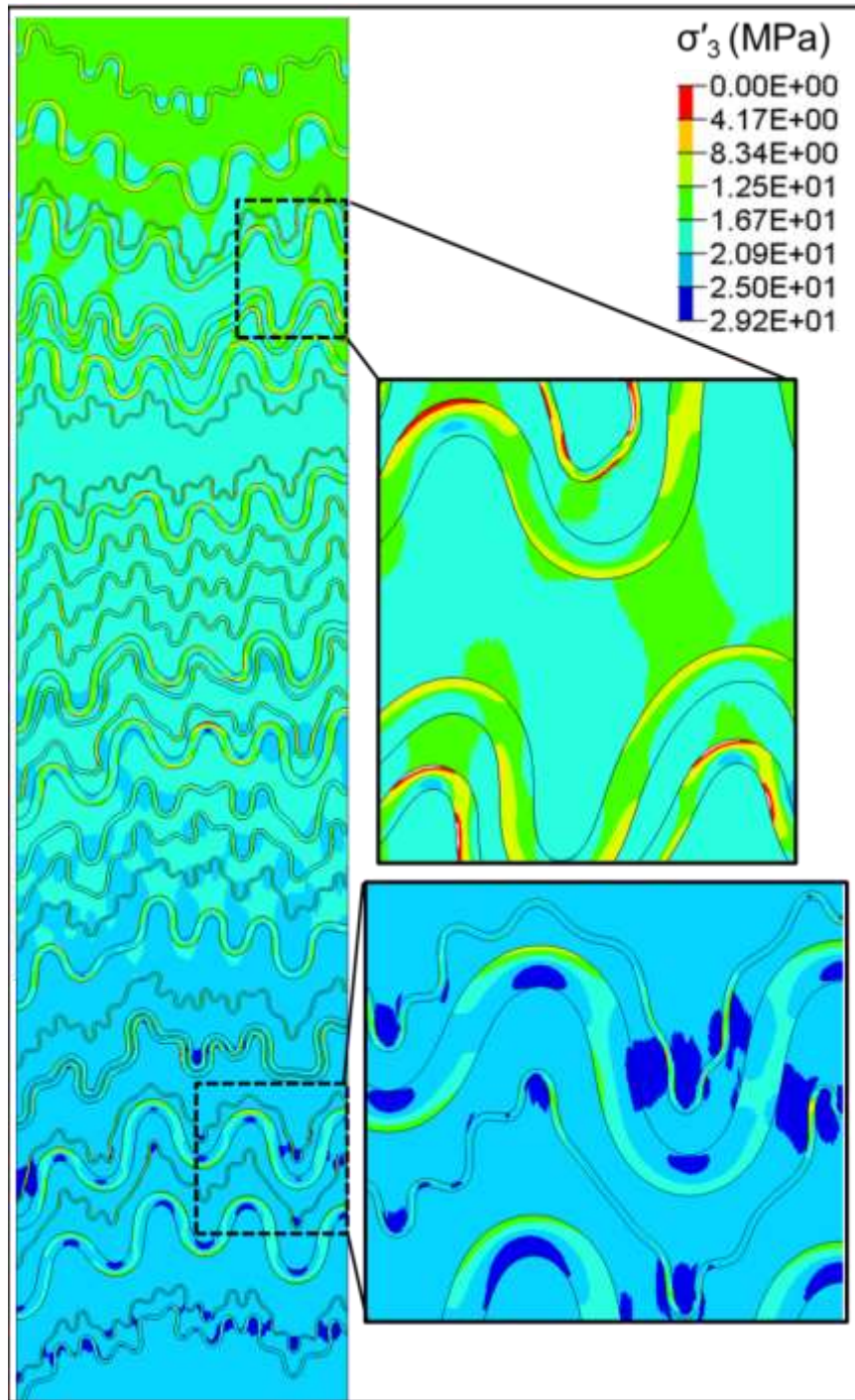
Figure 16. Distribution of the effective minimum principal stress in the multilayer model with various thicknesses.

5. CONCLUSIONS

This study represents the first numerical simulation of visco-elastic multilayer folding with large number of layers (i.e. 10 competent layer) investigating the effects of various model system parameters on the resulting stress and strain distribution under in-situ state of stress with gravity and pore pressure. The 2D numerical models presented illustrate that considering the interplay between initial geometry, material properties and model parameters is necessary in order to better understand the resulting fold shapes and associated parameters such as stress and strain.

The model results show that chevron folds are observed in the core of the multilayer system with noticeable hinge collapse, and concentric folds are observed at the margin of the multilayer stack, which is in agreement with Schmalholz et al.'s (2001) observation. Moreover, the deformation of the multilayer folds show a similar sinusoidal shape of all layers for certain conditions, such as for low viscosity contrast or thick less competent layers. This study demonstrates that the shapes of the multilayer folds with visco-elastic rheology and large number of layers depend on the buckling of the folding layers, which is influenced by various parameters such as initial geometry and material properties and model parameters. It is interesting to note that neither anisotropic material properties nor flexural slip has contributed to the development of these chevron folds at the core of the multilayer stack and associated hinge collapse. The models results indicate that layer number and layer thickness ration are the most critical factors for the development of chevron folds.

The results presented show a large variability in stress and strain distribution due to the complex deformation of both competent and less competent layers during the multilayer buckling process. The numerical modeling results show that tensile stress develops at the top hinge of the antiform and bottom hinge of the synforms for the layers between the core and margin of the multilayer system (i.e. the 3rd and 4th layers at the top half and the 7th and 8th layers at the bottom half of the 10-competent-layer system, Figure 2a). Moreover, tensile stress is also observed at the regions between the limb and the hinge in these layers. The strain distribution shows that little variety of strain is developed in the competent layer and large magnitude of compressive strain is observed

at the limb of the less competent layer close to the margin of the multilayer stack. The numerical simulations also provide a general understanding of the influence of various parameters such as initial geometry, material properties and model parameters on the resulting stress and strain distribution. The results presented here show:

(1) The elastic modulus contrast, R_E, between the competent layer and less competent layer determines the magnitude of tensile stress and compressional strain. A higher RE results in a larger area of tensile stress in the competent layers and the high compressive strain in the less competent layers.

(2) For high viscosity contrast Rμ (between the competent layer and less competent layer), large amplitude of folds and lower maximum principal strain (in compression) is developed in the less competent layers. For low viscosity contrast, the competent layers develop similar sinusoidal shapes.

(3) The initial overburden thickness determines the amount of compression in the model. Lower overburden pressure promotes the onset of tensile stress. Higher overburden pressures decreases the likelihood of tensile stresses at depth and results in larger magnitude of compressive strain.

(4) For large number of layers (N>5), more layers at the core of the multilayer stack deform into chevron folds, and larger area of tensile stress in the competent layers and the high compressive strain in the less competent layers.

(5) While the layer thickness ratio, H/S, is a crucial factor with respect to the generation of various fold shapes, for the porosity distribution, when H/S> 1, the competent layers develop sinusoidal shape and a larger ratio of H/S results in a larger area of tensile stress in the competent layers and less compressive strain in the less competent layers. For H/S <1, smaller ratio of H/S results in a sinusoidal shape of competent layers and low variety of fold shapes and no tensile stress is developed. The distribution of maximum principal strain in the less competent layer is mainly depends on the depth.

In addition, through the applied heterogeneous layer thickness in the multilayer system, this study shows that the fold shape and associated stress distribution become more complicated in the multi-scale multilayer model.

REFERENCES

Sibson, R. H. 1996. Structural permeability of fluid-driven fault-fracture meshes. J. Struct. Geol. 18(8), 1031-1042.

Price N. J. and J.W. Cosgrove. 1990. Analysis of Geological Structures. Cambridge University Press.

Biot, M. A.1961. Theory of folding of stratified viscoelastic media and its implications in tectonics and orogenesis, Geol. Soc. Am. Bull. 72: 1595-1620.

Biot, M.A. 1965. Further development in the theory of internal buckling of multilayers. Geol. Soc. Am. Bull. 76, 833-840.

Cobbold, P.R., Cosgrove, J.W. and J.M. Summers. 1971. Development of internal structures in deformed anisotropic rocks." Tectonophysics. 12.1: 23-53.

Johnson, A.M., and S.D. Ellen. 1974. A theory of concentric, kink, and sinusoidal folding and of monoclinal flexuring of compressible, elastic multilayers: I. Introduction. Tectonophysics. 21.4: 301-339.

Casey, M. 1976. Application of Finite Element Analysis to Some Problems in Structural Geology. PhD. Diss. Imperial College London (University of London).

Ghosh, S.K. 1970. A theoretical study of intersecting fold patterns." Tectonophysics. 9.6: 559-569.

Hunt, G.W., R. Edmunds, C. J. Budd, and J. W. Cosgrove. 2006 Serial parallel folding with friction: a primitive model using cubic B-splines. J. Struct. Geol. 28, 444–455.

Ramberg, H. 1970. Folding of laterally compressed multilayers in the field of gravity. Phys. Earth Planet. Interiors 2, 203–232.

Johnson, A.M. and Fletcher, R. C. 1994. Folding of viscous layers. New York: Columbia University Press.

Schmid, D.W. and Y.Y. Podlachikov. 2006. Fold amplification rates and dominant wavelength selection in multilayer stacks. Phil. Mag. 86: 3409–3423.

Treagus, S.H. and R.C. Fletcher. 2009. Controls of folding on different scales in multilayered rocks. J. Struct. Geol. 31: 1340–1349.

Schmalholz, S.M., Podladchikov, Y. Y. and D. W. Schmid. 2001. A spectral/finite difference method for simulating large deformations of heterogeneous, viscoelastic materials. Geophys J. Int. 145: 199–208.

Schmalholz, S.M. and D. W. Schmid. 2012. Folding in power-law viscous multi-layers." PHILOS. T. ROY. SOC. A. 370.1965: 1798-1826.

Ramberg, H. 1962. Contact strain and folding instability of a multilayered body under compression. Geol. Rdsch. 51: 405–439.

Sherwin, J. and W.M. Chapple. 1968. Wavelengths of single layer folds: a comparison between theory and observation. Am. J. Sci. 266, 167–179.

Frehner, M. and S.M. Schmalholz. 2006. Numerical simulations of parasitic folding in multilayers. J. Struct. Geol. 28: 1647–1657.

Johnson, A.M. 1969. Development of folds within Carmel Formation, Arches national monument. Tectonophysics. 8.1: 31-77.

Ghosh, S.K. 1968. Experiments of buckling of multilayers which permit interlayer gliding. Tectonophysics. 6.3: 207-249.

Ramberg, H. and K.E. Stromgard. 1971. Experimental tests of modern buckling theory applied on multilayered media. Tectonophysics. 11: 461-472.

Debremaccker, J.C. and E.B. Becker. 1978. Finite element models of folding. Tectonophysics. 50: 349-367.

Casey M.and P. Huggenberger. 1985. Numerical modelling of finite-amplitude similar folds developing under general deformation histories. J. Struct. Geol. 7(1): 103-114.

Schmalholz, S.M., Y.Y. Podladchikov, and J.P. Burg. 2002. Control of folding by gravity and matrix thickness: implications for large-scale folding. J. Geophys. Res. 107.

Stephansson, O. 1974, Stress-induced diffusion during folding, Tectonophysics, 22.3: 233-251.

Mancktelow, N.S. 2008. Tectonic pressure: Theoretical concepts and modelled examples, Lithos. 103(1-2): 149-177.

Eckert, A., P. Connolly, and X. Liu. 2014. Large-scale mechanical buckle fold development and the initiation of tensile fractures. Geochem. Geophys. Geosyst. 15(11): 4570-4587.

Cosgrove, J.W. and M.S. Ameen. 1999. A comparison of the geometry, spatial organization and fracture patterns associated with forced folds and buckle folds. Geological Society, London, Special Publications 169.1: 7-21.

Ramsay, J.G. and M.I. Huber. 1987. Strain analysis in the techniques of modern structural geology, vol. 1.London: Academic Press.

Mancktelow, N.S. 1999. Finite-element modeling of single-layer folding in elasto-viscous materials: the effect of initial perturbation geometry, J. Struct. Geol. 21:161-177.

Zhang, Y., N.S. Mancktelow, B.E. Hobbs, A. Ord, and H.B. Muhlhaus. 2000. Numerical modeling of single-layer folding: clarification of an issue regarding the possible effect of computer codes and the influence of initial irregularities, J. Struct. Geol. 22: 1511-1522.

Fowler C.M.R., 1990. The Solid Earth. Cambridge: Cambridge University Press.

Turcotte, D. L. and G. Schubert. 2002. Geodynamics. New York: Cambridge University Press.

Jaeger, J. C., N. G. Cook, and R. W. Zimmerman. 2007. Fundamentals of Rock Mechanics. Oxford: Blackwell Publishing Ltd.

Mühlhaus, H. B., L. Moresi, B. Hobbs, and F. Dufour. 2002. Large amplitude folding in finely layered viscoelastic rock structures. Pure and Applied Geophysics. 159(10), 2311-2333.

Ramberg, H. 1961. Contact strain and folding instability of a multilayered body under compression. Geol Rdsch. 51, 405-439.

Twiss, R.J., and E.M. Moores. 2007. Structural Geology, 2nd Edition. New York: W.H. Freeman and Company.

Medina C.R., J. A. Rupp, and D. A. Barnes. 2011. Effects of reduction in porosity and permeability with depth on storage capacity and injectivity in deep saline aquifers: A case study from the Mount Simon Sandstone aquifer, Int. J. Greenh. Gas Con. 5:146-156.

Buchmann, T. J., and P. T. Connolly 2007. Contemporary kinematics of the Upper Rhine Graben: A 3D finite element approach, Global Planet. Change. 58(1).

Smart, K. J., D. A. Ferrill, and A. P. Morris. 2009. Impact of interlayer slip on fracture prediction from geomechanical models of fault-related folds. AAPG Bull. 93(11):1447-1458.

Eckert, A., and Liu, X. 2014. An improved method for numerically modeling the minimum horizontal stress magnitude in extensional stress regimes. Int. J. Rock. Mech. Min. 70: 581-592.

De Bremaecker, J.C., and Becker, E.B. 1978. Finite element models of folding. Tectonophysics. 50(2):349-367.

Williams, J.R. 1980. Similar and chevron folds in multilayers using finite-element and geometric models. Tectonophysics. 65(3): 323-338.

Ramberg, H. 1963. Fluid dynamics of viscous buckling applicable to folding of layered rocks. Bull. Am. Assoc. Petr. Geol. 47: 484–505.

Ramberg, H. 1964. Selective buckling of composite layers with contrasted rheological properties, a theory for simultaneous formation of several orders of folds. Tectonophysics. 1:307–341.

Metzner, A. B., White, J. L., and Denn, M. M. 1966. Constitutive equations for viscoelastic fluids for short deformation periods and for rapidly changing flows: significance of the Deborah number. AIChE Journal. 12(5): 863-866.

Marshall, R.J., and Metzner, A.B. 1967. Flow of viscoelastic fluids through porous media. Ind. Eng. Chem. Fund. 6(3), 393-400.

Schmalholz, S. M., and Y. Podladchikov. 1999. Buckling versus folding: importance of viscoelasticity. Geophys. Res. Lett. 26(17): 2641-2644.

Jäger, P., S.M. Schmalholz, D.W. Schmid, and E. Kuhl. 2008. Brittle fracture during folding of rocks: A finite element study. Philos. Mag. 88(28-29): 3245-3263.

Price, N. J. 1966. Fault and joint development in brittle and semi-brittle rock, Vol. 1. Oxford: Pergamon Press.

Lemiszki, P. J., J. D. Landes, and R. D. Hatcher. 1994. Controls on hinge-parallel extension fracturing in single-layer tangential-longitudinal strain folds. J. Geophys. Res.-Sol. Ea. (1978–2012), 99(B11): 22027-22041.

Fischer, M. P., and M. S. Wilkerson. 2000. Predicting the orientation of joints from fold shape: Results of pseudo–three-dimensional modeling and curvature analysis. Geology. 28(1): 15-18.

Casey, M., and R. W. Butler (2004), Modelling approaches to understanding fold development: implications for hydrocarbon reservoirs, Mar. Petrol. Geol., 21(7), 933-946, doi: 10.1016/S0264-8172(04)00063-7.

Perritt, S. H., Watkeys, M. K., 2003. Implications of late Pan-African shearing in western Dronning Maud Land, Antarctica. Geological Society, London, Special Publications. 210(1): 135-143.

Bellahsen, N., Fiore, P., Pollard, D. D., 2006. The role of fractures in the structural interpretation of Sheep Mountain Anticline, Wyoming. J. Struct. Geol. 28(5):850-867.

Bergbauer, S., Pollard, D. D., 2004. A new conceptual fold-fracture model including prefolding joints, based on the Emigrant Gap anticline, Wyoming. AAPG Bull. 116(3-4): 294-307.

Ismat, Z., 2008. Folding kinematics expressed in fracture patterns: An example from the Anti-Atlas fold belt, Morocco. J. Struct. Geol. 30(11): 1396-1404.

Sanz, P. F., D.D. Pollard, P.F. Allwardt, and R.I. Borja. 2008. Mechanical models of fracture reactivation and slip on bedding surfaces during folding of the asymmetric anticline at Sheep Mountain, Wyoming. J. Struct. Geol. 30: 1177-1191.

Reber, J. E., S. M. Schmalholz, and J. P. Burg. 2010. Stress orientation and fracturing during three-dimensional buckling: Numerical simulation and application to chocolate-tablet structures in folded turbidites, SW Portugal, Tectonophysics. 493(1), 187-195.

Frehner, M. 2011. The neutral lines in buckle folds. J. Struct. Geol. 33(10): 1501-1508.

Zhang, Y., G. Lin, P. Roberts and A. Ord. 2007. Numerical modelling of deformation and fluid flow in the Shuikoushan district, Hunan Province, South China, Ore Geology Reviews. 31: 683 261-278.

III. VISCO-ELASTIC PARASITIC FOLDING: INFLUENCES ON THE RESULTING POROSITY DISTRIBUTION

Xiaolong Liu*

Department of Geosciences and Geological and Petroleum Engineering, Missouri University of Science and Technology, Rolla, Missouri. 65401-0140 USA. Email address: xlwz9@mst.edu.Tel:01-573-3414151

Andreas Eckert

Department of Geosciences and Geological and Petroleum Engineering, Missouri University of Science and Technology, Rolla, Missouri 65401-0141. USA.

Peter Connolly

Chevron ETC, 1500 Louisiana St, Houston, TX 77002. USA.

Dean Thornton

Chevron ETC, Hill of Rubislaw, Aberdeen AB156XL, United Kingdom

ABSTRACT

Parasitic folds represent a common structure of multi-scale multilayer folds and the resulting asymmetric S- or Z-shapes and symmetric M-shapes represent a complex strain distribution. How the strain distribution affects the resulting porosity remains unclear. In this study, a 2-D plane strain finite element modeling approach is used to simulate multi-scale, multilayer, viscoelastic buckle folds under in-situ stress and pore pressure conditions. A variety of material and model parameters (including the elastic modulus contrast, number of layers, viscosity contrast, strain rate and layer thickness ratio) are considered and their influence on the shape of parasitic folds and on the resulting porosity distribution is analyzed. This study demonstrates that the shapes of the parasitic folds depend on the buckling of both the large- and small-scale folds and are influenced by the various parameters. The numerical modeling results show a large variability in porosity changes due to the complex distribution of the volumetric strain during the mutli-scale, multi-layer buckling process. Three regions, including the hinge and limb of the less competent layer in the M-shaped folds and the limb of the less competent layer in the Z-shaped folds, feature significant porosity changes. In addition, the numerical simulations provide a general understanding of the influence of the various model parameters on the resulting porosity distribution. Through the applied volumetric stain-porosity-permeability coupling, influences on the resulting fluid flow regimes in multi-scale, multilayer buckling systems are documented.

Key words: Parasitic folds; porosity distribution; fold shapes

1. INTRODUCTION

One type of commonly observed multilayer buckle folding is polyharmonic folding, which is defined as small-scale folds with small wavelengths and amplitudes embedded in large-scale folds featuring large amplitude and wavelength (Ramsay and Huber, 1987; Price and Cosgrove, 1990; Twiss and Moores, 2007; Fossen, 2016). The small-scale folds, termed parasitic folds or second-order folds, develop simultaneously with the larger-scale fold and normally show asymmetric S- or Z-shapes in the limbs of the larger-scale fold and symmetric M-shapes in the hinge zones of the large-scale fold (Ramsay and Huber, 1987).

Numerous studies have been performed on multilayer buckle folding (e.g. theoretical: Biot, 1965, Johnson, 1969; Johnson and Fletcher, 1994; analogue: Ghosh, 1968; Cobbold et al., 1971; Ramberg and Strömgard, 1971; numerical: Debremaecker and Becker, 1978; Casey and Huggenberger, 1985; Schmalholz et al., 2001) and on the development of parasitic folds (e.g. theoretical: Ramberg, 1963, 1964; Hunt et al., 2001; Treagus and Fletcher, 2009; analogue: Ramberg, 1963, 1964; Pfaff and Johnson, 1989; and numerical: Frehner and Schmalholz, 2006; Frehner and Schmid, 2016). Ramberg (1963, 1964) showed that parasitic folds may develop in multilayer sequences when the individual layers have different thicknesses and mechanical strengths based on the concept of the dominant wavelength (Biot, 1961). Treagus and Fletcher (2009) suggest that small folds in one layer are likely to develop parasitic folds when the small folds are the most competent layers.

The growth of parasitic folds can be divided into two stages (Ramberg, 1963; Frehner and Schmalholz, 2006). In the first stage of buckling, during horizontal shortening, the small-scale layers develop into symmetric folds with a short wavelength and a low finite amplitudes resulting in a faster amplification rate than the large-scale layers. The second stage represents the shearing of the small-scale folds and the associated development of asymmetric geometries (i.e. S- and Z-shaped) in the limb of the large-scale fold, which is caused by the buckling of the large-scale folds. In the hinge area of the large-scale folds, shearing is less significant and the parasitic folds remain symmetric (M-shaped folds; Ramsay and Huber, 1987; Frehner and Schmalholz, 2006).

A review of numerical modeling studies (e.g. Frehner and Schmalholz, 2006; Frehner and Schmid, 2016) investigating the development of parasitic folds shows that a great amount of knowledge has been gained on the evolution of parasitic folds and their strain history. Frehner and Schmalholz (2006) conclude that the number of small-scale folds are important to the development of asymmetric parasitic folds and a large number of small-scale folds requires less shortening to develop parasitic folds.

Although Ramberg's theory on the development of parasitic folds has been verified for elastic materials (e.g. Ramberg, 1963) and viscous materials (e.g. Frehner and Schmalholz, 2006), the viscoelastic behavior of deformed geological materials (e.g. Ramsay and Huber, 1987; Turcotte and Schubert, 2002; Fowler, 2005) has not been considered for parasitic folds. Schmalholz and Podladchikov (1999, 2001) have shown the importance of viscoelastic single-layer buckling with respect to the dominant wavelength selection, and viscoelastic rheology has been adopted in recent single-layer buckling studies by Eckert et al. (2014, 2015) and Liu et al. (2016). These studies have shown that viscoelastic rheology enables the investigation of both viscous and elastic contributions to the evolution of stress and strain. Considering that the volumetric strain represents porosity changes when the volume change in the solid matrix is neglected (Jaeger et al., 2009), viscoelastic rheology is an appropriate material definition for the study of porosity evolution in high strain zones such as buckle folds. The understanding of the porosity and permeability evolution associated to deformation is of significant importance, since the accumulation and redistribution of fluids and minerals in folds is controlled by the spatial distribution of permeability and porosity (e.g. Du Rouchet 1981; Walder and Nur 1984; Ord and Oliver 1997; Ju et al. 2009; Evans and Fischer 2012; Eckert et al., 2016).

In porous, granular rocks, compaction related porosity-loss is observed which in turn significantly reduces the permeability of deformed rocks by one to four orders of magnitude relative to the host rock matrix (Pittman, 1981). The change of porosity due to vertical compaction and lateral loading depends strongly on the lithology (Dewhurst et al., 1998), grain-scale deformation such as grain-contact dissolution (Rutter and Elliott,1976; Tada, et al. 1987; Hickman and Evans, 1995; Dewers and Hajash, 1995) and associated deformational structures (e.g. deformation bands: Fossen, et al 2007; folds:

Souque et al. 2010; faults: Faulkner and Rutter, 2000, 2003) A great amount of knowledge has been gained on the evolution of porosity and permeability during elastic deformation processes such as brittle faulting and dilatant cataclastic flow (e.g. Zhu and Wong, 1997; Heiland and Raab, 2001; Holcomb and Olsson, 2003; Main et al., 2000; Ngwenya et al., 2003; Ojala et al., 2004; Vajdova et al., 2004), and fault gouges (Faulkner and Rutter, 2000, 2003; Uehara and Shimamoto, 2004). Even though viscous deformation has been identified in contributing to porosity changes during compaction in sedimentary rocks (Bathurst, 1971; Tada and Siever, 1989; Yang 2010), to the authors' knowledge, no study has addressed the influence of viscous and/or viscoelastic deformation on the resulting porosity evolution during multilayer folding (including parasitic folds).

The main objective of this study is to simulate parasitic folds within a multilayer folding system for a viscoelastic rheology. Of particular interest is to quantify the influence of material and model parameters, and fold geometry on the small-scale spatial evolution of porosity and associated permeability during deformation. 2D plane-strain finite element analysis (FEA) is used to simulate the development of parasitic folds under in-situ stress and pore pressure conditions. While this approach has been successfully applied to large-scale single-layer buckle folds to study the deformation related fluid flow patterns (Eckert et al., 2016), this study additionally accounts for porosity related permeability changes in a multi-scale multi-layer fold system.

2.   MODELING APPROACH

2.1. GOVERNING EQUATIONS

In this study, the parasitic folds are simulated in a multilayer system with visco-elastic rheology (e.g.Ramsay and Huber 1987; Turcotte and Schubert, 2002; Fowler 2005) and a linear Maxwell model is utilized following the studies of Mancktelow (1999), Zhang et al. (2000), Schmalholz et al. (2001), Eckert et al. (2014, 2015) and Liu et al. (2016). The Maxwell model, which is utilized in numerical simulation of buckling, features instantaneous elastic deformation under fast strain rates and time-dependent viscous behavior under slower strain rates which is especially suitable to simulate buckling (Schmalholz et al., 2001). For the multilayer system where parasitic folds develop, it is assumed that folds extend infinitely along the fold axis since many natural folds surfaces can be approximated by the cylindrical fold model (Ramsay and Huber, 1987). Therefore, a 2-dimensional plane strain approach is followed (Eckert et al., 2014, 2015; Liu et al.,2015). The finite element analysis (via the commercial software package ABAQUS^{TM}) is utilized in this study to solve the equations of equilibrium, conservation of mass and constitutive equations. The detailed derivation of the governing equation system is presented by Eckert et al. (2014; i.e. supporting information) and not repeated here.

When utilizing an isotropic viscoelastic rheology, the porosity is related to the volumetric strain which is the sum of the elastic and viscous components of strain and the porosity is given by Chin et al. (2000) and Cappa and Rutqvist (2011):

$$\phi = 1 - (1 - \phi_0)e^{\alpha\varepsilon_v} \tag{1}$$

where ϕ is the porosity, ϕ_0 is the initial porosity, ε_v is volumetric strain and α is the Biot coefficient which equals to 1 under the assumption of incompressible fluid and rock grains.

2.2. MODEL SETUP AND MATERIAL PROPERTIES

Simulation of parasitic folds requires a multi-scale multilayer fold system. The model geometry comprises a sequence of three larger scale, layers of 0.1m thickness (2 competent, 1 less competent) embedded in a less competent matrix of 0.5m thickness (Figure 2). A sequence of 19 smaller scale, thin layers (each has a thickness of 2mm) of

alternating competence (10 competent, 9 less competent) are embedded in the thick less competent layer. The variation of thickness results in the wavelength of the parasitic folds being much smaller than the wavelength of the large-scale folds (Frehner and Schmalholz, 2006). The viscosity of the large-scale layers (μ_l) and small-scale competent layers (μ_s) is the same, which is 100 times the viscosity of the less competent layers/matrix (μ_m). The multi-scale fold system models is setup such that only one wavelength is amplified for each fold. The initial geometry of both the large-scale and small-scale folding layer is characterized by small periodic perturbations of the appropriate dominant wavelength (Biot, 1961; Schmid and Podladchikov, 2006) along the shortening direction (x-axis). The limb dip of the initial perturbation is 2° for the thin layers (following Zhang et al., 1996) and 1° for the thick layers which are both much smaller than the 5° limb dip limit for infinitesimal perturbations (Chapple,1968). The different initial perturbations of the multi-scale fold system result in different timing of fold amplification, i.e. the folding of thin layers develops before that of the thick layers, which corresponds to the two stages of the growth of parasitic folds (Ramberg, 1963). The appropriate dominant wavelengths are selected by the same method presented by Eckert et al. (2014) where the parameter R (after Schmalholz and Podladchikov, 1999; Schmalholz et al.,2001) is applied to determine if the competent layer is folded viscously (R<1) or elastically (R>1). R is the ratio between the multilayer viscous dominant wavelength, λ_{dv}, and the multilayer elastic dominant wavelength, λ_{de}:

$$R = \frac{\lambda_{dv}}{\lambda_{de}} = \sqrt[3]{\frac{N_l \mu_l}{6 \mu_m}} \sqrt{\frac{P_0}{G}} \ or \ \sqrt[3]{\frac{N_s \mu_s}{6 \mu_m}} \sqrt{\frac{P_0}{G}} \tag{2}$$

where N_l is the number of large-scale folding layers, N_s is the number of small-scale folding layers, G is the shear modulus and P_0 is the initial layer parallel stress. For the applied viscosity μ_l (i.e. 10^{21}Pa s) in the numerical models, the initial layer parallel stress is given by $P_0 = 4\mu_l \dot{\varepsilon}$ (Schmalholz and Podladchikov, 1999). With a constant viscosity ratio of 100 (between the large/small-scale folding layer and the matrix; Zhang, et al., 1996; Mancktelow, 1999; Zhang et al., 2000; Frehner and Schmalholz, 2006) R from equation 2 is in the range of 0.009 to 0.033 and indicates that viscous folding is the main deformation during buckling. Therefore, the viscous dominant wavelengths of

$$\lambda_{dv} = 2\pi h \sqrt[3]{\frac{N_l \mu_l}{6\mu_m}} \text{ and } \lambda_{dv} = 2\pi H \sqrt[3]{\frac{N_s \mu_s}{6\mu_m}}$$ (where h and H are the thickness of the large and

small-scale competent layers respectively) are applied for the large-scale and small-scale folds. The model is horizontally compressed under a constant strain rate of 10^{-14} s^{-1} representative of a reasonable geologic deformation rate (Twiss and Moores, 2007) and free slip boundary conditions are applied at the bottom boundary.

A power-law relationship relating the permeability evolution to the porosity evolution is given by:

$$k / k_0 = (\phi / \phi_0)^n \tag{3}$$

Where k_0 is the initial permeability and k is the updated permeability in m^2, and n=6 (Petro et al., 2007; Chin et al., 2000; Cappa and Rutqvist, 2011). The permeability is considered to be anisotropic with the horizontal permeability being 5 times the vertical permeability. The initial porosity ϕ_0 is 0.1 and the initial horizontal permeability is 1×10^{-16} m^2. It should be noted that there are various permeability-porosity relationship for porous rocks and the magnitude of *n* depends on the type of rock and the type of deformation (Bernabe et al., 2003). The focus of this study is on the porosity evolution during the deformation of parasitic folds and the associated spatial distribution of permeability. Therefore, a pre-defined permeability-porosity relationship is applied. Moreover, hydrostatic pore pressure is assigned to the model as an initial condition. Considering the scale of the simulation, constant pore pressure is maintained during the deformation of shortening. All material parameters are given in Table 1, unless specified differently for special cases.

In order to simulate stresses resembling in-situ conditions, a stress initialization procedure (following Buchmann and Connolly, 2007; Smart et al., 2009; Eckert and Liu, 2014) is applied, before subjecting the model domain to horizontal shortening, which induces buckling. The procedure includes a vertical load acting at the top of the model to simulate an overburden load of 1000 m, followed by 50% horizontal shortening along the x-direction with a constant strain rate (10^{-14} s^{-1}).

Table 1. Material properties for general sedimentary rocks for the base model (Eckert et al., 2014).

Properties	Folding Layer	Matrix/Overburden/Base
Specific Gravity	2.75	2.75
Viscosity	10^{21} (Pa s)	2×10^{19} (Pa s)
Young's Modulus	30 (GPa)	$30/R_E$ (GPa)
Poisson Ratio	0.25	0.25
Permeability (horizontally)	1×10^{-16} (m^2)	1×10^{-16} (m^2)
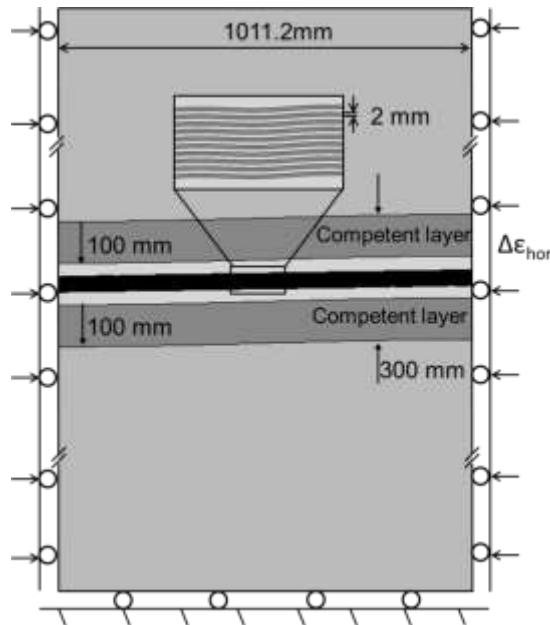
Figure 1. Sketch (not to scale) of the 2D numerical model setup and boundary condition. A large-scale 3-layer multilayer is embedded in a matrix with lower viscosity and elastic strength. The thickness of the three layers are 100 mm and the layer between the two competent layers features lower viscosity and elastic strength. A small-scale multilayer sequence consisting of 10 thin competent layers and 9 thin less competent layers is placed in the large-scale less competent layer. All the thin layers in the multilayer sequence are assigned with the same thickness of 2mm.

2.3. LIMITATIONS

It is clear that utilizing a 2-D plane strain approach for simulating multilayer viscoelastic buckle folds implies cylindrical fold geometry and thus limitations arise. The

2D geometry is adopted to enable simple comparison with the study of Frehner and Schmalholz (2006). While 3D modeling enables more sophisticated and detailed analysis of the spatio-temporal evolution of stress/strain in the folding layer when compared to 2D models (e.g. Eckert et al.,2014; Liu et al., 2016), the 3D geometry of parasitic folds remains unclear, since it is difficult to determine the 3D geometry of parasitic folds from field observations.

In this study, the same small periodic perturbation is used as the initial geometry for the small-scale folds. In nature, layers composed of different rock types are impossible to feature perfect periodic perturbations and the shape of the perturbation is influenced by various factors (Frehner and Schmalholz, 2006), for example, sedimentary structures (e.g. wave ripples) or metamorphic processes (e.g. crenulation). Random perturbations of the initial geometry, which are used by Frehner and Schmalholz (2006) and Frehner and Schmid (2016) may produce comparable results. However, it can be expected that the fundamental deformation of parasitic folds remains the same, which is that small-scale folds are first generated symmetrically and then deformed into parasitic folds by the development of the large-scale fold. Moreover, the focus in this study is on the porosity distribution during the deformation of parasitic folds and the influence from various parameters such as layer number and thickness ratios; the same periodic perturbation is used to generate the same small-scale folds in the early stage before buckling of the large-scale fold in order to exclude the impact of random initial perturbation on the porosity distribution.

3. RESULTS

In the following result analysis the influence of elastic modulus contrast, number of thin layers, viscosity contrast, strain rate, and of the thickness ratio (of the thin competent to the thin less competent layers) is investigated. For all porosity contour plots in the results analysis the color scale is adjusted such that red colored contours always represent porosity increase (i.e. above the initial porosity of 0.1).

3.1. REFERENCE MODEL

To better compare the spatial distribution of porosity of parasitic folds within a multilayer system, a reference model (with the same initial geometry) is presented here, in which all the thin layers feature the same material as the large-scale less competent layer and matrix, i.e. no competence contrast is assigned to the thin layers. Figure 2 shows the distribution of porosity and volumetric strain after 50% shortening. Positive values of volumetric strain indicates compressive strain. It is observed that the porosity of the large-scale competent layer is close to the initial magnitude (i.e. 10%) and only a small amount of volumetric strain (~0.1%) is developed during buckling. For the thin layers, no amplification of small-scale folding is observed, with no influence on the porosity distribution. The porosity distribution within the less competent layer shows reduced magnitudes in the limb and the lowest magnitudes at the top of the hinge zone. This can be explained by the volumetric strain distribution after 50% shortening (Figure 2b), where significant compressive strain is generated at the top of the hinge and in the limb close to the large-scale competent layer (i.e. orange and red areas in Figure 2b). This observation of volumetric strain matches Frehner and Schmalholz's (2006) findings about the strain distribution in multilayer folds with a Newtonian viscous material.

3.2. INFLUENCE OF ELASTIC MODULUS CONTRAST

In order to evaluate the influence of the elastic modulus contrast (i.e. the ratio of Young's Modulus), R_E, between the thin competent layer and the interlayers, two magnitudes of R_E of 1 and 30 are applied to the thin layers. It should be noted that the less competent layers have the same material properties as the large-scale less competent

layer and the elastic modulus contrast between the large-scale competent and less competent layers is constant (i.e. R_E'=30).
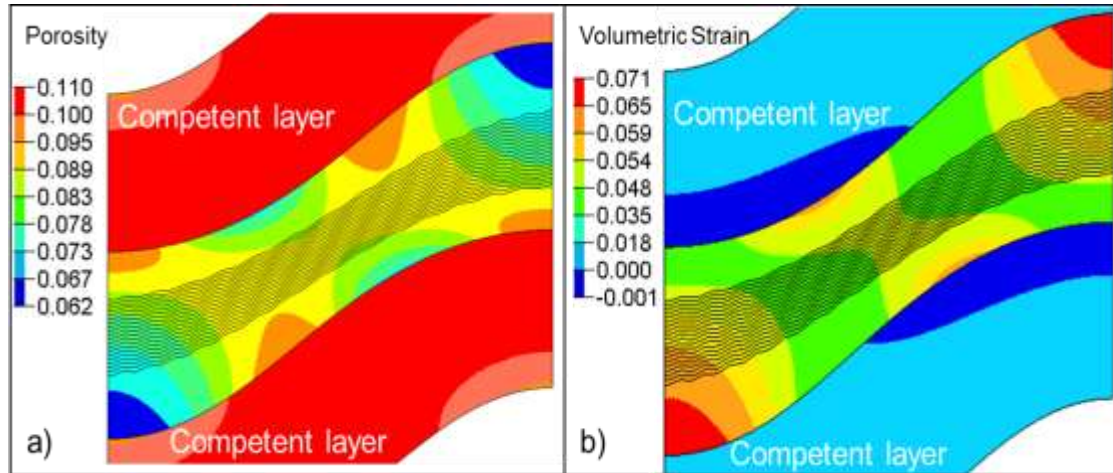
Figure 2. Reference model after 50% bulk shortening of a 3 layer multilayer system, in which the small-scale layers do not have a competence contrast. The porosity distribution (a) spatially corresponds to the distribution of volumetric strain (b), i.e. low porosity in areas of high compressive volumetric strain.

Figure 3 shows the deformed small-scale multilayer folds after 50% bulk shortening for R_E= 1 and R_E= 30. For both models, parasitic folds are observed throughout the large-scale less competent layer with asymmetric Z-shaped folds in the limb region and symmetric M-shaped folds in the hinge region. The shape of the parasitic folds in the limb region is strongly influenced by R_E while the large-scale fold shape remains similar. Since the thicknesses of the parasitic fold layers vary significantly with respect to their location, the ratio A/H (where A represents fold amplitude, and H is the layer thickness) which is commonly used to describe fold shape (e.g. Schmalholz and Podladchikov, 2001, Frehner and Schmalholz, 2006) is replaced by the normalized amplitude A'=A/H_0 (where H_0 is the initial thickness of the thin layer). For R_E=1, the M-shaped small-scale folds exhibit a lower amplitude (A'=3.51) and inter-limb angel (α =75°) compared to R_E=30 (A'=4.19, α =77°). More significant differences of the geometry are observed for the Z-shaped folds, i.e. A'=0.80 and α=106° for R_E=1 (Figure 3a), compared to A'=2.83 and α =116° when R_E=30 (Figure 3b). The observation that the

amplitudes of the parasitic folds decrease from the hinge to the limb of the larger-scale fold are in agreement with results by Frehner and Schmalholz (2006).

With respect to the resulting porosity distributions, it is observed that for low R_E, a significant porosity reduction (f=~0.05) occurs in the limb of the M-shaped less competent layers (Figure 3a). Moreover, limb thinning of the less competent layers is observed in the long limb of the asymmetric Z-shaped parasitic folds with porosity decreasing to ~0.07. Limb thickening is observed in the short limb of the asymmetric Z-shaped folds with porosity increasing to ~0.113. For R_E=30, higher amplitude parasitic folds are observed both at the hinge and limb region of the large-scale fold. The porosity of the less competent thin layers in the M-shaped parasitic folds decreases in the limb (~<0.2) and increases at their hinge zone (>0.11, Figure 3b). In the Z-shaped folds, ϕ ~0.147 in the short limb indicating that significant extensional volumetric strain is occurring. In the long limb, the porosity of the less competent thin layers is 0.05, featuring compressive volumetric strain. When the 2 models are further compared to each other, a significant porosity reduction to ~0 can be observed outside the parasitic fold stack in the limb of the large-scale incompetent layer. This can be explained by the combined layer-perpendicular compression induced in this region by the large-scale competent layer and the parasitic folds. The larger amplification of parasitic folds, which results from the high elastic modulus contrast (i.e. R_E=30), generates a more significant compressive strain and a lower porosity compared to the low elastic modulus model (i.e. R_E=1).

In order to validate that the porosity distribution at 50% shortening represents the possibly lowest overall magnitudes, the porosity evolution of two elements located in the center of the two limbs is plotted in Figure A1 in the Appendix. As shown in Figure A1, the magnitudes of the porosity decrease with shortening and drop to the lowest magnitude at end of the shortening.

3.3. INFLUENCE OF THE NUMBER OF THIN COMPETENT LAYERS

To investigate the effect of the number of thin layers on the deformation and porosity distribution of parasitic folds, the original number of thin, competent layers (N=10) is varied to N=5,15 and 20. The rest of the model setup, including large-scale
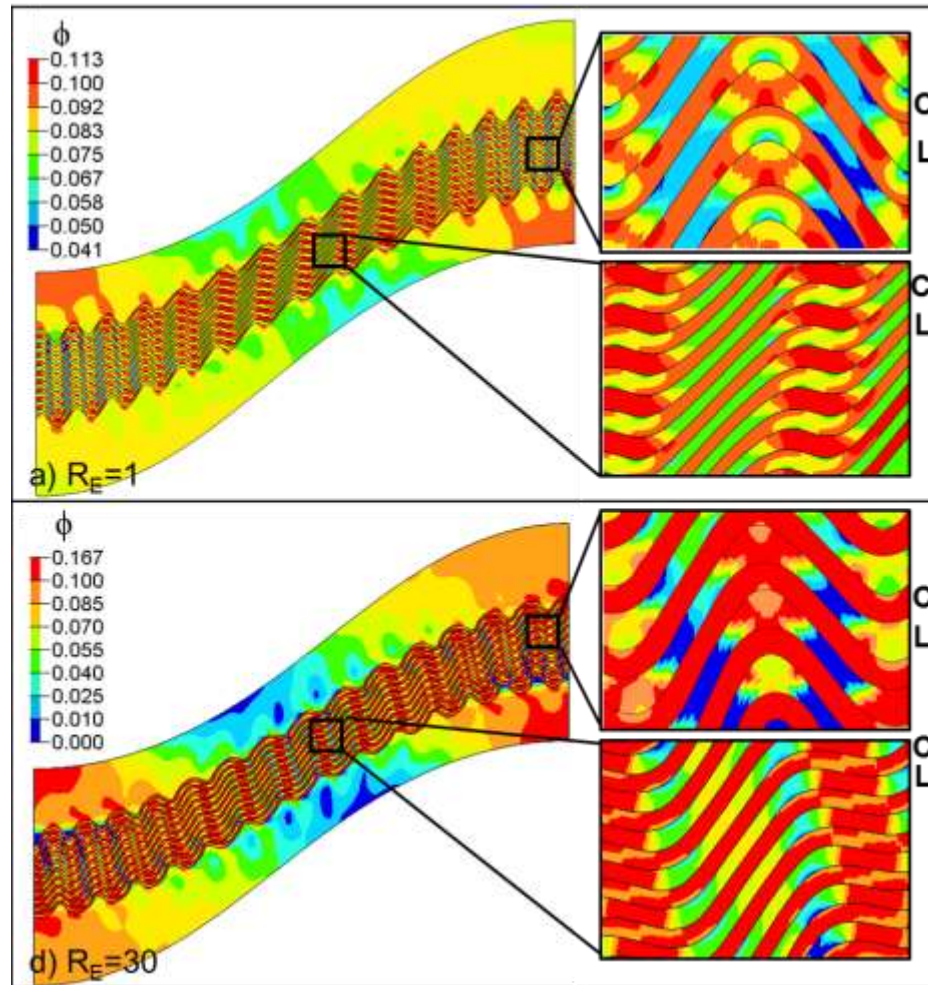
Figure 3. a) Porosity distribution of the large-scale less competent layer and embedded parasitic folds for R_E=1. The upper inset shows the detailed porosity distribution at the M-shaped folds at the hinge of the large-scale layer. The lower inset shows the detailed porosity distribution at the Z-shaped folds in the limb of the large-scale fold. The letters C and L in the insets indicate the competent and less competent thin layers, respectively. b) Porosity distribution of the large-scale less competent layer and embedded parasitic folds for R_E=30.

folds and the thickness of the thin layers, remains the same. Figure 4 shows the normalized amplitude A′ for both the M- and Z-shaped parasitic folds for the tested models. The overall magnitude of the M-shaped parasitic folds at the hinge of the large-scale fold is higher than for the Z-shaped folds. The same observation as seen in Figure 3, that a high R_E increases the amplification of the parasitic folds, is found for all the models (Figure 4). It is also observed that the amplitudes increase when N increases from 5 to 15 for both M-shaped and Z-shaped folds. This can be explained by the amplitude growth

rate, which increases with increasing number of layers for a multilayer system (e.g. Ramberg, 1961; Schmid and Podladchikov, 2006). However, for N=20, a sharp decline in A' for both M-shaped and Z-shaped folds can be observed, and A′ is lower than for N=15. Especially for the model with R_E=1 and N=20, the amplitude of the Z-shaped folds is as low is 2mm, which is close to its initial thickness (2mm).
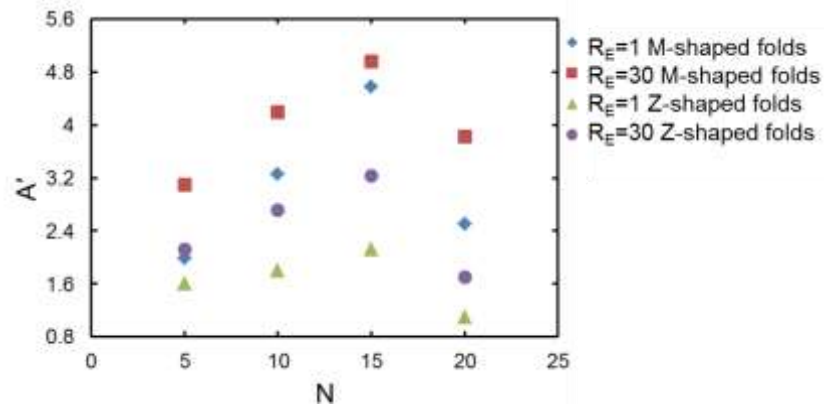
Figure 4. Normalized amplitude, A′, of M-shaped and Z-shaped parasitic folds for varying number of thin, competent layers, N=5,10,15 and 20.

Figure 5 shows the porosity distribution for the deformed small-scale multilayer folds after 50% bulk shortening for N=5,15 and 20 (for both R_E=1 and R_E=30). The observations for the porosity distribution for the various models can be summarized with respect to locations in the hinge zone and limbs of the M- and Z-shaped parasitic folds, and outside the parasitic fold stack in the limb of the large-scale fold:

- For the hinge zone of the M-shaped folds (Figure 5a-f, upper insets) a slight porosity decrease (with a maximum porosity decrease of $\Delta\phi$=0.045 for N=5, R_E=30, Figure 5b upper inset) is observed in the less competent layers for all model variations except for N=15, R_E=30, which features a slight porosity increase ($\Delta\phi$=~0.03, Figure 5d upper inset).

- For the limbs of the M-shaped folds (Figure 5a-f, upper insets) a significant porosity decrease in the less competent layers is observed for all models, with ultra-low porosity (<0.01) for the model with N=5, R_E=30 (Figure 5b, upper inset).

- For the long limb of the Z-shaped folds (Figure 5a-f, lower insets) limb thinning of the less competent layers occurs for all models. This is accompanied by a significant decrease in porosity, with ultralow porosity (<0.01) for the model with N=20, R_E=30 (Figure 5f, lower inset).

- For the short limb of the Z-shaped folds (Figure 5a-f, lower insets) limb thickening of the less competent layers occurs for models with N=5 and 15. This is accompanied by a slight increase in porosity, with a maximum porosity of 0.164 for the model with N=15, R_E=30. For models with N=20, porosity decrease is observed at the short limb of the Z-shaped folds (with a maximum porosity decrease of $\Delta\phi$=0.06 for N=20, R_E=1, Figure 5e lower inset)

- Outside the parasitic fold stack in the limb of the large-scale fold (Figure 5a-f) a significant porosity decrease with increasing layer numbers can be observed (with porosity approaching zero for N=15 and N=20).

For all models it can be observed that the elastic modulus contrast, R_E, influences the degree of porosity changes, i.e. large R_E results in a larger range of porosities.

3.4. INFLUENCE OF VISCOSITY CONTRAST

In order to evaluate the influence of the viscosity contrast, R_μ, between the thin competent and less competent layers, a lower magnitude of R_μ=25 is applied. It should be noted that the viscosity contrast between the large-scale competent layers and less competent layer/matrix is kept at 100 in order to ensure the same fold shape of the large-scale less competent layer after shortening.

For the lower viscosity contrast, significant amplification of the parasitic folds is not observed when R_E=1, and the thin layers exert a limited influence on the porosity distribution, i.e. the overall porosity distribution is similar to the reference model shown in Section 3.1 (Figure 2a). The main difference is that the lowest porosity (~0.075) is observed both at the hinge of the large and small-scale less competent layers (Figure 6b).

Figure 5. Porosity distribution of the large-scale less competent layer and embedded parasitic folds with $R_E=1$ and $N=5$ (a), $R_E=30$ and $N=5$ (b), $R_E=1$ and $N=15$ (c), $R_E=30$ and $N=15$ (d), $R_E=1$ and $N=20$ (e), and $R_E=30$ and $N=20$ (f). The letters C and L in the insets indicate the competent and less competent thin layers, respectively.

For $R_E=30$, the M-shaped folds show a larger amplification of amplitude ($A'=3.73$) than the Z-shaped folds ($A'=0.55$), and both of their magnitudes are much smaller than for the model with a high viscosity contrast (i.e. $\mu_s/\mu_m=100$). This is an expected result, as the viscosity contrast influence on parasitic fold amplification is the same as for regular multilayer folds (Schmid and Podladchikov, 2006). High porosity (~0.134) is observed in the limb of the less competent thin layers and at the bottom of the hinge zone of the large-scale fold. Low porosity (~0.04) is mainly occurring in the limb of the large-scale fold.
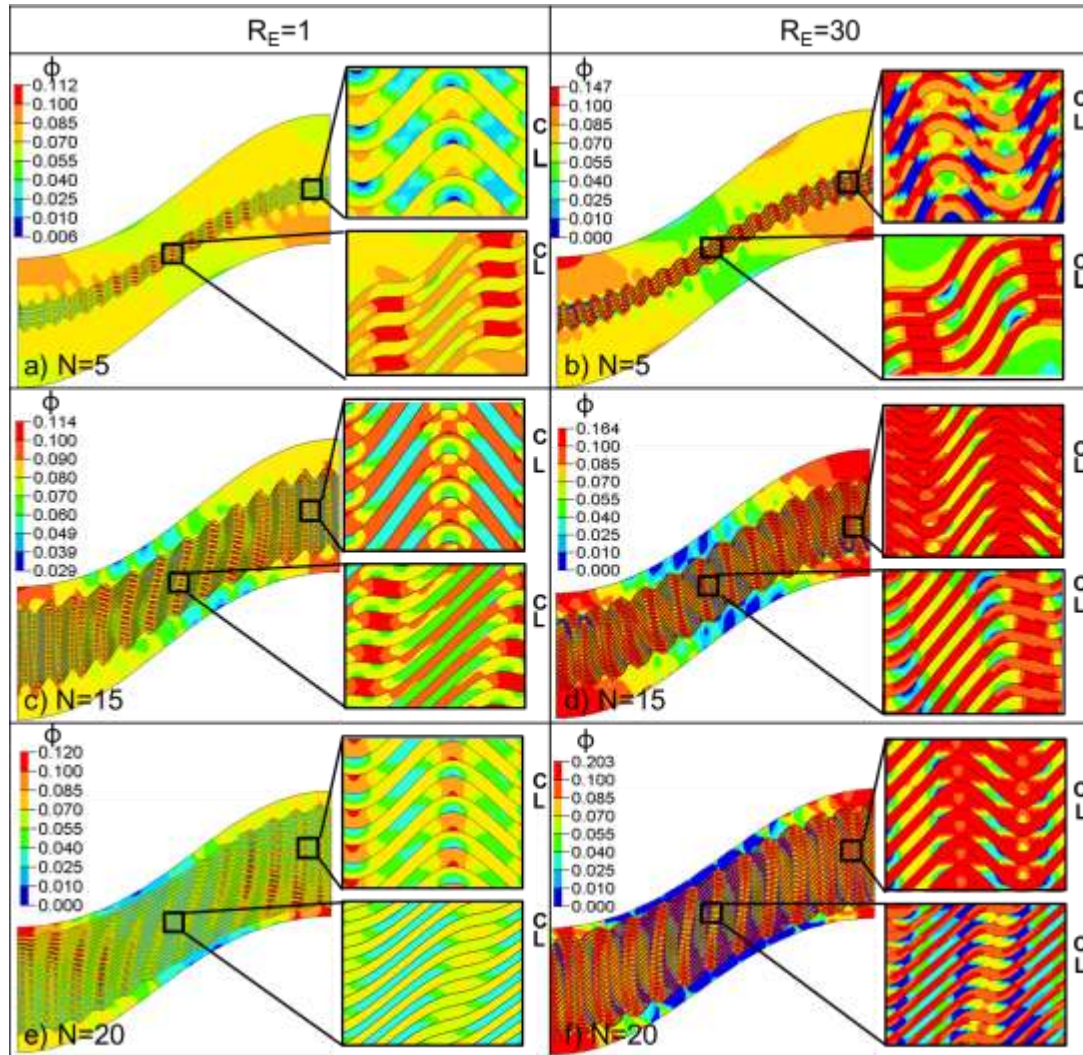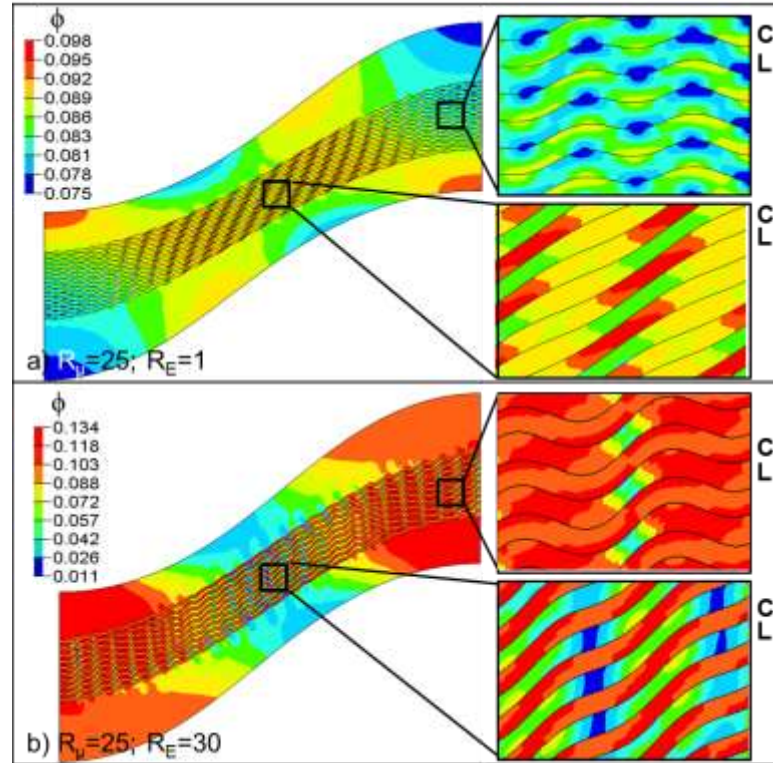
Figure 6. Porosity distribution of the large-scale less competent layer and embedded parasitic folds for $R_\mu=25$ and $R_E=1$ (a) and for $R_\mu=25$ and $R_E=30$ (b). The letters C and L in the insets indicate the competent and less competent thin layers, respectively.

3.5. INFLUENCE OF STRAIN RATE

To investigate the effect of different strain rates on the deformation and porosity evolution of parasitic folds, two more strain rates are assigned. Considering that small folds in quartz or calcite veins in slates or schists or quartz-feldspar veins in granitic rocks are commonly deformed at typical rates of 10^{-14} s^{-1} (Hudleston and Treagus, 2010), the magnitudes of the strain rate investigated here are chosen as 5×10^{-15} s^{-1} and 5×10^{-14} s^{-1}, with viscous folding representing the main deformation during shortening (i.e. R<1). Figure 7a and b show the finial geometry of the parasitic folds after 50% shortening. With the same initial geometry and elastic modulus contrast ($R_E=30$), the M-shaped folds exhibit similar geometry for the two strain rate models ($A´=7.25$ for 5×10^{-15} s^{-1} model and $A´=9.35$ for 5×10^{-15} s^{-1} model, Figure 7a and b, upper inset). A more significant difference in fold shape is observed for the Z-shaped folds with $A´=9.66$ for the low strain rate model and $A´=6.62$ for the high strain rate model (Figure 7a and b, lower

inset). For a better understanding of the differences between the shapes of the Z-shaped folds, the A´ evolution of the large-scale fold and the Z-shaped folds are plotted in Figure 8a and b. The amplitudes of the large-scale fold in the two models increase with shortening (blue curve in Figure 8a and b), with the high strain rate model exhibiting larger amplification during buckling. This is in agreement with Zhang et al.'s (2000) findings on the influence of strain rate on single-layer folding. Figure 8b shows that for the high strain rate model, A´ for the Z-shaped fold increases and reaches the maximum magnitude (A´=10.61) at 32% shortening and then decreases towards A´=6.62 at 50% shortening representing de-amplification of the fold magnitudes. The de-amplification indicates that the growth of the large-scale fold along with the simultaneous limb thinning has a significant influence on the small-scale geometry.

Figure 9 shows the porosity distribution of the parasitic folds for the two strain rate models with R_E=30 after 50% shortening. For the low strain rate model (i.e. 5×10^{-15} s^{-1}), ultralow porosity (<0.01) is observed in the limb of the less competent layers in the M-shaped folds (Figure 9a, upper inset). High porosity (>0.10) is observed in the less competent layers at the hinge zone of the M-shaped folds and in the short limb of the Z-shaped folds (Figure 9a, lower inset). For the model with high strain rate (i.e. 5×10^{-14} s^{-1}), the porosity of the less competent layers in the M-shaped folds decreases in the limb (~<0.01) and increases at their hinge zone (>0.10, Figure 9b, upper inset). In the Z-shaped folds, high porosity (>0.10) in the short limb and ultralow porosity (<0.01) in the long limb are observed in the less competent layers (Figure 9b, lower inset). Compared to the previous model (i.e. low strain rate model), a more significant porosity reduction to ϕ<0.01 can be observed outside the parasitic fold stack in the limb of the large-scale incompetent layer. The porosity distribution for the two strain rates models for a low elastic modulus contrast (i.e. R_E=1) show a similar distribution and hence the observations are not repeated here and the detailed descriptions can found in Appendix B.
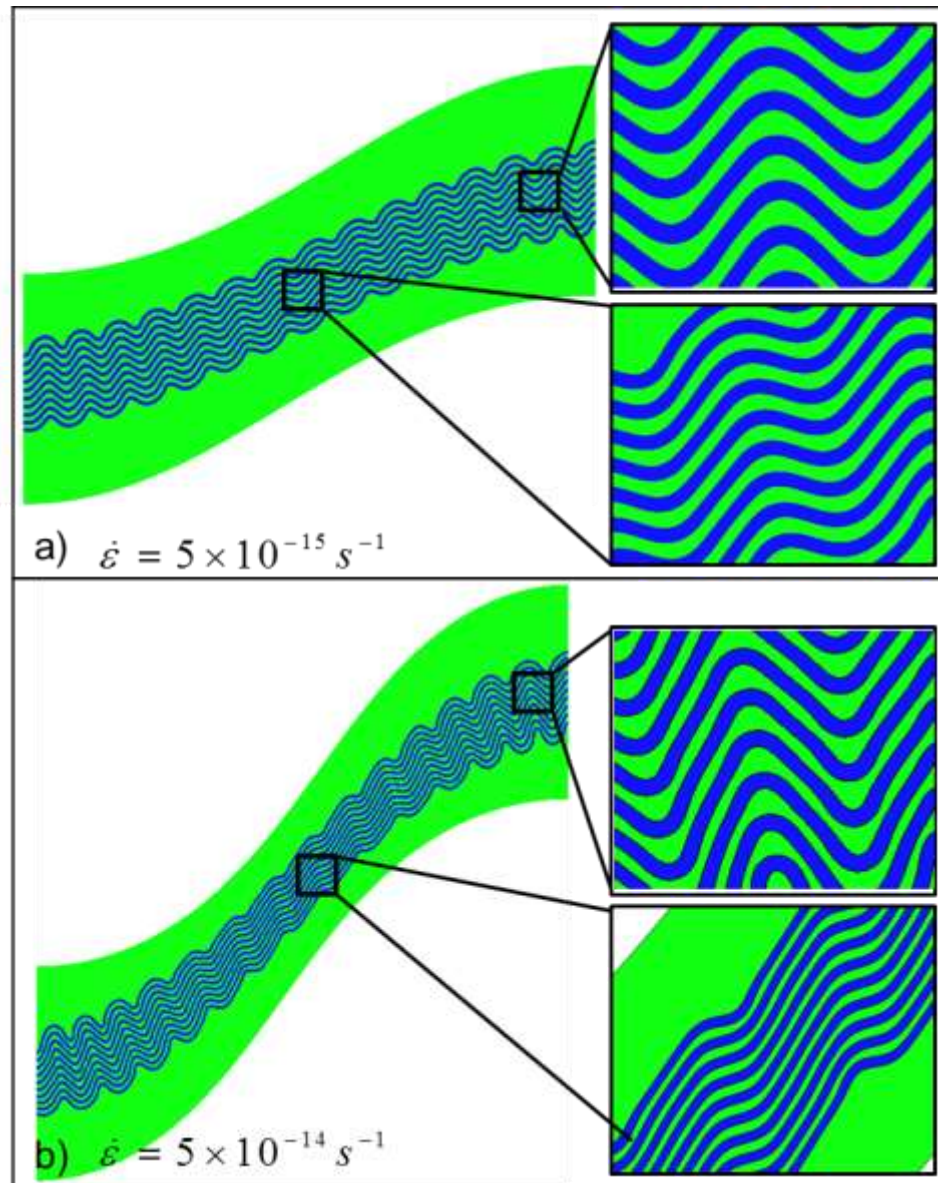
Figure 7. Fold shape of the large-scale less competent layer and embedded parasitic folds for models with strain rates of 5×10^{-15} s^{-1} (a) and 5×10^{-14} s^{-1} (b) at 50% shortening. Blue layers represent thin competent layers. The upper inset shows the detailed M-shaped folds. The lower inset shows the detailed Z-shaped folds.
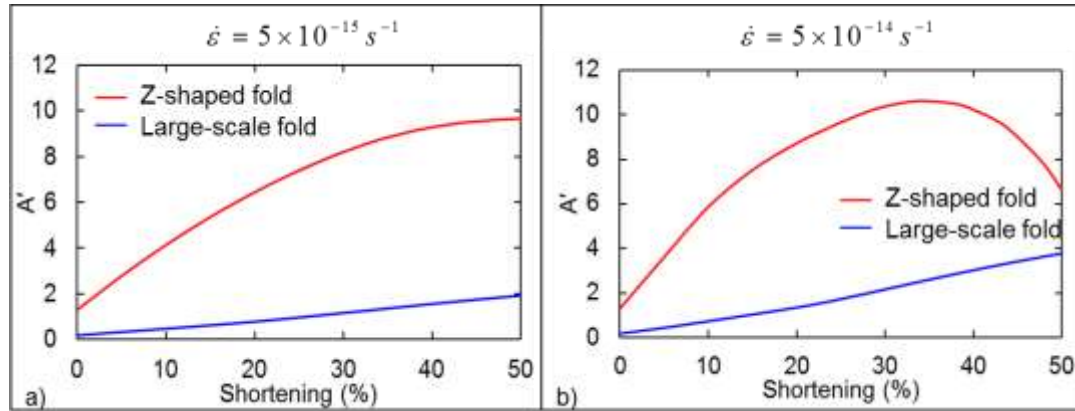
Figure 8. The evolution of the normalized amplitude A´ over shortening of the large-scale and Z-shaped folds for strain rate of 5×10^{-15} s^{-1} (a) and 5×10^{-14} s^{-1} (b).
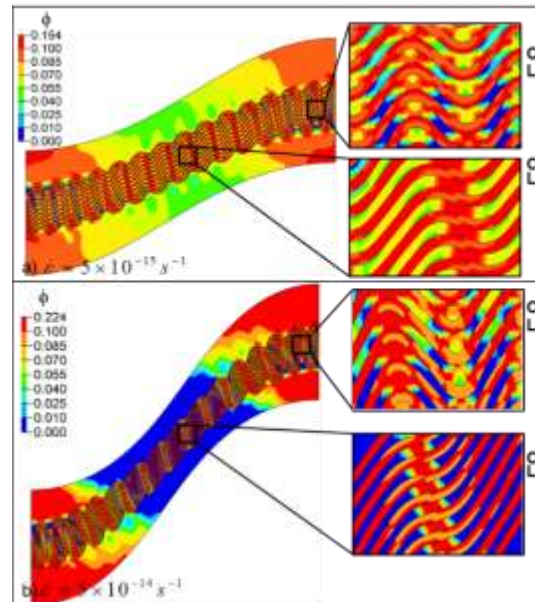
Figure 9. Porosity distribution of the large-scale less competent layer and embedded parasitic folds for low strain rate 5×10^{-15} s^{-1} (a) and high strain rate 5×10^{-14} s^{-1} (b). The letters C and L in the insets indicate the competent and less competent thin layers, respectively.

3.6. INFLUENCE OF THICKNESS RATIO

To investigate the effect of thickness ratio, H/S (with S being the thickness of the small-scale less competent layer), of the small-scale folds, three magnitudes of H/S (2, 0.5 and 1/3) are applied to the models with $R_E= 1$ and $R_E= 30$. It should be pointed out that these magnitudes along with the previous model (i.e. H/S=1) represent true

multilayer buckle folding after Schmid and Podladchikov (2006). Figure 10 shows the deformed small-scale multilayer folds after 50% bulk shortening for $R_E= 1$ and $R_E= 30$.

For H/S=2 and R_E=1 (Figure 10a), M-shaped and Z-shaped parasitic folds are observed in the large-scale less competent layer, with high amplitude (A′=19) for M-shaped folds and low amplitude (A′=5.8) for Z-shaped folds. The observed porosity changes are marginal in the parasitic folds. A porosity reduction (f=~0.065) is observed in the limb of the large-scale fold. For H/S=2 and R_E=30 (Figure 10b), parasitic folds only develop in the hinge region; in the limb of the large-scale fold the thin layers are close to straight. It can also be observed that the small-scale folds in the hinge region form as box folds with rounded hinges and converging paired axial surfaces (Ramsay and Huber, 1987). Low porosity (~0.5) is mainly observed in the limb of the large-scale less competent layer.

Since the models for H/S=0.5 and H/S=0.33 have some similarities, the observations for the porosity distribution for the various models can be summarized with respect to locations in the hinge zone and limbs of the M- and Z-shaped parasitic folds, and outside the parasitic fold stack in the limb of the large-scale fold:

- For the M-shaped folds (Figure 10c-f, upper insets) a significant porosity decrease is observed in the bottom of the hinge of the competent layers for all model variations with R_E=1 (i.e. ϕ=~0.04-0.01). In contrast, for R_E=30, the competent layers show a slight porosity increase, and a slight porosity decrease (i.e. ϕ=~0.07-0.06) is observed in the hinge zone of the less competent layers.
- For the limbs of the M-shaped folds, for R_E=1 (Figure 10c and e, upper insets) a slight porosity decrease in both the competent and less competent layers is observed. For R_E=30 (Figure 10d and f, upper insets), a porosity decrease is observed in the less competent layers (with the lowest porosity of ϕ=0.055 for H/S=0.33, R_E=30, Figure 10f, upper inset).
- For the long limb of the Z-shaped folds (Figure 10c-f, lower insets) limb thinning of the less competent layers occurs for all models except for H=0.33S, R_E=1. The limb thinning is accompanied by a decrease in

porosity (with the lowest porosity of ϕ=0.025 for H/S=0.33, R_E=30, Figure 10f, lower inset).

- In contrast to the models of H/S=1 (Figure 3) which show a porosity increase in the short limb of the less competent layers, a porosity decrease occurs.

- Outside the parasitic fold stack in the limb of the large-scale fold (Figure 10c-f) a significant porosity decrease with increasing elastic contrast can be observed (with porosity approaching zero for models with R_E=30).
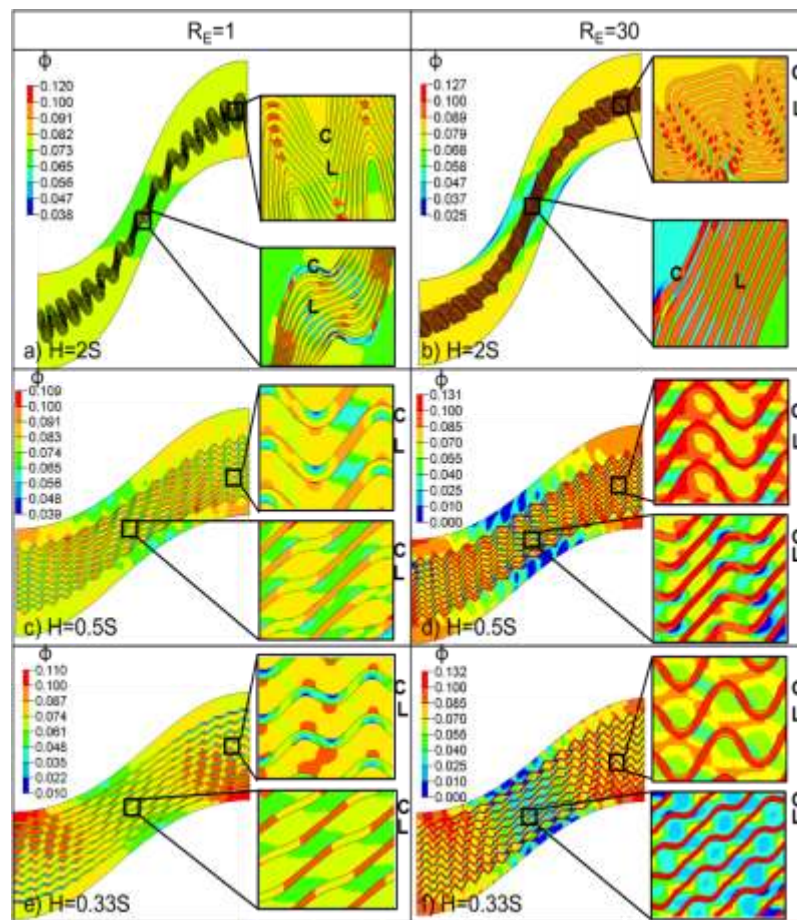
Figure 10. Porosity distribution of the large-scale less competent layer and embedded parasitic folds with R_E=1 and H=2s (a), R_E=30 and H=2s (b), R_E=1 and H=0.5S (c), R_E=30 and H=0.5S (d), R_E=1 and H=0.33S (e),and R_E=30 and H=0.33S (f). The letters C and L in the insets indicate the competent and less competent thin layers, respectively.

To better demonstrate the influence of thickness ratio on the fold shape, Figure 11 shows the normalized amplitudes A' of the M- and Z-shaped parasitic folds for the

variations in H/S. The model with H/S=2 is not included here due to the variability of the occurring fold shapes (i.e. box folds are replacing the M-fold shapes for RE=30). It can be observed that the amplification of fold amplitude increases with H/S and is maximum for H=S. This finding is in agreement with Schmid and Podladchikov (2006), who show that multilayer folds exhibit maximum growth rate when H=S. Moreover, the influence of the elastic ratio, which is increasing the amplification of both M-shaped and Z-shaped parasitic folds, can be observed on all models tested.
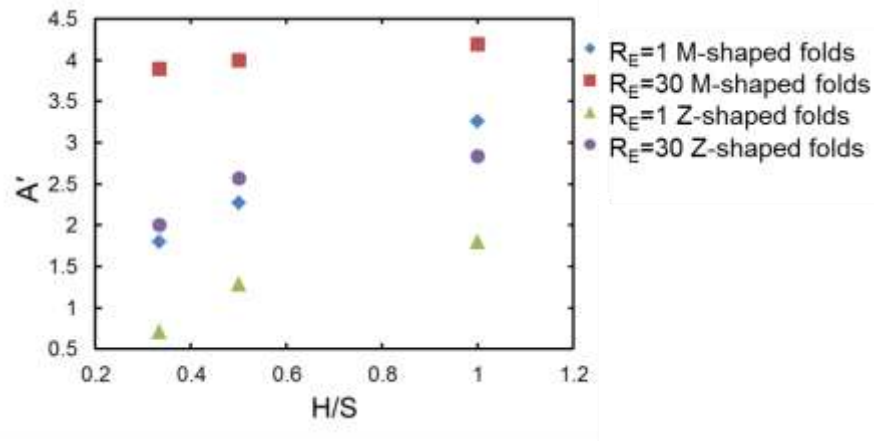
Figure 11. Normalized amplitude of M-shaped and Z-shaped parasitic folds with H=0.33S, H=0.5S and H=S.

4. DISCUSSION

The 2-D plane strain modeling approach presented in this study shows that the deformation of viscoelastic parasitic folds can be successfully simulated and helps to provide a better understanding of parasitic fold development and the associated porosity distribution. A large variety of studies explain the occurrence of parasitic folds in a multilayer fold system (e.g. Ramberg, 1963, 1964; Pfaff and Johnson, 1989; Hunt et al., 2001; Frehner and Schmalholz, 2006; Treagus and Fletcher, 2009; Frehner and Schmid, 2016). From these previous studies, it can be concluded that different rheologies and deformation types can result in the development of parasitic folds, such as linear viscous (Newtonian) rheology (Frehner and Schmalholz, 2006; Treagus and Fletcher, 2009; Frehner and Schmid, 2016), power-law rheology (Fletcher, 1974), and slip between layers (Pfaff and Johnson, 1989). The results in this study verify Ramberg's (1963) theory of the development of parasitic folds using viscoelastic rheology. While these studies have been mainly focusing on the evolution of parasitic fold shapes and their relation to the large-scale fold, this study is the first to quantify the effect of various fold system parameters (such as layer thicknesses, elastic modulus contrast, strain rate, number of layers, and viscosity contrast) on the deformation of the resulting viscoelastic parasitic folds and the associated porosity distribution.

The results presented confirm the basic observations regarding the development of asymmetric parasitic folds as predicted by Frehner and Schmalholz (2006) for a more complex model setup (i.e. simulating in-situ effective stress conditions, as considered here). However, the different model setup also results in some significant differences. Frehner and Schmalholz (2006) observe that for low amplitude parasitic folds deamplification occurs and Z-shaped asymmetric folds do not develop. This "unfolding" of the Z-shaped folds is the result of the compression in the limb (i.e. resulting in limb thinning) of the less competent large-scale fold. This is also observed in this study for models featuring a high strain rate resulting in a high degree of limb thinning (Figure 7 and 8). Moreover, deamplification of Z-shaped folds can also result from other modeling parameters, such as for a low thickness ratio H/S in combination with a high elastic modulus contrast (Figure 10a,b). Frehner and Schmalholz (2006) also conclude that a

large number of thin layers will enhance the development of parasitic folds, which is confirmed in this study, when the number of thin layers increases from 5 to 15. However, the model with 20 competent layers (i.e. a total of 39 small-scale multilayers) shows less amplification of the small-scale folds, which is in contradiction to Frehner and Schmalholz's study (2006). This conflict is due to the different geometry setup of the large-scale less competent layer, which in their study varies its thickness when the number of thin layers is changed. Here, the thickness of the large-scale less competent layer remains constant, and thus the amplification of the parasitic fold stack is inhibited by the limited space of the surrounding less competent material (when N=20).

Moreover, Frehner and Schmalholz (2006) show that the presence of the thin layers has little influence on the dynamics of the two large-scale competent layers. However, the numerical simulations here show that the deformation of the parasitic folds may influence the large-scale folding for certain conditions, such as H/S>1. The normalized amplitude ($A'=A/H_0$) of the large-scale fold ranges from 0.54 when H/S=0.33, to 0.55 when H/S=0.33, and to 0.60 when H/S=0.5, and increases significantly to 1.21 when H/S=2 (the corresponding fold amplitudes can be observed in Figure 10). Despite the different utilized rheologies (i.e. viscous rheology is applied in their study), the conclusion drawn by Frehner and Schmalholz (2006) is based on the fact that the thickness ratio remains constant (H/S=0.33) in their models. It can be concluded that the thickness ratio between the competent and less competent thin layers, especially when it is larger than 1, influences the amplification of the large-scale multilayer system. Clearly, there are other parameters of the small-scale folds that may influence the buckling of multilayer such as an initial asymmetric geometry of the thin layers (Frehner and Schmid, 2016). A detailed investigation on the influence of parasitic folds on the large-scale folding is beyond the scope of the paper but is vary tractable using the numerical simulation presented.

4.1. SHAPE OF PARASITIC FOLDS

In the simulations presented, the Z-shaped folds exhibit a larger variability in fold shapes than the M-shaped folds. This results from the deformation of the Z-shaped folds, which is more complex than either pure or simple shear. The deformation of the large-

scale less competent layer comprises contributions of the layer-perpendicular compression and the layer-parallel extension induced by the buckling of the large-scale competent layers (Frehner and Schmalholz, 2006), and the amplification of the competent layers results in flexural flow between them (Ramsay and Huber, 1987). As a result, the deformation field in the less competent layer is a combination of pure and simple shear (Frehner and Schmalholz, 2006). The pure shear component results in a layer-perpendicular compression, and the simple shear results in a clockwise rotation of the thin layers. Both effects decrease from the large-scale fold limb to the hinge (Ramsay and Huber, 1987; Frehner and Schmalholz, 2006 and Frehner and Schmid, 2016). However, as shown by the variations in the Z-shaped folds in this study (i.e. in the same large-scale fold environment), the effect of the buckling of the thin layers by itself has an influence on the overall deformation of the parasitic folds. This contribution has not been discussed previously, and the models presented in this study provide a better understanding of this effect.

For a discussion of the influence of the small-scale buckling on the Z-shaped folds the models presented in 3.2 featuring different elastic modus contrasts are analyzed in more detail. It is observed that the Z-shaped folds in the limb of the large-scale fold exhibit different fold shapes even though the large-scale fold deforms similarly (Figure 3). Figure 12 shows the respective fold shapes and the distribution and orientations of the principle strains. It can be observed that for the model with $R_E=1$, the Z-shaped folds exhibit a very pronounced thin long limb and a thick short limb (Figure 12a). The minimum (ε_{min}) and maximum principal strains (ε_{max}) of the less competent layers are vertical and horizontal (Figure 12c and e), respectively, indicating the less competent layer undergoes simple shear deformation. The principle strains throughout the less competent layers are compressional (i.e. positive blue contours). For the competent thin layers, ε_{min} is perpendicular to the layer in the short limb, and strain is extensional (i.e. negative red contours). In the long limb, ε_{min} is sub-parallel to the layer, and strain is compressional. No extensional ε_{max} is observed (Figure 12e). For the model with $R_E=30$, the Z-shaped parasitic folds feature a larger inter-limb angle (116° compared to 106° for $R_E=1$) with less tightness. ε_{min} and ε_{max} in the less competent layers are sub-vertical and sub-horizontal, respectively, which are similar to the previous model, indicating that
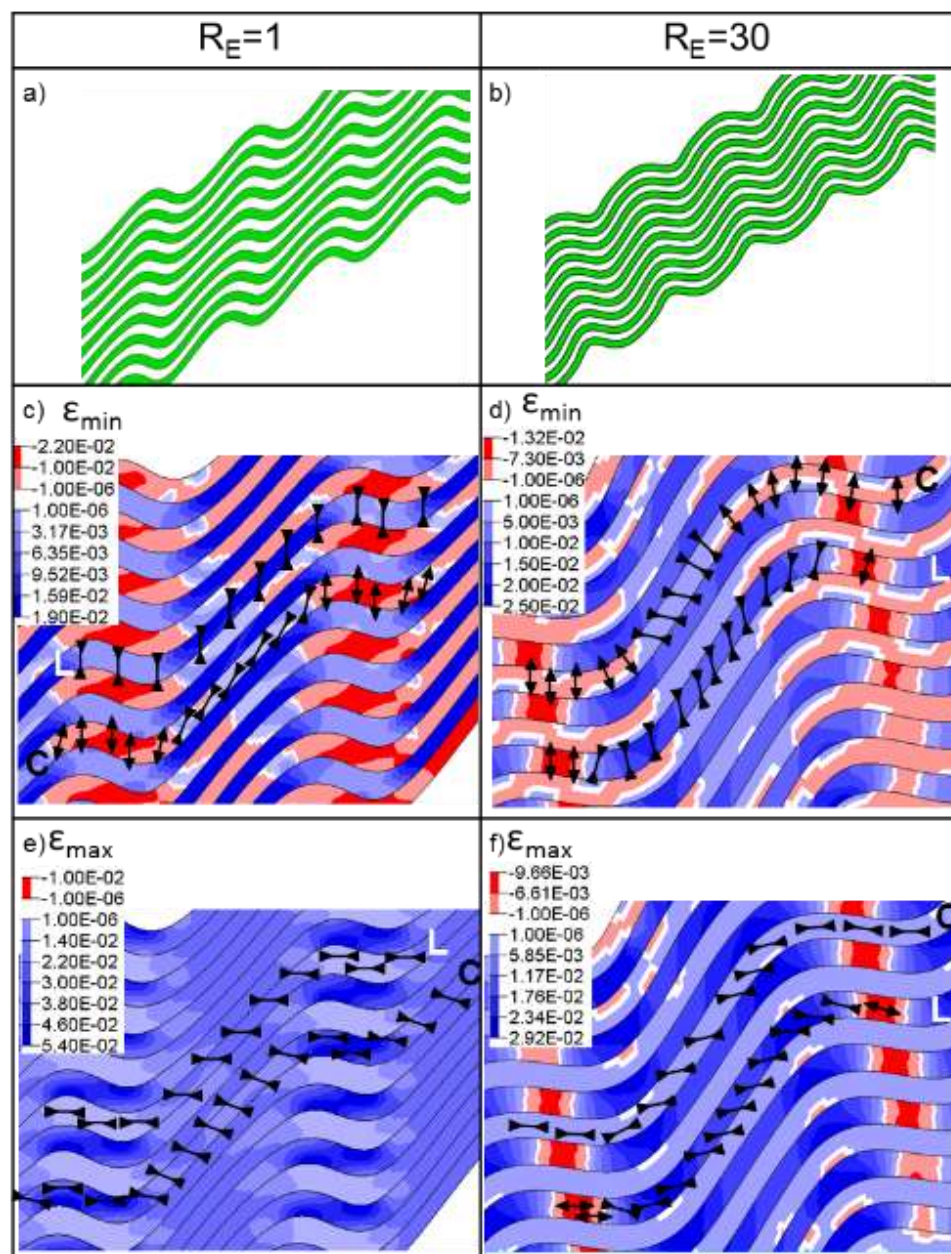
Figure 12. (a) Z-shaped folds of the model with R_E=1. The magnitude and orientation (represented by black arrow) of the minimum and maximum principle strain are shown in (c) and (e); (b) Z-shaped fold of the model with R_E=30. The magnitude and orientation (represented by black arrow) of the minimum and maximum principle strain are shown in (d) and (f). It needs to be noted that the strain orientations are manually plotted (based on the numerical modeling results) on top of the contours due to limited graphical options provided by the analysis software. Original vector and contour plots provided directly by the analysis software can be obtained by contacting the corresponding author.

simple shear is dominating. In contrast to RE=1, only the principal strains in the long limb are compressional, while strains in the short limb are both extensional. For the competent thin layers, εmin is sub-perpendicular to the layer at both the short limb (being extensional) and the long limb (being compressional) and no extensional εmax is observed. The observed change from compressive maximum principle strain in the thin less competent layer when RE=1 to extensional strain in the short limb in when RE=30 indicates a more significant buckling response of the parasitic fold stack. The possible explanation of the two different strain distributions and different shapes is that the high elastic modulus contrast enhances the buckling of the small-scale folds. It needs to be pointed out that the deformation of the parasitic folds, especially for a large elastic modulus contrast, is more complex than a combination of just pure and simple shear, and the small scale buckling has a significant effect on the strain distribution of the parasitic fold stack. This represents an interesting observation and further investigations are necessary, which are beyond the scope of this contribution.

Another important observation is the variation of the shapes of the M-shaped parasitic folds at the hinge zone of the large-scale layer.

- Symmetric M-shaped fold are commonly observed in most models, and the deformation can be explained by the pure shear deformation in the large-scale layer (Frehner and Schmalholz, 2006).

- Chevron folds (which featuring sharp hinges and straight limbs) at the hinge of the large scale layer are observed for the model with H=2S and R_E=1 (Figure 10a) and to some degree for N=15 and R_E=1 (Figure 5c). From these rare manifestations of chevron folds it is clear that the fold shape of the M-shaped folds is the result of a complex interaction of different material properties and fold geometric parameters. It is interesting to note that neither anisotropic material properties (Bayly, 1970; Cobbold et al., 1971; Price and Cosgrove, 1990) nor flexural slip (e.g. Ramsay, 1974, Dubey and Cobbold, 1977, Behzadi and Dubey, 1980; Hudleston et al., 1996)   has contributed to the development of these chevron folds. Similar field observations of chevron shaped parasitic folds

can be found in several studies (e.g. Hobson, 1976; Bergh and Andresen, 1990; Bergh, et al., 1997; Homza and Wallace, 1997; Civile et al., 2000).

- Box folds are observed when $R_E=30$, and the less competent layers become thinner than the competent thin layers. The existence of box folds as parasitic folds is observed by Watkinson (1976) and Andersen (1981). As for the Chevron folds, it is interesting to note that neither flexural slip (e.g. Cobbold et al., 1971; Home and Clushaw, 2001) or buckling of anisotropic rocks (e.g. Ramsay and Huber, 1987; Price and Cosgrove, 1990) have contributed to the development of the box fold shape.

In order to compare the shape evolution of the M-shaped folds featuring chevron (H/S=2 with $R_E=1$) and box folds (H/S=2 with $R_E=1$), Figure 13 shows the shape of the parasitic folds throughout the large-scale fold at different stages of shortening. At 20% shortening, the small-scale folds amplify faster than the large-scale fold and the shapes are the same (as shown in Figure13a and d). At a later stage (i.e. 30% shortening), the parasitic folds with $R_E=1$ deform into sinusoidal shapes (Figure 13b). This sinusoidal shape continues amplifying in the hinge region resulting in chevron folds and rotates in the limb region, resulting in Z-shaped folds at 45% shortening (Figure 13c). In contrast, for $R_E=30$, at 30% shortening the parasitic folds deform into a box shape in the hinge zone and low amplitude, highly asymmetric Z-shaped folds in the limb (Figure 13e). At 45% shortening, the parasitic folds in the hinge region retain the box fold shape and the Z-shaped folds in the limb deamplify and become straight (Figure 13f). Similar geometries of the parasitic folds are also observed for the models with H/S=3/2 (shown in Appendix Figure A1). It needs to be pointed out again that the deformation of these parasitic folds results from the combination of the buckling of the large-scale fold and the buckling of the small-scale layers, which is more complex than simple or pure shearing, thus a straightforward explanation of these various shapes cannot be provided at this stage.
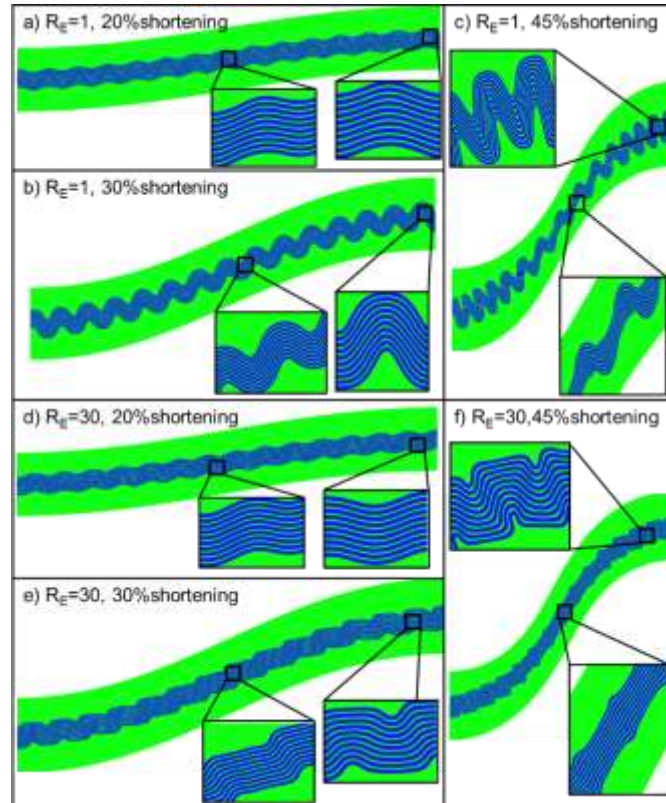
Figure 13. Fold shapes of the large-scale less competent layer and embedded parasitic folds for models with H=2S and R_E=1 (a)-(c) and H=2S and R_E=30(d)-(f) at 20%, 30% and 45% shortening. Blue layers represent the thin, competent layers.

4.2. POROSITY DISTRIBUTION

Numerical modeling results show that the mechanical material properties and their competence contrast are mainly responsible for the strain distribution in large-scale buckle fold structures (e.g. Frehner 2011; Eckert et al., 2014). However, the effect of strain changes on porosity during visco-elastic buckling has not been considered before. However as stated by Yang (2010), mechanical compaction is the most important geological factor contributing to the porosity evolution. This study shows that for a multi-scale, multilayer fold system, various parameters are responsible for the various shapes of the parasitic folds and the associated strain and porosity distribution. Furthermore, the high resolution and detailed distribution of porosity enables to derive associated permeability changes and effects on fluid flow regimes. A comprehensive analysis of the resulting porosity distribution shows that significant changes in porosity can be observed both for the large-scale fold system and for the parasitic folds.

For the cases when both the viscosity contrast and the elastic contrast are low (i.e. $R_\mu = 25$ and $R_E = 1$, see Figure 6a), or when the layer thickness ratio (H/S) is higher than 1 (Figure 10a and b), or when H/S is small along with a low elastic modulus contrast (i.e. $H/S = 0.33$ and $R_E = 1$, see Figure 10e), the porosity in the large scale less competent layers is reduced at the top of the hinge zone and in the limb of the large-scale less competent layer. This can be explained by the large compressional volumetric strain induced by the large-scale buckling (as shown in Figure 2); the influence of the parasitic folds on the overall porosity is negligible. This is also observed in the simulations of multilayer folding (without parasitic folds) by Frehner and Schmalholz (2006). In contrast, for models featuring an increasing number of layers (i.e. Figure 5f), or increasing strain rate (i.e. Figure 9b), or decreasing H/S (i.e. Figure 10 f), the porosity in the limb of the large scale less competent layer becomes ultralow. This indicates that the parasitic folds have significant influence on the overall porosity distribution.

The modeling results presented also show that the porosity also varies significantly within the parasitic fold stack. The observations for the porosity distribution can be summarized with respect to increased (i.e. $\phi > 0.1$) porosity and ultralow porosity (i.e. $\phi < 0.01$):

- Increased porosity is mainly observed in the small-scale competent layers both in the M- and Z-shaped folds for $R_E = 30$ (e.g. Figure 5). This can be explained by the enhanced buckling resulting in extensional volumetric strain. Moreover, increased porosity is also observed in the short limb of the less competent layer in the Z-shaped folds, when $H/S = 1$ and $N < 20$. This finding is in agreement with Schmid and Podladchikov (2006), who show that multilayer folds exhibit maximum growth rate when $H = S$. For models with $H/S < 1$ and/or $N = 20$, the amplification of the parasitic folds is restricted, either due to the increased space between the competent layers ($H/S < 1$), or due to the lack of space outside the parasitic fold stack in the large-scale less competent layer (for $N = 20$).

- The occurrence of ultralow porosity is restricted to the less competent layers, which is under compression induced by the nearby competent

layers. Particular locations include the limb of the M-shaped folds, and the long limb of the Z-shaped folds for models with R_E=30 (e.g. Figure 5).

4.3. PERMEABILITY AND ITS INFLUENCE OF FLUID FLOW

In addition to simulating the porosity evolution the numerical modeling approach accounts for porosity related permeability changes (see equation x). Therefore, through the applied volumetric stain-porosity-permeability coupling, the fluid flow in the multi-scale multilayer system is not just a function of pore pressure. As stated by Ord & Oliver (1997), fluid flow based on mean stress or pore pressure alone may be misleading. Eckert et al. (2015) show that that fluid flow induced by buckling can result in different, even reversed, flow directions depending on the amount of strain and the permeability distribution. However, since the model of Eckert et al. (2015) is based on constant permeability, this study provides an improved understanding of how permeability variations during small-scale multilayer folding affect the resulting fluid flow regimes.

Assuming fluid migration follows Darcy's law (e.g. Jaeger et al., 2007), the pore pressure gradient and the permeability determine the fluid velocities. In order to study the resulting fluid flow pattern in the parasitic folds, a constant pore pressure gradient (10 Pa/mm) is applied to the deformed parasitic fold (of the models shown in section 3.2) horizontally (from the right side of the models to the left) or vertically (from top of the model to the bottom). The resulting permeability distribution and fluid flow magnitudes and vectors are shown in Figure 14. Through equation x it is clear that the distribution of (horizontal) permeability is identical to the porosity distribution (Figure 3), where low permeability is observed in the limb of the large-scale layer and the limb of the less competent small layers. Extremely low permeability ($<1\times10^{-18}$ m^2, compared to the initial permeability of 1×10^{-16} m^2) develops when the porosity decreases to ultralow magnitudes (<0.01), as shown in the limb of the large-scale less competent layer when R_E=30 (Figure 14b).

The resulting fluid flow velocities (v_f) of these models range from 10^{-10} to 10^{-18} m/s (Figure 14c-f), with the lowest magnitudes occurring in the limb of the large-scale less competent layers. For a horizontal pore pressure gradient (Figure 14c and d), a pervasive fluid flow regime exists between the hinge zones of the large-scale less

competent and competent layers. Within the limb of the large-scale less competent layer, fluid flow in the parasitic fold stack becomes focused (i.e. acting as a channel) along the competent small–scale layers. For a vertical pore pressure gradient (Figure 14e and f), a complex fluid flow regime across the large-scale less competent layer develops. Fluid flow is restricted across the limb (Figure 14e and f), and focused flow occurs through the hinge zones of the parasitic folds in the M-shaped folds (Figure 14e and f, insets).

The resulting deformation dependent fluid flow regimes in the multilayer fold systems presented have important implications for commercial fluid flow extraction/injection/storage applications (such as CO_2 sequestration, hydrocarbon production, radioactive waste disposal; Nagel, 2001; Emberley et al., 2005; Delage et al., 2010; Megawati et al., 2012) in reservoirs of folded sedimentary rocks and for hydrothermal ore deposits in metamorphic rocks (Etheridge et al.,1983; Oliver, 1996).
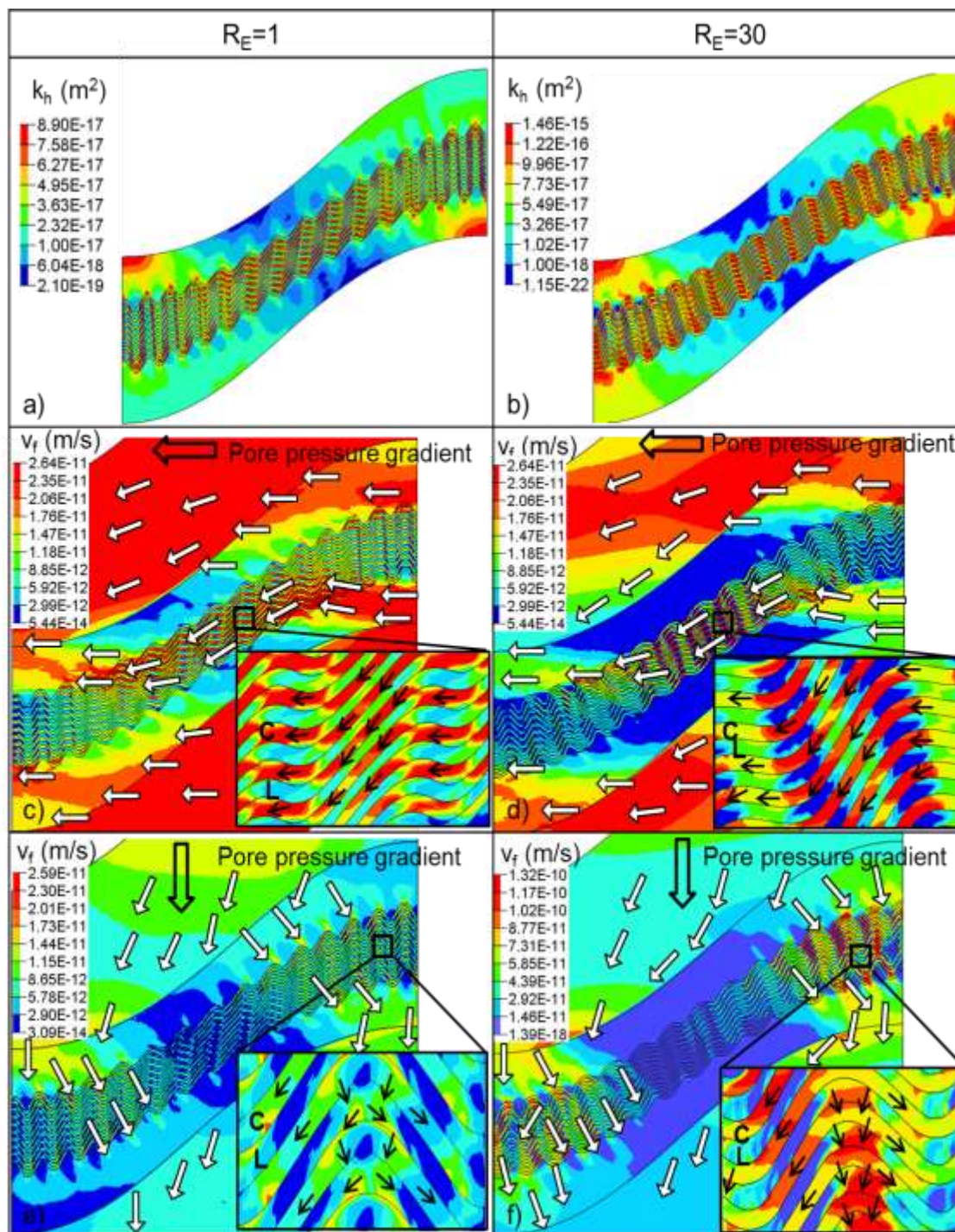
Figure 14. Horizontal permeability distribution of model for $R_E=1$ (a) and $R_E=30$ (b).

The observed fluid flow regimes in Figure 14 become even more pronounced when N=20 and $R_E=30$ (Figure 15).
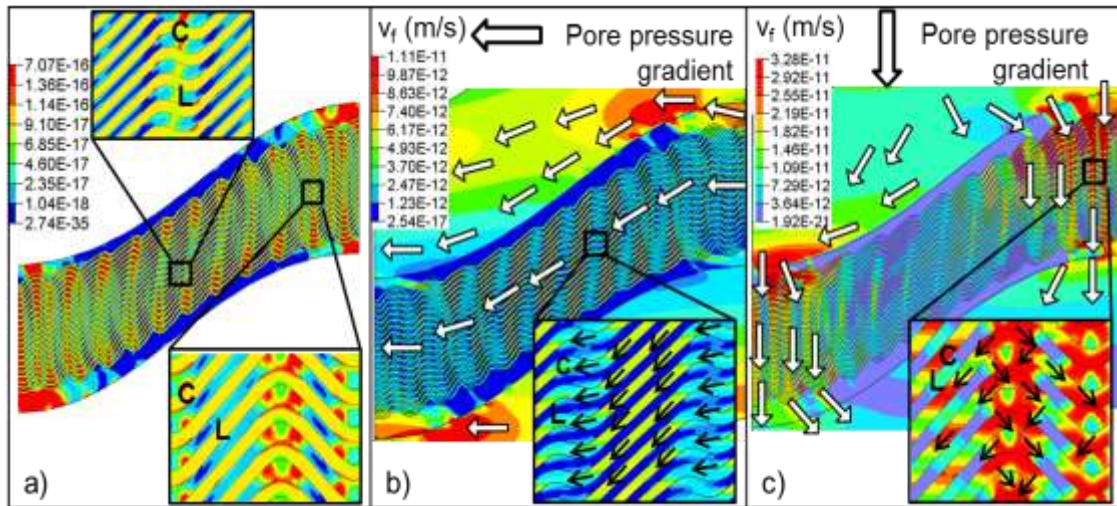
Figure 15. (a) Horizontal permeability distribution of model for N=20 and R_E=30; Fluid flow vector and magnitude contours in the large-scale less competent layer and parasitic folds under horizontal pore pressure gradient (b) and under vertical pore pressure gradient (c).

5. CONCLUSIONS

This study represents the first numerical simulation of multi-layer parasitic folding investigating the effects of various model system parameters on the resulting volumetric strain changes and on the associated porosity distribution. The 2D numerical models presented illustrate that consideringing the interplay between initial geometry, material properties and model boundary conditions is necessary in order to better understand the resulting fold shapes and associated parameters such as porosity.

The model shows that parasitic folds of symmetric M-shapes and asymmetric Z-shapes develop which verifying Ramberg's (1963) theory. Large variability in individual fold shapes including Chevron and box folds in the hinge and unfolded Z-shaped folds as straight layers in the limb of the large-scale fold can develop in the parasitic folds. Moreover, the deformation of the parasitic folds may influence the large-scale folding (i.e. resulting in enhanced fold amplification) for certain conditions, such as H/S>1. This study demonstrates that the shapes of the parasitic folds depend on the buckling of both the large- and small-scale folds, which is influenced by various parameters such as initial geometry, material properties and model boundary conditions.

The results presented show a large variability in porosity changes due to the complex distribution of the volumetric strain during the mutli-scale, multi-layer buckling process. The numerical modeling results show that three regions with significant porosity changes are observed and summarized in Figure 16. The numerical simulations also provide a general understanding of the influence of various parameters such as initial geometry, material properties and model boundary conditions on the resulting porosity distribution. The results presented here show:

1. The elastic modulus contrast, R_E, between the thin competent layer and less competent layer determines the magnitude of compressional volumetric strain. A higher R_E results in a larger range of porosity magnitudes, i.e. higher porosity for extensional strain regions and lower porosity for compressional strain regions.

2. For varying layer numbers (N), the fold amplification of the parasitic folds increases with increasing N, and thus results in a larger range of porosity

131

magnitudes, until a critical thickness is reached when fold amplification reduces significantly.

3. For high viscosity contrast R_μ (between the thin competent layer and less competent layer) and/or high strain rate, significant volumetric strain (in compression and extension) is developed in the less competent layers, resulting in a larger range of porosity magnitudes.

4. While the layer thickness ratio, H/S, is a crucial factor with respect to the generation of various fold shapes, for the porosity distribution, when H/S ≤ 1, larger rations of H/S result in a more significant influence on the regional porosity distribution. For H/S > 1, different fold shapes are observed for the parasitic folds and porosity decrease mainly occurs in the limb of the large-scale fold.

In addition, through the applied volumetric stain-porosity-permeability coupling, this study shows that the resulting fluid flow regimes within small scale structures such as parasitic folds, are significantly affected.
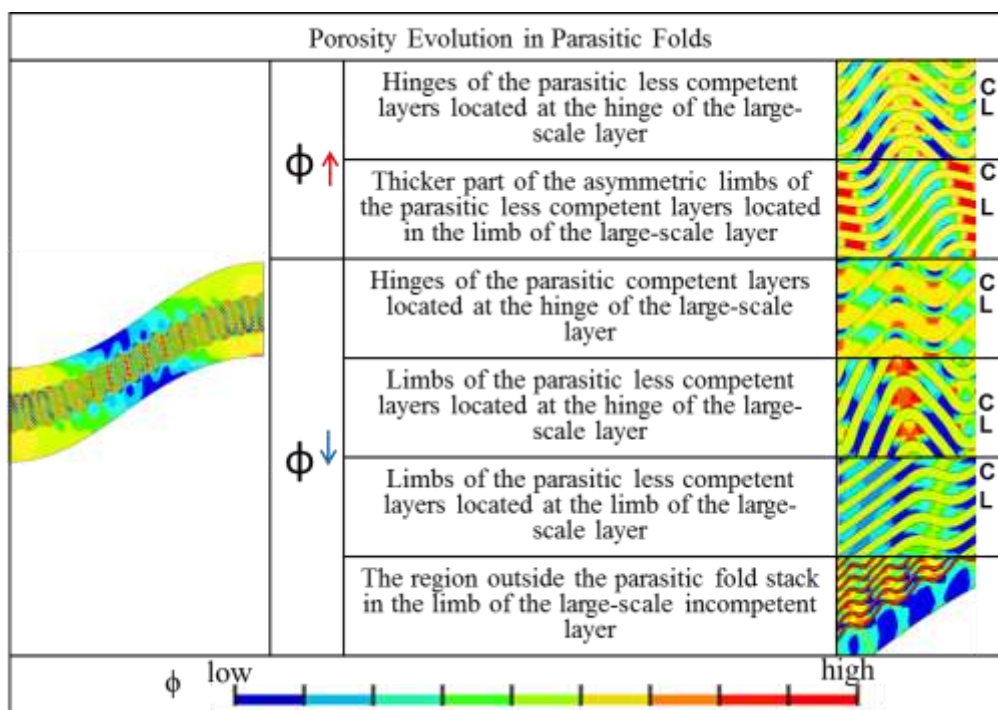

Figure 16. The figure summarizes regions of porosity increase/decrease in parasitic folds.

REFERENCES

Andersen, Torgeir Bjorge. "The structure of the Magerøy Nappe, Finnmark, North Norway." Norges geologiske undersøkelse 363 (1981): 1-23.

Bastida, F., Aller, J. and Bobillo-Ares, N.C., 1999. Geometrical analysis of folded surfaces using simple functions. Journal of structural geology, 21(7), pp.729-742.

Bayly, M.B., 1970. Viscosity and anisotropy estimates from measurements on chevron folds. Tectonophysics, 9(5), pp.459-474.

Bernabé, Y., Mok, U. and Evans, B., 2003. Permeability-porosity relationships in rocks subjected to various evolution processes. Pure and Applied Geophysics, 160(5-6), pp.937-960.

Bergh, S.G. and Andresen, A., 1990. Structural development of the Tertiary fold-and-thrust belt in east Oscar II Land, Spitsbergen. Polar Research, 8(2), pp.217-236.

Bergh, S.G., Braathen, A. and Andresen, A., 1997. Interaction of basement-involved and thin-skinned tectonism in the Tertiary fold-thrust belt of central Spitsbergen, Svalbard. AAPG bulletin, 81(4), pp.637-661.

Biot, M.A., 1961. Theory of folding of stratified viscoelastic media and its implications in tectonics and orogenesis. Geological Society of America Bulletin, 72(11), pp.1595-1620.

Biot, M.A. and Romain, J.E., 1965. Mechanics of incremental deformations. Physics Today, 18, p.68.

Casey, M. and Huggenberger, P., 1985. Numerical modelling of finite-amplitude similar folds developing under general deformation histories. Journal of Structural Geology, 7(1), pp.103-114.

Chapple, W.M., 1968. A Mathematical Theory of Finite–Amplitude Rock–Folding. Geological Society of America Bulletin, 79(1), pp.47-68.

Chin, L.Y., Raghavan, R., Thomas, L.K., 2000. Fully coupled geomechanics and fluid-flow analysis of wells with stress-dependent permeability. SPE J. 5 (1), 32–45,Paper 58968.

Civile, D.A.R.I.O., Martino, C.L.A.U.D.I.O. and Zecchin, M.A.S.S.I.M.O., 2010. Contractional deformation and Neogene tectonic evolution of the Pergola-Melandro valley area (Southern Apennines). GeoActa, 9, pp.1-19.

Cobbold, P.R., Cosgrove, J.W. and Summers, J.M., 1971. Development of internal structures in deformed anisotropic rocks. Tectonophysics, 12(1), pp.23-53.

De Bremaecker, J.C. and Becker, E.B., 1978. Finite element models of folding. Tectonophysics, 50(2), pp.349-367.

Dewers, T. and Hajash, A., 1995. Rate laws for water‐assisted compaction and stress‐induced water‐rock interaction in sandstones. Journal of Geophysical Research: Solid Earth, 100(B7), pp.13093-13112.

Dewhurst, D.N., Aplin, A.C., Sarda, J.P. and Yang, Y., 1998. Compaction‐driven evolution of porosity and permeability in natural mudstones: An experimental study. Journal of Geophysical Research: Solid Earth, 103(B1), pp.651-661.

Dubey, A.K. and Cobbold, P.R., 1977. Noncylindrical flexural slip folds in nature and experiment. Tectonophysics, 38(3-4), pp.223-239.

Du Rouchet, J., 1981. Stress fields, a key to oil migration. AAPG bulletin, 65(1), pp.74-85.

Eckert, A., Connolly, P. and Liu, X., 2014. Large-scale mechanical buckle fold development and the initiation of tensile fractures. Geochemistry, Geophysics, Geosystems, 15(11), pp.4570-4587.

Eckert, A., Liu, X. and Connolly, P., 2015. Pore pressure evolution and fluid flow during visco-elastic single‐layer buckle folding. Geofluids.

Etheridge, M.A., Wall, V.J. and Vernon, R.H., 1983. The role of the fluid phase during regional metamorphism and deformation. Journal of Metamorphic Geology, 1(3), pp.205-226.

Evans, M.A. and Fischer, M.P., 2012. On the distribution of fluids in folds: A review of controlling factors and processes. Journal of Structural Geology, 44, pp.2-24.

Faulkner, D.R. and Rutter, E.H., 2003. The effect of temperature, the nature of the pore fluid, and subyield differential stress on the permeability of phyllosilicate‐rich fault gouge. Journal of Geophysical Research: Solid Earth, 108(B5).

Fowler, C.M.R., 2005. The Solid Earth. Cambridge University Press, Cambridge,pp. 557–577.

Fossen, H., Schultz, R.A., Shipton, Z.K. and Mair, K., 2007. Deformation bands in sandstone: a review. Journal of the Geological Society, 164(4), pp.755-769.

Fossen, H., 2016. Structural geology. Cambridge University Press.

Frehner, M. and Schmalholz, S.M., 2006. Numerical simulations of parasitic folding in multilayers. Journal of Structural Geology, 28(9), pp.1647-1657.

Frehner, M. and Schmid, T., 2016. Parasitic folds with wrong vergence: How pre-existing geometrical asymmetries can be inherited during multilayer buckle folding. Journal of Structural Geology, 87, pp.19-29.

Ghosh, S.K., 1968. Experiments of buckling of multilayers which permit interlayer gliding. Tectonophysics, 6(3), pp.207-249.

Hickman, S.H. and Evans, B., 1995. Kinetics of pressure solution at halite‐silica interfaces and intergranular clay films. Journal of Geophysical Research: Solid Earth, 100(B7), pp.13113-13132.

Heiland, J. and Raab, S., 2001. Experimental investigation of the influence of differential stress on permeability of a Lower Permian (Rotliegend) sandstone deformed in the brittle deformation field. Physics and Chemistry of the Earth, Part A: Solid Earth and Geodesy, 26(1), pp.33-38.

Hobson, D.M., 1976. A structural section between Plymouth and Bolt Tail, south Devon. Proceedings of the Geologists' Association, 87(1), pp.27-43.

Holcomb, D.J. and Olsson, W.A., 2003. Compaction localization and fluid flow. Journal of Geophysical Research: Solid Earth, 108(B6).

Homza, T.X. and Wallace, W.K., 1997. Detachment folds with fixed hinges and variable detachment depth, northeastern Brooks Range, Alaska. Journal of Structural Geology, 19(3-4), pp.337-354.

Horne, R. and Culshaw, N., 2001. Flexural-slip folding in the Meguma group, Nova Scotia, Canada. Journal of Structural Geology, 23(10), pp.1631-1652.

Hudleston, P.J., 1973. Fold morphology and some geometrical implications of theories of fold development. Tectonophysics, 16(1-2), pp.1-46.

Hudleston, P.J., Treagus, S.H. and Lan, L., 1996. Flexural flow folding: Does it occur in nature?. Geology, 24(3), pp.203-206.

Hunt, G.W., Wadee, M.A. and Ord, A., 2001. Length scale interactions in the folding of sandwich structures. Tectonophysics, 335(1), pp.111-120.

Jaeger, J.C., Cook, N.G. and Zimmerman, R., 2009. Fundamentals of rock mechanics. John Wiley & Sons.

Johnson, A.M., 1969. Development of folds within Carmel Formation, Arches national monument, Utah. Tectonophysics, 8(1), pp.31-77.

Johnson, A.M. and Fletcher, R.C., 1994. Folding of viscous layers: mechanical analysis and interpretation of structures in deformed rock. Columbia University Press.

Ju, M. and Yang, J., 2010. Preliminary numerical simulation of tectonic deformation-driven fluid flow: Implications for ore genesis in the Dachang district, South China. Journal of Geochemical Exploration, 106(1), pp.133-136.

Liu, X., Eckert, A. and Connolly, P., 2015. A Comparison of Stress Evolution in Single-layer and Multilayer Buckle Folds. In 49th US Rock Mechanics/Geomechanics Symposium. American Rock Mechanics Association.

Liu, X., Eckert, A. and Connolly, P., 2016. Stress evolution during 3D single-layer visco-elastic buckle folding: Implications for the initiation of fractures. Tectonophysics, 679, pp.140-155.

Liu, C., Zhang, Y. and Wang, Y., 2009. Analysis of complete fold shape based on quadratic Bézier curves. Journal of Structural Geology, 31(6), pp.575-581.

Mancktelow, N.S., 1999. Finite-element modelling of single-layer folding in elasto-viscous materials: the effect of initial perturbation geometry. Journal of Structural Geology, 21(2), pp.161-177.

Main, I.G., Kwon, O., Ngwenya, B.T. and Elphick, S.C., 2000. Fault sealing during deformation-band growth in porous sandstone. Geology, 28(12), pp.1131-1134.

Ngwenya, B.T., Kwon, O., Elphick, S.C. and Main, I.G., 2003. Permeability evolution during progressive development of deformation bands in porous sandstones. Journal of Geophysical Research: Solid Earth, 108(B7).

Ojala, I.O., Ngwenya, B.T. and Main, I.G., 2004. Loading rate dependence of permeability evolution in porous aeolian sandstones. Journal of Geophysical Research: Solid Earth, 109(B1).

Oliver, N.H.S., 1996. Review and classification of structural controls on fluid flow during regional metamorphism. Journal of Metamorphic Geology, 14(4), pp.477-492.

Ord, A., Hobbs, B.E., Zhang, Y., Broadbent, G.C., Brown, M., Willetts, G., Sorjonen‐Ward, P., Walshe, J.L. and Zhao, C., 2002. Geodynamic modelling of the century deposit, Mt Isa Province, Queensland. Australian Journal of Earth Sciences, 49(6), pp.1011-1039.

Ord, A. and Oliver, N.H.S., 1997. Mechanical controls on fluid flow during regional metamorphism: some numerical models. Journal of Metamorphic Geology, 15(3), pp.345-359.

Petro, D.R., Chu, W.C., Burk, M.K. and Rogers, B.A., 1997, January. Benefits of pressure transient testing in evaluating compaction effects: Gulf of Mexico deepwater turbidite sands. In SPE Annual Technical Conference and Exhibition. Society of Petroleum Engineers.

Pittman, E.D., 1981. Effect of fault-related granulation on porosity and permeability of quartz sandstones, Simpson Group (Ordovician), Oklahoma. AAPG Bulletin, 65(11), pp.2381-2387.

Price, N.J. and Cosgrove, J.W., 1990. Analysis of geological structures. Cambridge University Press.

Ramberg, H., 1961. Contact strain and folding instability of a multilayered body under compression. Geologische Rundschau 51,pp. 405-439.

Ramberg, H., 1963. Evolution of drag folds. Geological Magazine, 100(02), pp.97-106.

Ramberg, H., 1964. Selective buckling of composite layers with contrasted rheological properties, a theory for simultaneous formation of several orders of folds. Tectonophysics, 1(4), pp.307-341.

Ramberg, H. and Strömgård, K.E., 1971. Experimental tests of modern buckling theory applied on multilayered media. Tectonophysics, 11(6), pp.461-472.

Ramsay, J.G., 1974. Development of chevron folds. Geological Society of America Bulletin, 85(11), pp.1741-1754.

Ramsay, J.G. and Huber, M.I., 1987. The techniques of modern structural geology: Folds and fractures (Vol. 2). Academic press.

Rutter, E.H. and Elliott, D., 1976. The kinetics of rock deformation by pressure solution [and discussion]. Philosophical Transactions of the Royal Society of London A: Mathematical, Physical and Engineering Sciences, 283(1312), pp.203-219.

Schmalholz, S.M. and Podladchikov, Y., 1999. Buckling versus folding: importance of viscoelasticity. Geophysical Research Letters, 26(17), pp.2641-2644.

Schmalholz, S.M., Podladchikov, Y.Y. and Schmid, D.W., 2001. A spectral/finite difference method for simulating large deformations of heterogeneous, viscoelastic materials. Geophysical Journal International, 145(1), pp.199-208.

Schmid, D.W. and Podladchikov, Y.Y., 2006. Fold amplification rates and dominant wavelength selection in multilayer stacks. Philosophical Magazine, 86(21-22), pp.3409-3423.

Smith-Rouch, L.S., 2006. Oligocene–Miocene Maykop/Diatom Total Petroleum System of the South Caspian Basin Province, Azerbaijan, Iran, and Turkmenistan. US Geological Survey Bulletin, 2201.

Souque, C., Fisher, Q.J., Casey, M. and Bentham, P., 2010. Structural controls on mechanical compaction within sandstones: An example from the Apsheron Peninsula, Azerbaijan. Marine and Petroleum Geology, 27(8), pp.1713-1724.

Srivastava, D.C. and Lisle, R.J., 2004. Rapid analysis of fold shape using Bézier curves. Journal of Structural Geology, 26(9), pp.1553-1559.

Tada, R., Maliva, R. and Siever, R., 1987. A new mechanism for pressure solution in porous quartzose sandstone. Geochimica et Cosmochimica Acta, 51(9), pp.2295-2301.

Treagus, S.H. and Fletcher, R.C., 2009. Controls of folding on different scales in multilayered rocks. Journal of Structural Geology, 31(11), pp.1340-1349.

Turcotte, D.L. and Schubert, G., 2002. Geodynamics.

Twiss, R.J. and Moores, E.M., 2007. Structural geology. Macmillan.

Uehara, S.I. and Shimamoto, T., 2004. Gas permeability evolution of cataclasite and fault gouge in triaxial compression and implications for changes in fault-zone permeability structure through the earthquake cycle. Tectonophysics, 378(3), pp.183-195.

Vajdova, V., Baud, P. and Wong, T.F., 2004. Permeability evolution during localized deformation in Bentheim sandstone. Journal of Geophysical Research: Solid Earth, 109(B10).

Walder, J. and Nur, A., 1984. Porosity reduction and crustal pore pressure development. J. geophys. Res, 89(B13), pp.11539-11548.

Watkinson, A.J., 1976. Fold propagation and interference in a single multilayer unit. Tectonophysics, 34(3-4), pp.T37-T42.

Williams, J.R., 1980. Similar and chevron folds in multilayers using finite-element and geometric models. Tectonophysics, 65(3-4), pp.323-338.

Yang, J., 2006. Finite element modeling of transient saline hydrothermal fluids in multifaulted sedimentary basins: implications for ore-forming processes. Canadian Journal of Earth Sciences, 43(9), pp.1331-1340.

Zhang, Y., Hobbs, B.E., Ord, A. and Mühlhaus, H.B., 1996. Computer simulation of single-layer buckling. Journal of Structural Geology, 18(5), pp.643-655.

Zhang, Y., Mancktelow, N.S., Hobbs, B.E., Ord, A. and Mühlhaus, H.B., 2000. Numerical modelling of single-layer folding: clarification of an issue regarding the possible effect of computer codes and the influence of initial irregularities. Journal of Structural Geology, 22(10), pp.1511-1522.

Zhu, W. and Wong, T.F., 1997. The transition from brittle faulting to cataclastic flow: Permeability evolution. Journal of Geophysical Research: Solid Earth, 102(B2), pp.3027-3041.

SECTION

2. CONCLUSIONS

The study conducts research on the stress and strain evolution and distribution during the deformation of multi-scale single/multilayer folding. In order to understand the fracture associated with single-layer cylindrical buckle folds, a 3D finite element modeling approach using a Maxwell visco-elastic rheology is utilized. The influences of three model parameters with significant influence on fracture initiation are considered: burial depth, viscosity, and permeability. It is concluded that these parameters are critical for the initiation of major fracture sets at the hinge zone with varying degrees. The numerical simulation results further show that the buckling process fails to explain most of the fracture sets occurring in the limb unless the process of erosional unloading as a post-fold phenomenon is considered. For fracture sets that only develop under unrealistic boundary conditions, the results demonstrate that their development is realistic for a perclinal fold geometry. In summary, a more thorough understanding of fractures sets associated with buckle folds is obtained based on the simulation of in-situ stress conditions during the structural development of buckle folds.

Moreover, this study represents the first numerical simulation of multilayer folding with large number of layers investigating the effects of various model system parameters on the resulting stress and strain distribution under in-situ state of stress with gravity and pore pressure. The model shows that chevron fold is observed in the core of the multilayer system with noticeable hinge collapse, and concentric fold is observed at the margin of the multilayer stack. Moreover, the deformation of the multilayer folds show that similar sinusoidal shape of all layers for certain conditions, such as low viscosity contrast or thick less competent layer. This study demonstrates that the shapes of the multilayer folds with visco-elastic rheology and large number of layers depend on the buckling of the folding layers, which is influenced by various parameters such as initial geometry and material properties and model parameters. The results presented show a large variability in stress and strain distribution due to the complex deformation of both competent and less competent layers during the multilayer buckling process. The strain distribution shows that little variety of strain is developed in the competent layer and

large magnitude of compressive strain is observed at the limb of the less competent layer closing to the margin of the multilayer stack. The numerical simulations also provide a general understanding of the influence of various parameters such as initial geometry, material properties and model parameters on the resulting stress and strain distribution.

In addition, porosity distribution resulted from the deformation of parasitic folds are studied here. Parasitic folds represent a common structure of multi-scale multilayer folds and the resulting asymmetric S- or Z-shapes and symmetric M-shapes represent a complex strain distribution. How the strain distribution affects the resulting porosity remains unclear. In this study, a 2-D plane strain finite element modeling approach is used to simulate multi-scale, multilayer, viscoelastic buckle folds under in-situ stress and pore pressure conditions. A variety of material and model parameters (including the elastic modulus contrast, number of layers, viscosity contrast, strain rate and layer thickness ratio) are considered and their influence on the shape of parasitic folds and on the resulting porosity distribution is analyzed. This study demonstrates that the shapes of the parasitic folds depend on the buckling of both the large- and small-scale folds and are influenced by the various parameters. The numerical modeling results show a large variability in porosity changes due to the complex distribution of the volumetric strain during the mutli-scale, multi-layer buckling process. Three regions, including the hinge and limb of the less competent layer in the M-shaped folds and the limb of the less competent layer in the Z-shaped folds, feature significant porosity changes. In addition, the numerical simulations provide a general understanding of the influence of the various model parameters on the resulting porosity distribution. Through the applied volumetric stain-porosity-permeability coupling, influences on the resulting fluid flow regimes in multi-scale, multilayer buckling systems are documented.

VITA

Xiaolong Liu studied safety engineering at China University of Petroleum (Huadong) and earned his Bachelor's degree in Safety Engineering in 2009. After that, he was recommended for admission to be a postgraduate without exams and performed his one year study in the Storage and Transportation of Oil and Gas at the same college in June, 2010. In August 2011, he attended Missouri University of Science and Technology in Rolla, Missouri for his graduate studies in petroleum engineering. Half a year later, he started positions of graduate research assistant and graduate teaching assistant in the Department of Geological Science and Engineering. In December, 2013, he received his M.S. in Petroleum Engineering from Missouri University of Science and Technology. In January 2014, he attended Missouri University of Science and Technology in Rolla, Missouri for his Ph.D in petroleum engineering.

He received Doctor of Philosophy in Petroleum Engineering in May, 2017.